# 14. Neutrino Masses, Mixing, and Oscillations

Revised March 2026 by M.C. Gonzalez-Garcia (YITP, Stony Brook; ICREA, Barcelona; ICC, U. of Barcelona) and R. Wendell (Kyoto U.).



## 14.1 Neutrinos in the Standard Model: Massless Neutrinos

The gauge symmetry principle is one of the pillars of the great success of modern particle physics as it establishes an unambiguous connection between local (gauge) symmetries and forces mediated by spin-1 particles. In the Standard Model (SM) of particle physics the strong, weak, and electromagnetic interactions are connected to gauge symmetry under $SU(3)_{\rm C} \times SU(2)_L \times U(1)_Y$ where C stands for colour, $L$ for left-handedness, and $Y$ for hypercharge. The SM gauge symmetry is spontaneously broken to $SU(3)_{\rm C} \times U(1)_{\rm EM}$ where $U(1)_{\rm EM}$ couples to the electromagnetic charge $Q_{\rm EM} = T_{L3} + Y$ ($T_{L3}$ is the third generator of the weak isospin $SU(2)_L$). The model explains all the interactions of the known fermions once they are assigned to a well defined representation of the gauge group. The construction and tests of the Standard Model as a gauge theory are covered in Chapter 9 "Quantum chromodynamics" and Chapter 10 "Electroweak model and constraints on new physics" of this *Review*. Here we emphasize that the gauge invariance principle requires that all terms in the Lagrangian, including the mass terms, respect the local symmetry. This has important implications for the neutrino and in particular for the question of the neutrino mass [1].

[1] The physics of massive neutrinos has been the subject of excellent books such as [1–5] and multiple review articles. The contents of the present review is built upon the structure and the contents of the review articles [6, 7].

In the SM, neutrinos are fermions that do not have strong nor electromagnetic interactions. Consequently, they are singlets of the subgroup $SU(3)_C \times U(1)_{\rm EM}$. They are part of the lepton doublets $L_{L\ell} = \begin{pmatrix} \nu_\ell \\ \ell \end{pmatrix}_L$ where $f_L$ is the left-handed component of the fermion $f$, $f_L = P_L f \equiv \frac{1-\gamma_5}{2} f$. In what follows we will refer as *active* neutrinos to neutrinos that are part of these lepton doublets. In the SM there is one active neutrino for each charged leptons, $\ell = e, \mu, \tau$. $SU(2)_L$ gauge invariance dictates the form of weak charged current (CC) interactions between the neutrinos and their corresponding charged leptons and neutral current (NC) among themselves to be:

$$-\mathcal{L}_{\rm CC} = \frac{g}{\sqrt{2}} \sum_\ell \bar{\nu}_{L\ell} \gamma^\mu \ell_L^- W_\mu^\dagger + \text{h.c.}\,, \tag{14.1}$$

$$-\mathcal{L}_{\rm NC} = \frac{g}{2\cos\theta_W} \sum_\ell \bar{\nu}_{L\ell} \gamma^\mu \nu_{L\ell} Z_\mu^0\,. \tag{14.2}$$

In the above equations, $g$ is the coupling constant associated with $SU(2)$ and $\theta_W$ is the Weinberg angle. Equations (14.1) and (14.2) describe all the neutrino interactions in the SM. In particular, Eq. (14.2) determines the decay width of the $Z$ boson into light ($m_\nu \leq m_Z/2$) left-handed neutrinos states. Thus from the measurement of the total decay width of the $Z$ one can infer the number of such states. At present the measurement implies $N_\nu = 2.984 \pm 0.008$ (see Particle Listing). As a result any extension of the SM should contain three, and only three, light active neutrinos.

*Sterile* neutrinos are defined as having no SM gauge interactions, that is, they are singlets of the complete SM gauge group. Thus the SM, as the gauge theory able to describe all known particle interactions, contains no sterile neutrinos.

The SM with its gauge symmetry and the particle content required for the gauge interactions, that is, in the absence of SM singlets, respects an accidental global symmetry that is not imposed but appears as a consequence of the gauge symmetry and the representation of the matter fields:

$$G_{\rm SM}^{\rm global} = U(1)_B \times U(1)_{L_e} \times U(1)_{L_\mu} \times U(1)_{L_\tau}, \tag{14.3}$$

where $U(1)_B$ is the baryon number symmetry, and $U(1)_{L_e,L_\mu,L_\tau}$ are the three lepton flavour symmetries. The total lepton number, $L_e + L_\mu + L_\tau$, is then also an accidental symmetry since it is a subgroup of $G_{\rm SM}^{\rm global}$. This fact has consequences that are relevant to the question of the neutrino mass as we argue next.

In the SM, the masses of the fermions are generated via a Yukawa coupling of the scalar Higgs doublet $\phi$ with a fermion right-handed and left-handed component. The former is an $SU(2)_L$ singlet, the latter is part of a doublet. For leptons, we can build such a term coupling the left-handed lepton doublets $L_L$ with the right-handed charged lepton fields $E_R$:

$$-\mathcal{L}_{\rm Yukawa,lep} = Y_{ij}^\ell \bar{L}_{Li} \phi E_{Rj} + \text{h.c.}\,. \tag{14.4}$$

After spontaneous symmetry breaking these terms lead to charged lepton masses

$$m_{ij}^\ell = Y_{ij}^\ell \frac{v}{\sqrt{2}}\,, \tag{14.5}$$

where $v$ is the vacuum expectation value of the Higgs field. However, since the model does not contain right-handed neutrinos, no such Yukawa interaction can be built for the neutrinos, which are consequently massless at the Lagrangian level.

In principle, a neutrino mass term could be generated at loop level. With the particle content of the SM the only possible neutrino mass term that could be constructed is the bilinear $\bar{L}_L L_L^c$, where

$L_L^c$ is the charge conjugated field, $L_L^c = C\bar{L_L}^T$ and $C$ is the charge conjugation matrix. However this term is forbidden in the SM because it violates the total lepton symmetry by two units and therefore it cannot be induced by loop corrections because it breaks the accidental symmetry of the model. Also, because $U(1)_{B-L}$ is a non-anomalous subgroup of $G_{\rm SM}^{\rm global}$, the bilinear $\bar{L}_L L_L^c$, cannot be induced by nonperturbative corrections either since it breaks $B-L$.

We conclude that within the SM neutrinos are precisely massless. Consequently one must go beyond the SM in order to add a mass to the neutrino.

## 14.2 Extending the Standard Model to Introduce Massive Neutrinos

From the above discussion, we conclude that it is not possible to construct a renormalizable mass term for the neutrinos with the fermionic content and gauge symmetry of the SM. The obvious consequence is that in order to introduce a neutrino mass in the theory one must extend the particle content of the model, depart from gauge invariance and/or renormalizability, or do both.

As a matter of fact, neutrino mass terms can be constructed in different ways. In the following we shall assume that the gauge symmetry is mantained and explore the different possibilities to introduce a neutrino mass term adding to the SM an arbitrary number of sterile neutrinos $\nu_{si}$ $(i = 1, \dots m)$.

In the SM extended with the addition of $m$ number of sterile neutrinos one can construct two gauge invariant renormalizable operators leading to two types of mass terms

$$-\mathcal{L}_{M_\nu} = M_{D\,ij}\bar{\nu}_{si}\nu_{Lj} + \frac{1}{2}M_{N\,ij}\bar{\nu}_{si}\nu_{sj}^c + \text{h.c.}\,, \tag{14.6}$$

where $\nu^c$ is the neutrino charge conjugated field (defined in section 14.1). $M_D$ is a complex matrix of dimension $m \times 3$ and $M_N$ is a symmetric $m \times m$ matrix.

The first term is generated after spontaneous electroweak symmetry breaking from Yukawa interactions,

$$Y_{ij}^\nu \bar{\nu}_{si}\tilde{\phi}^\dagger L_{Lj} \Rightarrow M_{D\,ij} = Y_{ij}^\nu \frac{v}{\sqrt{2}}\,, \tag{14.7}$$

in a similar way to Eqs.(14.4) and (14.5) for the charged fermion masses. It is correspondingly called a Dirac mass term. It conserves total lepton number but it can break the lepton flavour number symmetries.

The second term in Eq. (14.6) is a Majorana mass term and it differs from the Dirac mass terms in several relevant aspects. First, it is a singlet of the SM gauge group and, as such, it can appear as a bare mass term in the Lagrangian. Second, since it involves two neutrino fields (right-handed in this case), it breaks lepton number by two units. In general, such a term is not allowed if the neutrinos carry any additive conserved charge.

It is possible to rewrite Eq. (14.6) as:

$$-\mathcal{L}_{M_\nu} = \frac{1}{2}(\overline{\vec{\nu}_L^c}, \overline{\vec{\nu}_s}) \begin{pmatrix} 0 & M_D^T \\ M_D & M_N \end{pmatrix} \begin{pmatrix} \vec{\nu}_L \\ \vec{\nu}_s^c \end{pmatrix} + \text{h.c.} \equiv \overline{\vec{\nu}^c} M_\nu \vec{\nu} + \text{h.c.}\,, \tag{14.8}$$

where $\vec{\nu} = (\vec{\nu}_L,\, \vec{\nu_s^c})^T$ is a $(3+m)$-dimensional vector. The matrix $M_\nu$ is complex and symmetric [2]. Thus it can be diagonalized by a unitary matrix $V^\nu$ of dimension$(3+m)$, so

$$(V^\nu)^T M_\nu V^\nu = \text{diag}(m_1, m_2, \dots, m_{3+m})\,. \tag{14.9}$$

One can express the original weak eigenstates in terms of the resulting $3+m$ mass eigenstates

$$\vec{\nu}_{\rm mass} = (V^\nu)^\dagger \vec{\nu}\,, \tag{14.10}$$

[2] Notice that Eq. (14.8) corresponds to the tree-level neutrino mass matrix. Corrections are induced at the loop level, which in particular lead to non-vanishing $\bar{\nu}_L^c \nu_L$ entry [8].

and in terms of the mass eigenstates, Eq. (14.8) takes the form:

$$-\mathcal{L}_{M_\nu} = \frac{1}{2}\sum_{k=1}^{3+m} m_k \left(\bar{\nu}^c_{\text{mass},k}\nu_{\text{mass},k} + \bar{\nu}_{\text{mass},k}\nu^c_{\text{mass},k}\right)$$
$$= \frac{1}{2}\sum_{k=1}^{3+m} m_k \bar{\nu}_{Mk}\nu_{Mk}\,, \tag{14.11}$$

where

$$\nu_{Mk} = \nu_{\text{mass},k} + \nu^c_{\text{mass},k} = (V^{\nu\dagger}\vec{\nu})_k + (V^{\nu\dagger}\vec{\nu})^c_k\,. \tag{14.12}$$

So these states obey the Majorana condition

$$\nu_M = \nu^c_M\,, \tag{14.13}$$

and are referred to as Majorana neutrinos. The Majorana condition implies that only one field describes both neutrino and antineutrino states, unlike the case of a charged fermion for which particles and antiparticles are described by two different fields. So a Majorana neutrino can be described by a two-component spinor unlike the charged fermions, which are Dirac particles, and are represented by four-component spinors.

Inverting Eq. (14.12) we can write the weak-doublet components of the neutrino fields as:

$$\nu_{Li} = P_L \sum_{j=1}^{3+m} V^\nu_{ij}\nu_{Mj} \quad i = 1,2,3\,, \tag{14.14}$$

where $P_L$ is the left projector.

In the following, we will discuss some interesting particular cases of this general framework: light Dirac neutrinos in Sec. 14.2.1, and light Majorana neutrinos and the see-saw mechanism in Sec. 14.2.2. A special case of the second example is the possibility of light-sterile neutrinos discussed in Sec. 14.2.3. In Sec. 14.2.4 we shall discuss the effective generation of neutrino masses from non-renormalizable operators (of which the see-saw mechanism is a particular realization).

### 14.2.1 *Dirac Neutrinos*

Imposing $M_N = 0$ is equivalent to imposing lepton number symmetry on the model. In doing this only the first term in Eq. (14.6), the Dirac mass term, is allowed. If there are only three sterile neutrinos( $m = 3$), we can identify them with the right-handed component of a four-spinor neutrino field. In this case the Dirac mass term can be diagonalized with two $3 \times 3$ unitary matrices, $V^\nu$ and $V^\nu_R$ as:

$$V^{\nu\dagger}_R M_D V^\nu = \text{diag}(m_1, m_2, m_3)\,. \tag{14.15}$$

The neutrino mass term can be written as:

$$-\mathcal{L}_{M_\nu} = \sum_{k=1}^{3} m_k \bar{\nu}_{Dk}\nu_{Dk}\,, \tag{14.16}$$

where

$$\nu_{Dk} = (V^{\nu\dagger}\vec{\nu}_L)_k + (V^{\nu\dagger}_R\vec{\nu}_s)_k\,, \tag{14.17}$$

so the weak-doublet components of the neutrino fields are

$$\nu_{Li} = P_L \sum_{j=1}^{3} V^\nu_{ij}\nu_{Dj}\,. \qquad i = 1,2,3\,. \tag{14.18}$$

Let us stress that in this case both the low-energy matter content and the assumed symmetries are different from those of the SM. Consequently, the SM is not even a good low-energy effective theory. Furthermore, this scenario does not explain the fact that neutrinos are much lighter than the corresponding charged fermions, because all of them acquire their mass via the same mechanism.

### 14.2.2 *The See-saw Mechanism*

If the mass eigenvalues of $M_N$ are much higher than the scale of electroweak symmetry breaking $v$, the diagonalization of $M_\nu$ leads to three light neutrinos, $\nu_l$, and $m$ heavy neutrinos, $N$:

$$-\mathcal{L}_{M_\nu} = \frac{1}{2}\bar{\nu}_l M^l \nu_l + \frac{1}{2}\bar{N} M^h N\,, \tag{14.19}$$

with

$$M^l \simeq -V_l^T M_D^T M_N^{-1} M_D V_l, \qquad M^h \simeq V_h^T M_N V_h\,, \tag{14.20}$$

and

$$V^\nu \simeq \begin{bmatrix} \left(1 - \frac{1}{2} M_D^\dagger {M_N^*}^{-1} 1 M_N^{-1} M_D\right) V_l & M_D^\dagger {M_N^*}^{-1} V_h \\ -M_N^{-1} M_D V_l & \left(1 - \frac{1}{2} {M_N}^{-1} M_D M_D^\dagger {M_N^*}^{-1}\right) V_h \end{bmatrix}, \tag{14.21}$$

where $V_l$ and $V_h$ are $3\times 3$ and $m \times m$ unitary matrices respectively. From Eq. (14.20) we see that the masses of the heavier states are proportional to $M_N$ while those of the lighter ones to $M_N^{-1}$, hence the name *see-saw mechanism* [9–13]. Also, as seen from Eq. (14.21), the heavy states are mostly right-handed while the light ones are mostly left-handed. Both the light and the heavy neutrinos are Majorana particles. Two well-known examples of extensions of the SM leading to a see-saw mechanism for neutrino masses are SO(10) Grand Unified Theories [10, 11] and left-right symmetric models [13].

In this case, the SM is a good effective low energy theory. Indeed the see-saw mechanism is a particular example of a full theory whose low energy effective realization is the SM with three light Majorana neutrinos which we describe in Sec. 14.2.4.

### 14.2.3 *Light Sterile Neutrinos*

If the scale of some $n_s \leq m$ eigenvalues of $M_N$ are not higher than the electroweak scale, the low energy spectrum contains $n_s$ additional light states with a large admixture of sterile component. As in the case with Dirac Neutrinos, the SM is not a good low energy effective theory: there are more than three ($3+n_s$) light neutrinos, and they are admixtures of doublet and singlet fields. As in the general case, both light and heavy neutrinos are Majorana particles.

### 14.2.4 *Neutrino Masses from Generic New Physics*

Under the generic hypothesis that new physics (NP) beyond the SM only manifests itself directly above some scale $\Lambda_{\rm NP}$, we can consider that the SM is an effective low energy theory which is valid to describe the physical world at energies well below $\Lambda_{\rm NP}$ with the same gauge group, fermionic spectrum, and the pattern of spontaneous symmetry breaking of the SM. However, this is an effective theory, holding only till energy below $\Lambda_{\rm NP}$, and consequently does not need to be renormalizable. In this case, the low energy Lagrangian can contain non-renormalizable higher dimensional terms whose effect will be suppressed by powers $1/\Lambda_{\rm NP}^{\rm dim-4}$.

In this approach, the least suppressed NP effects at low energy are expected to come from dim= 5 operators. With the SM fields and gauge symmetry one can only construct the following set of dimension-five terms

$$\mathcal{O}_5 = \frac{Z^\nu_{ij}}{\Lambda_{\rm NP}}\left(\bar{L}_{Li}\tilde{\phi}\right)\left(\tilde{\phi}^T L^C_{Lj}\right) + \text{h.c.}\,. \tag{14.22}$$

This set violates (14.3), which poses no problem since, in general, there is no reason for the NP to respect the accidental symmetries of the SM. In particular, it violates the total lepton number by

two units, and after spontaneous symmetry breaking it generates a bilinear neutrino field term:

$$-\mathcal{L}_{M_\nu} = \frac{Z^\nu_{ij}}{2}\frac{v^2}{\Lambda_{\rm NP}}\bar{\nu}_{Li}\nu^c_{Lj} + \text{h.c.}\,. \tag{14.23}$$

This is a Majorana mass term (see Eq. (14.8)). It is built with the left-handed neutrino fields and with mass matrix:

$$(M_\nu)_{ij} = Z^\nu_{ij}\frac{v^2}{\Lambda_{\rm NP}}\,. \tag{14.24}$$

We conclude that Eq. (14.24) would arise in a generic extension of the SM and that neutrino masses are very likely to appear if there is NP. Comparing Eq. (14.24) and Eq. (14.5), we also find that the scale of neutrino masses is suppressed by $v/\Lambda_{\rm NP}$ when compared to the scale of charged fermion masses, which provides an explanation for their smallness. Furthermore, both total lepton number and the lepton flavour symmetry $U(1)_e \times U(1)_\mu \times U(1)_\tau$ are broken by Eq. (14.24), which means that, generically, in the absence of additional symmetries on the coefficients $Z_{ij}$, we can expect lepton flavour mixing and $CP$ violation as we discuss in the next section.

Finally, we notice that, as mentioned in Sec. 14.2.2, a theory where the NP is composed of $m$ heavy sterile neutrinos, provides an specific example of a theory which at low energy contains three light mass eigenstates with an effective dim-5 interaction of the form (14.22) with $\Lambda_{\rm NP} = M_N$. In this case, the NP scale is the characteristic mass scale of the heavy sterile neutrinos.

## 14.3 Lepton Mixing

Let us start by considering $n = 3 + m$ massive neutrino states and denote the neutrino mass eigenstates by $(\nu_1, \nu_2, \nu_3, \ldots, \nu_n)$. The neutrino interaction eigenstates are denoted by $\vec{\nu} = (\nu_{Le}, \nu_{L\mu}, \nu_{L\tau}, \nu_{s1}, \ldots, \nu_{sm})$. We label the corresponding mass and interaction eigenstates for the charged leptons as $(e, \mu, \tau)$ and $(e^I, \mu^I, \tau^I)$, respectively. The Lagrangian for the leptonic charged current interactions in the mass basis takes the form:

$$-\mathcal{L}_{\rm CC} = \frac{g}{\sqrt{2}}(\bar{e}_L,\, \bar{\mu}_L,\, \bar{\tau}_L)\gamma^\mu U \begin{pmatrix}\nu_1\\ \nu_2\\ \nu_3\\ \vdots\\ \nu_n\end{pmatrix} W_\mu + \text{h.c.}\,, \tag{14.25}$$

where $U$ is a $3 \times n$ matrix [14–16]. It satisfies the unitary condition

$$UU^\dagger = I_{3\times 3}\,. \tag{14.26}$$

However, in general $U^\dagger U \neq I_{n\times n}$.

In the interaction basis, the mass terms for the leptons are:

$$-\mathcal{L}_M = [(\bar{e}^I_L,\, \bar{\mu}^I_L,\, \bar{\tau}^I_L)M_\ell \begin{pmatrix}e^I_R\\ \mu^I_R\\ \tau^I_R\end{pmatrix} + \text{h.c.}] - \mathcal{L}_{M_\nu}\,, \tag{14.27}$$

with $\mathcal{L}_{M_\nu}$ given in Eq. (14.8). $M_\ell$ can be diagonalized with two $3 \times 3$ unitary matrices $V^\ell$ and $V^\ell_R$ which satisfy

$$V^{\ell\dagger} M_\ell V^\ell_R = \text{diag}(m_e, m_\mu, m_\tau)\,. \tag{14.28}$$

Then for the charged leptons we have

$$-\mathcal{L}_{M_\ell} = \sum_{k=1}^{3} m_{\ell_k}\bar{\ell}_k\ell_k\,, \tag{14.29}$$

with

$$\ell_k = (V^{\ell\dagger}\ell_L^I)_k + (V_R^{\ell\dagger}\ell_R^I)_k\,. \tag{14.30}$$

Inverting the equation above we find that the weak-doublet components of the charged lepton fields are

$$\ell_{Li}^I = P_L \sum_{j=1}^{3} V_{ij}^{\ell}\ell_j\,. \qquad i=1,2,3 \tag{14.31}$$

From Eqs.(14.14), (14.18) and (14.31) we find that the mixing matrix $U$ can be expressed as:

$$U_{ij} = \mathcal{P}_{\ell,ii}\, V_{ik}^{\ell\,\dagger}\, V_{kj}^{\nu}\, (\mathcal{P}_{\nu,jj}). \tag{14.32}$$

The matrix $V^{\ell\dagger}V^{\nu}$ contains a number of phases that are not physical. Three of them are eliminated by the diagonal $3\times3$ phase matrix $\mathcal{P}_\ell$ that absorbs them in the charged lepton mass eigenstates. If neutrinos are Dirac states, further $n-1$ are similarly eliminated by absorbing them in the neutrino mass eigenstates with the diagonal $n\times n$ phase matrix $\mathcal{P}_\nu$. For Majorana neutrinos, $\mathcal{P}_\nu = I_{n\times n}$ because one cannot rotate by an arbitrary phase a Majorana field without physical effects. If one rotates a Majorana neutrino by a phase, this phase will appear in its mass term, which will no longer be real. Consequently, the number of phases that can be absorbed by redefining the mass eigenstates depends on whether the neutrinos are Dirac or Majorana particles. Altogether for $n\geq 3$ Majorana [Dirac] neutrinos, the $U$ matrix contains a total of $6(n-2)$ [$5n-11$] real parameters, of which $3(n-2)$ are angles, and $3(n-2)$ [$2n-5$] can be interpreted as physical phases.

The possibility of arbitrary mixing between massive neutrino states was first discussed in the context of two neutrinos in Ref. [17] (the possibility of two mixed massless flavour neutrino states had been previously considered in the literature [18], and the possibility of mixing between neutrino and antineutrino states even earlier, in the seminal paper of Pontecorvo [19]). For the case where only mixing between two generations is considered with $n=2$ distinct neutrino masses, the $U$ matrix is $2\times2$ and contains one mixing angle if the neutrinos are Dirac and an additional physical phase if they are Majorana.

If there are only $n=3$ Majorana neutrinos, $U$ is a $3\times3$ matrix analogous to the CKM matrix for the quarks [20, 21], but due to the Majorana nature of the neutrinos it depends on six independent parameters: three mixing angles and three phases. In this case the mixing matrix can be conveniently parameterized as:

$$U = \begin{pmatrix} 1 & 0 & 0 \\ 0 & c_{23} & s_{23} \\ 0 & -s_{23} & c_{23} \end{pmatrix} \cdot \begin{pmatrix} c_{13} & 0 & s_{13}e^{-i\delta_{\rm CP}} \\ 0 & 1 & 0 \\ -s_{13}e^{i\delta_{\rm CP}} & 0 & c_{13} \end{pmatrix} \cdot \begin{pmatrix} c_{12} & s_{12} & 0 \\ -s_{12} & c_{12} & 0 \\ 0 & 0 & 1 \end{pmatrix} \cdot \begin{pmatrix} e^{i\eta_1} & 0 & 0 \\ 0 & e^{i\eta_2} & 0 \\ 0 & 0 & 1 \end{pmatrix}, \tag{14.33}$$

where $c_{ij}\equiv\cos\theta_{ij}$ and $s_{ij}\equiv\sin\theta_{ij}$. The angles $\theta_{ij}$ can be taken without loss of generality to lie in the first quadrant, $\theta_{ij}\in[0,\pi/2]$ and the phases $\delta_{\rm CP}$, $\eta_i\in[0,2\pi]$. This is to be compared to the case of three Dirac neutrinos. In this case, the Majorana phases, $\eta_1$ and $\eta_2$, can be absorbed in the neutrino states so the number of physical phases is one (similar to the CKM matrix). Thus we can write $U$ as:

$$U = \begin{pmatrix} c_{12}\,c_{13} & s_{12}\,c_{13} & s_{13}\,e^{-i\delta_{\rm CP}} \\ -s_{12}\,c_{23} - c_{12}\,s_{13}\,s_{23}\,e^{i\delta_{\rm CP}} & c_{12}\,c_{23} - s_{12}\,s_{13}\,s_{23}\,e^{i\delta_{\rm CP}} & c_{13}\,s_{23} \\ s_{12}\,s_{23} - c_{12}\,s_{13}\,c_{23}\,e^{i\delta_{\rm CP}} & -c_{12}\,s_{23} - s_{12}\,s_{13}\,c_{23}\,e^{i\delta_{\rm CP}} & c_{13}\,c_{23} \end{pmatrix}. \tag{14.34}$$

The matrices in Eqs. (14.33) and (14.34) are often called the Pontecorvo-Maki-Nakagawa-Sakata (PMNS) mixing matrix.

Notice that when the charged leptons have no other interactions than the SM ones, one can identify their interaction eigenstates with the corresponding mass eigenstates up to phase redefinition. This implies that, in this case, $U$ is just a $3 \times n$ sub-matrix of the unitary neutrino mass diagonalizing matrix $V^\nu$.

Finally, let us point out that for the case of 3 light Dirac neutrinos, the procedure above leads to a unitary $U$ matrix for the light states. But for three light Majorana neutrinos, this is not the case since the full spectrum contains states which are heavy and are not in the low energy spectrum as seen, for example, in Eq. (14.21). This implies that, strictly speaking, the parametrization in Eq. (14.33) is not valid to describe the flavour mixing of the three light Majorana neutrinos in the see-saw mechanism. The violation of unitarity, however, is rather small, of the order $\mathcal{O}(M_D/M_N)$ as seen in Eq. (14.21). It is also severely constrained experimentally [22, 23]. For all these reasons, for all practical purposes, we will consider the $U$ matrix for the $3\nu$ mixing case to be unitary independently of whether neutrinos are Dirac or Majorana particles.

## 14.4 Mass-Induced Flavour Oscillations in Vacuum

If neutrinos have masses and lepton flavours are mixed in the weak CC interactions, lepton flavour is not conserved in neutrino propagation [19, 24]. This phenomenon is usually referred to as *neutrino oscillations*. In brief, a weak eigenstates, $\nu_\alpha$, which by default is the state produced in the weak CC interaction of a charged lepton $\ell_\alpha$, is the linear combination determined by the mixing matrix $U$

$$|\nu_\alpha\rangle = \sum_{i=1}^{n} U^*_{\alpha i} |\nu_i\rangle \,, \tag{14.35}$$

where $\nu_i$ are the mass eigenstates, and here $n$ is the number of light neutrino species (implicit in our definition of the state $|\nu\rangle$ is its energy-momentum and space-time dependence). After traveling a distance $L$ ($L \simeq ct$ for relativistic neutrinos), that state evolves as:

$$|\nu_\alpha(t)\rangle = \sum_{i=1}^{n} U^*_{\alpha i} |\nu_i(t)\rangle \,. \tag{14.36}$$

This neutrino can then undergo a charged-current (CC) interaction producing a charge lepton $\ell_\beta$, $\nu_\alpha(t) N' \to \ell_\beta N$, with a probability

$$P_{\alpha\beta} = |\langle \nu_\beta | \nu_\alpha(t)\rangle|^2 = |\sum_{i=1}^{n}\sum_{j=1}^{n} U^*_{\alpha i} U_{\beta j} \langle \nu_j | \nu_i(t)\rangle|^2 \,. \tag{14.37}$$

Assuming that $|\nu\rangle$ is a plane wave, $|\nu_i(t)\rangle = e^{-i\,E_i t}|\nu_i(0)\rangle$, [3] with $E_i = \sqrt{p_i^2 + m_i^2}$ and $m_i$ being, respectively, the energy and the mass of the neutrino mass eigenstate $\nu_i$. In all practical cases neutrinos are very relativistic ,so $p_i \simeq p_j \equiv p \simeq E$. We can then write

$$E_i = \sqrt{p_i^2 + m_i^2} \simeq p + \frac{m_i^2}{2E} \,, \tag{14.38}$$

and use the orthogonality of the mass eigenstates, $\langle \nu_j | \nu_i \rangle = \delta_{ij}$, to arrive to the following form for $P_{\alpha\beta}$:

$$\begin{aligned} P_{\alpha\beta} = \delta_{\alpha\beta} &- 4 \sum_{i<j}^{n} \mathrm{Re}[U_{\alpha i} U^*_{\beta i} U^*_{\alpha j} U_{\beta j}] \sin^2 X_{ij} \\ &+ 2 \sum_{i<j}^{n} \mathrm{Im}[U_{\alpha i} U^*_{\beta i} U^*_{\alpha j} U_{\beta j}] \sin 2X_{ij} \,, \end{aligned} \tag{14.39}$$

[3] For a pedagogical discussion of the quantum mechanical description of flavour oscillations in the wave packet approach see for example Ref. [3]. A recent review of the quantum mechanical aspects and subtleties on neutrino oscillations can be found in in Ref. [25].

where

$$X_{ij} = \frac{(m_i^2 - m_j^2)L}{4E} = 1.267 \, \frac{\Delta m_{ij}^2}{\text{eV}^2} \, \frac{L/E}{\text{m/MeV}} \, . \tag{14.40}$$

If we had made the same derivation for antineutrino states, we would have ended with a similar expression but with the exchange $U \to U^*$. Consequently, we conclude that the first term in the right-hand-side of Eq. (14.39) is $CP$ conserving since it is the same for neutrinos and antineutrinos, while the last one is $CP$ violating because it has opposite signs for neutrinos and antineutrinos.

**Table 14.1:** Characteristic values of $L$ and $E$ for experiments performed using various neutrino sources and the corresponding ranges of $|\Delta m^2|$ to which they can be most sensitive to flavour oscillations in vacuum. SBL stands for Short Baseline, VSBL stands for Very Short Baseline , MBL stands for Medium Baseline, and LBL for Long Baseline.

| Experiment | | $L$ (m) | $E$ (MeV) | $\lvert\Delta m^2\rvert$ (eV$^2$) |
|---|---|---|---|---|
| Solar | | $10^{10}$ | 1 | $10^{-10}$ |
| Atmospheric | | $10^4 - 10^7$ | $10^2$–$10^5$ | $10^{-1} - 10^{-4}$ |
| Reactor | VSBL–SBL–MBL | $10 - 10^3$ | 1 | $1 - 10^{-3}$ |
| | LBL | $10^4 - 10^5$ | | $10^{-4} - 10^{-5}$ |
| Accelerator | SBL | $10^2$ | $10^3$–$10^4$ | $> 0.1$ |
| | LBL | $10^5 - 10^6$ | $10^3 - 10^4$ | $10^{-2} - 10^{-3}$ |

Equation (14.39) is oscillatory in distance with oscillation lengths

$$L_{0,ij}^{\text{osc}} = \frac{4\pi E}{|\Delta m_{ij}^2|} \, , \tag{14.41}$$

and with amplitudes proportional to products of elements in the mixing matrix. Thus, neutrinos must have different masses ($\Delta m_{ij}^2 \neq 0$) and they must have not vanishing mixing ($U_{\alpha_i} U_{\beta i} \neq 0$) in order to undergo flavour oscillations. Also, from Eq. (14.39) we see that the Majorana phases cancel out in the oscillation probability. This is expected because flavour oscillation is a total lepton number conserving process.

Ideally, a neutrino oscillation experiment would like to measure an oscillation probability over a distance $L$ between the source and the detector, for neutrinos of a definite energy $E$. In practice, neutrino beams, both from natural or artificial sources, are never monoenergetic but have an energy spectrum $\Phi(E)$. In addition, each detector has a finite energy resolution. Under these circumstances what is measured is an average probability

$$\begin{aligned} \langle P_{\alpha\beta} \rangle &= \frac{\int dE \frac{d\Phi}{dE} \sigma_{CC}(E) P_{\alpha\beta}(E) \epsilon(E)}{\int dE \frac{d\Phi}{dE} \sigma_{CC}(E) \epsilon(E)} \\ &= \delta_{\alpha\beta} - 4 \sum_{i<j}^{n} \text{Re}[U_{\alpha i} U_{\beta i}^* U_{\alpha j}^* U_{\beta j}] \langle \sin^2 X_{ij} \rangle + 2 \sum_{i<j}^{n} \text{Im}[U_{\alpha i} U_{\beta i}^* U_{\alpha j}^* U_{\beta j}] \langle \sin 2X_{ij} \rangle \, . \end{aligned} \tag{14.42}$$

$\sigma$ is the cross-section for the process in which the neutrino flavour is detected, and $\epsilon(E)$ is the detection efficiency. The minimal range of the energy integral is determined by the energy resolution of the experiment.

It is clear from the above expression that if $(E/L) \gg |\Delta m_{ij}^2|$ ($L \ll L_{0,ij}^{\text{osc}}$) so $\sin^2 X_{ij} \ll 1$, the oscillation phase does not give any appreciable effect. Conversely, if $L \gg L_{0,ij}^{\text{osc}}$, many oscillation

cycles occur between production and detection, so the oscillating term is averaged to $\langle \sin^2 X_{ij} \rangle = 1/2$. We summarize in Table 14.1 the typical values of $L/E$ for different types of neutrino sources and experiments and the corresponding ranges of $\Delta m^2$ to which they can be most sensitive.

Historically, the results of neutrino oscillation experiments were interpreted assuming two-neutrino states so there is only one oscillating phase; the mixing matrix depends on a single mixing angle $\theta$, and no $CP$ violation effect in oscillations is possible. At present, as we will discuss in Sec. 14.7, we need at least the mixing among three-neutrino states to fully describe the bulk of experimental results. However, in many cases, the observed results can be understood in terms of oscillations dominantly driven by one $\Delta m^2$. In this limit $P_{\alpha\beta}$ of Eq. (14.39) takes the form [24]

$$P_{\alpha\beta} = \delta_{\alpha\beta} - (2\delta_{\alpha\beta} - 1) \sin^2 2\theta \sin^2 X \,. \tag{14.43}$$

In this effective $2-\nu$ limit, changing the sign of the mass difference, $\Delta m^2 \to -\Delta m^2$, and changing the octant of the mixing angle, $\theta \to \frac{\pi}{2} - \theta$, is just redefining the mass eigenstates, $\nu_1 \leftrightarrow \nu_2$: $P_{\alpha\beta}$ must be invariant under such transformation. So the physical parameter space can be covered with either $\Delta m^2 \geq 0$ with $0 \leq \theta \leq \frac{\pi}{2}$, or, alternatively, $0 \leq \theta \leq \frac{\pi}{4}$ with either sign for $\Delta m^2$.

However, from Eq. (14.43) we see that $P_{\alpha\beta}$ is actually invariant under the change of sign of the mass splitting *and* the change of octant of the mixing angle separately. This implies that there is a two-fold discrete ambiguity since the two different sets of physical parameters, $(\Delta m^2, \theta)$ and $(\Delta m^2, \frac{\pi}{2} - \theta)$, give the same transition probability in vacuum. In other words, one could not tell from a measurement of, say, $P_{e\mu}$ in vacuum whether the larger component of $\nu_e$ resides in the heavier or in the lighter neutrino mass eigenstate. This symmetry is broken when one considers mixing of three or more neutrinos in the flavour evolution and or when the neutrinos traverse regions of dense matter as we describe in Sec. 14.7.1 and Sec. 14.5, respectively.

## 14.5 Propagation of Massive Neutrinos in Matter

Neutrinos propagating in a dense medium can interact with the particles in the medium. The probability of an incoherent inelastic scattering is very small. For example the characteristic cross section for $\nu$-proton scattering is of the order

$$\sigma \sim \frac{G_F^2 s}{\pi} \sim 10^{-43} \text{ cm}^2 \left( \frac{E}{\text{MeV}} \right)^2 , \tag{14.44}$$

where $G_F$ is the Fermi constant and $s$ is the square of the center of mass energy of the collision.

But when neutrinos propagate in dense matter, they can also interact coherently with the particles in the medium. By definition, in coherent interactions, the medium remains unchanged so it is possible to have interference of the forward scattered and the unscattered neutrino waves which enhances the effect of matter in the neutrino propagation. In this case, the effect of the medium is not on the intensity of the propagating neutrino beam, which remains unchanged, but on the phase velocity of the neutrino wave, and for this reason the effect is proportional to $G_F$, instead of the $G_F^2$ dependence of the incoherent scattering. Coherence also allows decoupling the evolution equation of the neutrinos from those of the medium. In this limit, the effect of the medium is introduced in the evolution equation for the neutrinos in the form of an effective potential which depends on the density and composition of the matter [26].

As an example, let us consider the evolution of $\nu_e$ in a medium with electrons, protons, and neutrons with corresponding $n_e$, $n_p$, and $n_n$ number densities. The effective low-energy Hamiltonian describing the relevant neutrino interactions at point $x$ is given by

$$H_W = \frac{G_F}{\sqrt{2}} \left[ J^{(+)\alpha}(x) J_\alpha^{(-)}(x) + \frac{1}{4} J^{(N)\alpha}(x) J_\alpha^{(N)}(x) \right] , \tag{14.45}$$

where the $J_\alpha$'s are the standard fermionic currents

$$J_\alpha^{(+)}(x) = \bar{\nu}_e(x)\gamma_\alpha(1-\gamma_5)e(x)\,, \tag{14.46}$$

$$J_\alpha^{(-)}(x) = \bar{e}(x)\gamma_\alpha(1-\gamma_5)\nu_e(x)\,, \tag{14.47}$$

$$\begin{aligned} J_\alpha^{(N)}(x) = {} & \bar{\nu}_e(x)\gamma_\alpha(1-\gamma_5)\nu_e(x) \\ & - \bar{e}(x)[\gamma_\alpha(1-\gamma_5) - 4\sin^2\theta_W\gamma_\alpha]e(x) \\ & + \bar{p}(x)[\gamma_\alpha(1-g_A^{(p)}\gamma_5) - 4\sin^2\theta_W\gamma_\alpha]p(x) \\ & - \bar{n}(x)\gamma_\alpha(1-g_A^{(n)}\gamma_5)n(x)\,, \end{aligned} \tag{14.48}$$

and $g_A^{(n,p)}$ are the axial couplings for neutrons and protons, respectively.

Let us focus first on the effect of the charged current interactions. The effective CC Hamiltonian due to electrons in the medium is

$$\begin{aligned} H_C^{(e)} &= \frac{G_F}{\sqrt{2}}\int d^3p_e f(E_e,T)\times\Big\langle\langle e(s,p_e)\,|\,\bar{e}(x)\gamma^\alpha(1-\gamma_5)\nu_e(x)\bar{\nu}_e(x)\gamma_\alpha(1-\gamma_5)e(x)\,|\,e(s,p_e)\rangle\Big\rangle \\ &= \frac{G_F}{\sqrt{2}}\bar{\nu}_e(x)\gamma_\alpha(1-\gamma_5)\nu_e(x)\int d^3p_e f(E_e,T)\Big\langle\langle e(s,p_e)\,|\,\bar{e}(x)\gamma_\alpha(1-\gamma_5)e(x)\,|\,e(s,p_e)\rangle\Big\rangle\,. \end{aligned} \tag{14.49}$$

In the above equation, we denote by $s$ the electron spin, and by $p_e$ its momentum, and $f(E_e,T)$ is the energy distribution function of the electrons in the medium which is assumed to be homogeneous and isotropic and is normalized as

$$\int d^3p_e f(E_e,T) = 1\,. \tag{14.50}$$

We denote by $\Big\langle\ldots\Big\rangle$ the averaging over electron spinors and summing over all electrons in the medium. Coherence dictates that $s$, $p_e$ are the same for initial and final electrons. The axial current reduces to the spin in the non-relativistic limit and therefore averages to zero for a background of non-relativistic electrons. The spatial components of the vector current cancel because of isotropy. Therefore, the only non-trivial average is

$$\int d^3p_e f(E_e,T)\Big\langle\langle e(s,p_e)\,|\,\bar{e}(x)\gamma_0 e(x)\,|\,e(s,p_e)\rangle\Big\rangle = n_e(x)\,, \tag{14.51}$$

which gives a contribution to the effective Hamiltonian

$$H_C^{(e)} = \sqrt{2}G_F n_e\bar{\nu}_{eL}(x)\gamma_0\nu_{eL}(x)\,. \tag{14.52}$$

This can be interpreted as a contribution to the $\nu_{eL}$ potential energy

$$V_C = \sqrt{2}G_F n_e\,. \tag{14.53}$$

Should we have considered antineutrino states, we would have ended up with $V_C = -\sqrt{2}G_F n_e$ For a more detailed derivation of the matter potentials see, for example, Ref. [3].

With an equivalent derivation, we find that for $\nu_\mu$ and $\nu_\tau$, the potential due to its CC interactions is zero for most media since neither $\mu$'s nor $\tau's$ are present, while the effective potential for any active neutrino due to the neutral current interactions is found to be

$$V_{NC} = \frac{\sqrt{2}}{2}G_F\left[-n_e(1-4\sin^2\theta_w) + n_p(1-4\sin^2\theta_w) - n_n\right]\,. \tag{14.54}$$

In neutral matter, $n_e = n_p$ and the contribution from electrons and protons cancel each other. So we are left only with the neutron contribution

$$V_{NC} = -1/\sqrt{2} G_F n_n \,. \tag{14.55}$$

After including these effects, the evolution equation for $n$ ultrarelativistic neutrinos propagating in matter written in the mass basis is (see for instance Ref. [27–29] for the derivation):

$$i\frac{d\vec{\nu}}{dx} = H\,\vec{\nu}, \qquad H = H_m + U^{\nu\dagger}\,V\,U^{\nu}\,. \tag{14.56}$$

Here $\vec{\nu} \equiv (\nu_1, \nu_2, \ldots, \nu_n)^T$, $H_m$ is the the kinetic Hamiltonian,

$$H_m = \frac{1}{2E}\,\mathrm{diag}(m_1^2, m_2^2, \ldots, m_n^2), \tag{14.57}$$

and $V$ is the effective neutrino potential in the interaction basis. $U^\nu$ is the $n \times n$ submatrix of the unitary $V^\nu$ matrix corresponding to the $n$ ultrarelativistic neutrino states. For the three SM active neutrinos with purely SM interactions crossing a neutral medium with electrons, protons and neutrons, the evolution equation takes the form (14.56) with $U^\nu \equiv U$, and the effective potential:

$$V = \mathrm{diag}\left(\pm\sqrt{2} G_F n_e(x),\, 0,\, 0\right) \equiv \mathrm{diag}\,(V_e,\, 0,\, 0)\,. \tag{14.58}$$

The sign + (−) in Eq. (14.58) applies to neutrinos (antineutrinos), and $n_e(x)$ is the electron number density in the medium, which in general is not constant along the neutrino trajectory so the potential is not constant. The characteristic value of the potential at the Earth core is $V_e \sim 10^{-13}$ eV, while at the solar core $V_e \sim 10^{-12}$ eV. Since the neutral current potential Eq. (14.55) is flavour diagonal, it can be eliminated from the evolution equation as it only contributes to an overall unobservable phase.

The instantaneous mass eigenstates in matter, $\nu_i^m$, are the eigenstates of the Hamiltonian $H$ in (14.56) for a fixed value of $x$, and they are related to the interaction basis by

$$\vec{\nu} = \tilde{U}(x)\vec{\nu^m}\,. \tag{14.59}$$

The corresponding instantaneous eigenvalues of $H$ are $\mu_i(x)^2/(2E)$ with $\mu_i(x)$ being the instantaneous effective neutrino masses.

Let us take for simplicity a neutrino state which is an admixture of only two neutrino species $|\nu_\alpha\rangle$ and $|\nu_\beta\rangle$, so the two instantaneous mass eigenstates in matter $\nu_1^m$ and $\nu_2^m$ have instantaneous effective neutrino masses

$$\begin{aligned} \mu_{1,2}^2(x) &= \frac{m_1^2 + m_2^2}{2} + E[V_\alpha + V_\beta] \\ \mp\frac{1}{2}&\sqrt{\left[\Delta m^2 \cos 2\theta - A\right]^2 + \left[\Delta m^2 \sin 2\theta\right]^2}\,, \end{aligned} \tag{14.60}$$

and $\tilde{U}(x)$ is a 2x2 rotation matrix with the instantaneous mixing angle in matter given by

$$\tan 2\theta_m = \frac{\Delta m^2 \sin 2\theta}{\Delta m^2 \cos 2\theta - A}\,. \tag{14.61}$$

In the Eqs.(14.60) and (14.61) $A$ is

$$A \equiv 2E(V_\alpha - V_\beta)\,, \tag{14.62}$$

and its sign depends on the composition of the medium and on the flavour composition of the neutrino state considered. From the expressions above, we see that for a given sign of $A$ the mixing angle in matter is larger(smaller) than in vacuum if this last one is in the first (second) octant. We see that the symmetry about $\theta = 45^\circ$ which exists in vacuum oscillations between two neutrino states is broken by the matter potential in propagation in a medium. The expressions above show that signficant effects are present when $A$, is close to $\Delta m^2 \cos 2\theta$. In particular, as seen in Eq. (14.61), the tangent of the mixing angle changes sign if, along its path, the neutrino passes by some matter density region satisfying, for its energy, the *resonance condition*

$$A_R = \Delta m^2 \cos 2\theta \,. \tag{14.63}$$

This implies that if the neutrino is created in a region where the relevant potential satisfies $A_0 > A_R$ ($A_0$ here is the value of the relevant potential at the production point), then the effective mixing angle in matter at the production point is such that $\text{sgn}(\cos 2\theta_{m,0}) = -\,\text{sgn}(\cos 2\theta)$. So the flavour component of the mass eigenstates is inverted as compared to their composition in vacuum. In particular, if at the production point we have $A_0 = 2A_R$, then $\theta_{m,0} = \frac{\pi}{2} - \theta$. Asymptotically, for $A_0 \gg A_R$, $\theta_{m,0} \to \frac{\pi}{2}$. In other words, if in vacuum the lightest (heaviest) mass eigenstate has a larger projection on the flavour $\alpha$ ($\beta$), inside a matter with density and composition such that $A > A_R$, the opposite holds. So if the neutrino system is traveling across a monotonically varying matter potential, the dominant flavour component of a given mass eigenstate changes when crossing the region with $A = A_R$. This phenomenon is known as *level crossing*.

Taking the derivative of Eq. (14.59) with respect to $x$ and using Eq. (14.56), we find that in the instantaneous mass basis the evolution equation reads:

$$i\frac{d\vec{\nu}^m}{dx} = \left[\frac{1}{2E}\,\text{diag}\left(\mu_1^2(x),\,\mu_2^2(x),\,\ldots,\,\mu_n^2(x)\right) - i\,\tilde{U}^\dagger(x)\,\frac{d\tilde{U}(x)}{dx}\right]\vec{\nu}^m \,. \tag{14.64}$$

The presence of the last term, Eq. (14.64) implies that this is a system of coupled equations. So, in general, the instantaneous mass eigenstates, $\nu_i^m$ are not energy eigenstates. For constant or slowly enough varying matter potential this last term can be neglected and the instantaneous mass eigenstates, $\nu_i^m$, behave approximately as energy eigenstates, and they do not mix in the evolution. This is the *adiabatic* transition approximation. On the contrary, when the last term in Eq. (14.64) cannot be neglected, the instantaneous mass eigenstates mix along the neutrino path. This implies there can be *level-jumping* [30–33], and the evolution is *non-adiabatic*.

For adiabatic evolution in matter, the oscillation probability take a form very similar to the vacuum oscillation expression, Eq. (14.39). For example, neglecting $CP$ violation:

$$P_{\alpha\beta} = \left|\sum_i \tilde{U}_{\alpha i}(0)\tilde{U}_{\beta i}(L)\exp\left(-\frac{i}{2E}\int_0^L \mu_i^2(x')dx'\right)\right|^2 \,. \tag{14.65}$$

To compute $P_{\alpha\beta}$ in a varying potential, one can always solve the evolution equation numerically. Also, several analytic approximations for specific profiles of the matter potential can be found in the literature [34].

### 14.5.1 *The Mikheyev-Smirnov-Wolfenstein Effect for Solar Neutrinos*

The matter effects discussed in the previous section are of special relevance for solar neutrinos. As the Sun produces $\nu_e$'s in its core, we consider the propagation of a $\nu_e - \nu_X$ neutrino system ($X$ is some superposition of $\mu$ and $\tau$, which is arbitrary because $\nu_\mu$ and $\nu_\tau$ have only and equal neutral current interactions) in the matter density of the Sun.

The density of solar matter is a monotonically decreasing function of the distance $R$ from the center of the Sun, and it can be approximated by an exponential for $R < 0.9R_\odot$

$$n_e(R) = n_e(0)\exp\left(-R/r_0\right) \ , \tag{14.66}$$

with $r_0 = R_\odot/10.54 = 6.6\times10^7$ m $= 3.3\times10^{14}$ eV$^{-1}$.

As mentioned above, the nuclear reactions in the Sun produce electron neutrinos. After crossing the Sun, the composition of the neutrino state exiting the Sun will depend on the relative size of $\Delta m^2\cos2\theta$ versus $A_0 = 2\,E\,G_F\,n_{e,0}$ (where 0 refers to the neutrino production point, which is near but not exactly at the center of the Sun, $R = 0$).

If the relevant matter potential at production is well below the resonant value, $A_R = \Delta m^2\cos2\theta \gg A_0$, matter effects are negligible. With the characteristic matter density and energy of the solar neutrinos, this condition is fulfilled for values of $\Delta m^2$ such that $\Delta m^2/E \gg L_{\rm Sun-Earth}$. So the propagation occurs as in vacuum with the oscillating phase averaged to 1/2 and the survival probability at the exposed surface of the Earth is

$$P_{ee}(\Delta m^2\cos2\theta \gg A_0) = 1 - \frac{1}{2}\sin^2 2\theta > \frac{1}{2}\,. \tag{14.67}$$

If the relevant matter potential at production is only slightly below the resonant value, $A_R = \Delta m^2\cos2\theta \gtrsim A_0$, the neutrino does not cross a region with resonant density, but matter effects are sizable enough to modify the mixing. The oscillating phase is averaged in the propagation between the Sun and the Earth. This regime is well described by an adiabatic propagation, Eq. (14.65). Using that $\tilde U(0)$ is a 2x2 rotation of angle $\theta_{m,0}$ – the mixing angle in matter at the neutrino production point–, and $\tilde U(L)$ is the corresponding rotation with vacuum mixing angle $\theta$, we get

$$P_{ee}(\Delta m^2\cos2\theta \geq A_0) = \cos^2\theta_{m,0}\cos^2\theta + \sin^2\theta_{m,0}\sin^2\theta = \frac{1}{2}\left[1+\cos2\theta_{m,0}\cos2\theta\right] \ . \tag{14.68}$$

This expression reflects that an electron neutrino produced at $A_0$ is an admixture of $\nu_1$ with fraction $P_{e1,0} = \cos^2\theta_{m,0}$ and $\nu_2$ with fraction $P_{e2,0} = \sin^2\theta_{m,0}$. On exiting the Sun, $\nu_1$ consists of $\nu_e$ with fraction $P_{1e} = \cos^2\theta$, and $\nu_2$ consists of $\nu_e$ with fraction $P_{2e} = \sin^2\theta$ so $P_{ee} = P_{e1,0}P_{1e} + P_{e2,0}P_{2e} = \cos^2\theta_{m,0}\cos^2\theta + \sin^2\theta_{m,0}\sin^2\theta$ [35–37], exactly as given in Eq. (14.68). Since $A_0 < A_R$ the resonance is not crossed so $\cos2\theta_{m,0}$ has the same sign as $\cos2\theta$ and still $P_{ee} \geq 1/2$.

Finally, in the case that $A_R = \Delta m^2\cos2\theta < A_0$, the neutrino can cross the resonance on its way out. In the convention of $\Delta m^2 > 0$ this occurs if $\cos2\theta > 0$ ($\theta < \pi/4$). which means that in vacuum $\nu_e$ is a combination of $\nu_1$ and $\nu_2$ with a larger $\nu_1$ component, while at the production point $\nu_e$ is a combination of $\nu_1^m$ and $\nu_2^m$ with larger $\nu_2^m$ component. In particular, if the density at the production point is much higher than the resonant density, $\Delta m^2\cos2\theta \ll A_0$,

$$\theta_{m,0} = \frac{\pi}{2} \quad \Rightarrow \quad \cos2\theta_{m,0} = -1\,, \tag{14.69}$$

and the produced $\nu_e$ is purely $\nu_2^m$.

In this regime, the evolution of the neutrino ensemble can be adiabatic or non-adiabatic depending on the particular values of $\Delta m^2$ and the mixing angle. The oscillation parameters (see Secs.14.6.1 and 14.7) happen to be such that the transition is adiabatic in all ranges of solar neutrino energies. Thus the survival probability at the exposed surface of the Earth is given by Eq. (14.68) but now with mixing angle (14.69) so

$$P_{ee}(\Delta m^2\cos2\theta < A_0) = \frac{1}{2}\left[1+\cos2\theta_{m,0}\cos2\theta\right] = \sin^2\theta \ . \tag{14.70}$$

So, in this case, $P_{ee}$ can be much smaller than 1/2 because $\cos 2\theta_{m,0}$ and $\cos 2\theta$ have opposite signs. This is referred to as the Mihheev-Smirnov-Wolfenstein (MSW) effect [26,38], which plays a fundamental role in the interpretation of the solar neutrino data.

The resulting energy dependence of the survival probability of solar neutrinos is shown in Fig.14.3 (together with a compilation of data from solar experiments). The plotted curve corresponds to $\Delta m^2 \sim 7.5 \times 10^{-5}$ eV$^2$ and $\sin^2\theta \sim 0.3$ (the so-called large mixing angle, LMA, solution). The figure illustrates the regimes described above. For these values of the oscillation parameters, neutrinos with $E \ll 1$ MeV are in the regime with $\Delta m^2 \cos 2\theta \gg A_0$ so the curve represents the value of vacuum averaged survival probability, Eq. (14.67), and therefore $P_{ee} > 0.5$. For $E > 10$ MeV, on the contrary, $\Delta m^2 \cos 2\theta \ll A_0$ and the survival probability is given by Eq. (14.70), so $P_{ee} = \sin^2\theta \sim 0.3$. In between, the survival probability is given by Eq. (14.68) with $\theta_0$ changing rapidly from its vacuum value to the asymptotic matter value (14.69), 90°.

## 14.6 Experimental Study of Neutrino Oscillations

Neutrino flavor transitions, or neutrino oscillations, have been experimentally studied using various neutrino sources and detection techniques for several decades. For these studies intense sources and large detectors are mandatory because large distances are required for observable oscillation effects and neutrino interaction cross sections are small. Another critical ingredient is knowledge of the neutrino flux before oscillations at a level of precision sufficient to make a definitive measurement of the oscillation effect. This is particularly true for so-called "disappearance" searches, where part of the primary flux oscillates into unseen flavors, as well as for "appearance" measurements, where oscillations induce transitions into a neutrino flavor that is not present, or present in only small quantities, in the primary flux. The following reviews the experimental status of neutrino oscillations organized by different neutrino sources: the Sun, Earth's atmosphere, accelerators, and nuclear reactors. The terminology "disappearance" is often used to describe oscillation measurements where the initial neutrino flavor is observed to decrease, whereas "appearance" is used when another flavor, not present in the original source, is observed.

### 14.6.1 *Solar Neutrinos*

#### 14.6.1.1 *Solar neutrino flux*

Electron neutrinos are produced in the Sun in thermonuclear reactions that generate solar energy. These reactions occur via two main chains, the *pp* chain and the CNO cycle. The *pp* chain includes the reactions $p + p \to d + e^+ + \nu$ (*pp*), $p + e^- + p \to d + \nu$ (*pep*), $^3\mathrm{He} + p \to {}^4\mathrm{He} + e^+ + \nu$ (*hep*), $^7\mathrm{Be} + e^- \to {}^7\mathrm{Li} + \nu(+\gamma)$ ($^7$Be), and $^8\mathrm{B} \to {}^8\mathrm{Be}^* + e^+ + \nu$ ($^8$B). These reactions result in the overall fusion of four protons into a $^4$He nucleus, $4p \to {}^4\mathrm{He} + 2e^+ + 2\nu_e$, where the energy released in the reaction, $Q = 4m_p - m_{^4\mathrm{He}} - 2m_e \sim 26$ MeV, is mostly radiated by photons and only a small fraction is carried by the neutrinos, $\langle E_{2\nu_e} \rangle = 0.59$ MeV. Neutrinos from the CNO cycle are produced via the $^{13}\mathrm{N} \to {}^{13}\mathrm{C} + e^+ + \nu$ ($^{13}$N), $^{15}\mathrm{O} \to {}^{15}\mathrm{N} + e^+ + \nu$ ($^{15}$O), and $^{17}\mathrm{F} \to {}^{17}\mathrm{O} + e^+ + \nu$ ($^{17}$F) reactions. Further, electron capture on $^{13}$N, $^{15}$O, and $^{17}$F produces line spectra of neutrinos called ecCNO neutrinos. Dividing the solar luminosity by the energy released per neutrino production, allows the total neutrino flux to be estimated. In the absence of oscillations, the *pp* solar neutrino flux arriving at Earth is about $6 \times 10^{10}$ cm$^{-2}$s$^{-1}$.

The solar neutrino flux has been calculated based on the Standard Solar Model (SSM). The SSM describes the structure and evolution of the Sun based on a variety of inputs such as its mass, luminosity, radius, surface temperature, age, and surface elemental abundances. To completely describe the flux, knowledge of the absolute nuclear reaction cross sections for the relevant fusion reactions as well radiative opacities are necessary. Bahcall and collaborators continuously updated the SSM calculations over several decades [39, 40]. Figure 14.1 shows the solar neutrino fluxes predicted by the SSM calculation in [41] and ecCNO neutrinos in [42].

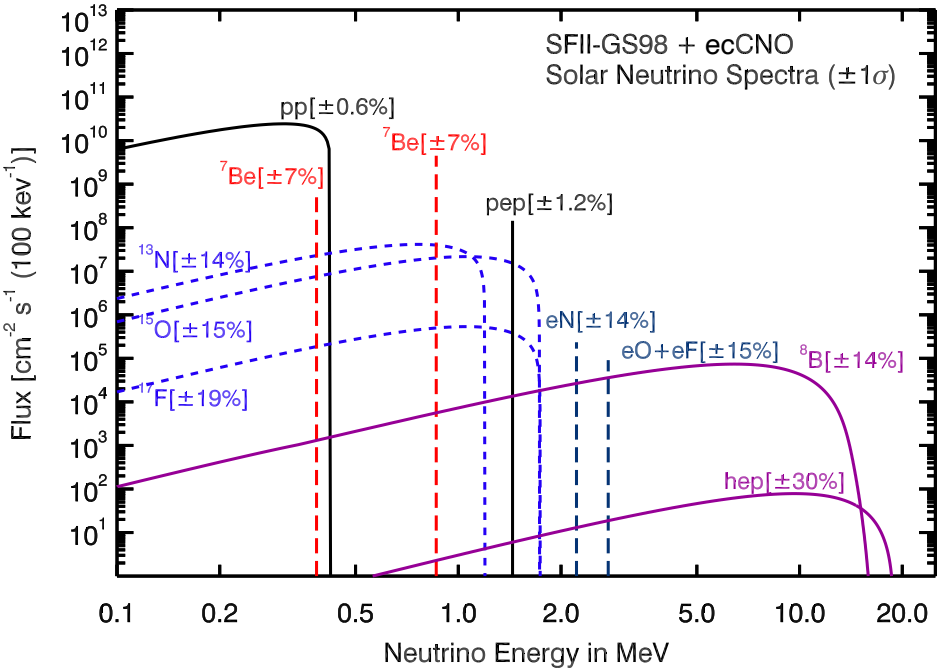


**Figure 14.1:** Spectrum of solar neutrino fluxes predicted by SSM calculation in [41]. In addition to standard fluxes, ecCNO neutrinos have been added based on [42]. Electron capture fluxes are given in $\mathrm{cm}^{-2}\mathrm{s}^{-1}$. Taken from [43].

**Table 14.2:** List of solar neutrino experiments

| Name | Target material | Energy threshold (MeV) | Mass (ton) | Years |
|---|---|---|---|---|
| Homestake | $C_2Cl_4$ | 0.814 | 615 | 1970–1994 |
| SAGE | Ga | 0.233 | 50 | 1989– |
| GALLEX | $GaCl_3$ | 0.233 | 100 [30.3 for Ga] | 1991–1997 |
| GNO | $GaCl_3$ | 0.233 | 100 [30.3 for Ga] | 1998–2003 |
| Kamiokande | $H_2O$ | 6.5 | 3,000 | 1987–1995 |
| Super-Kamiokande | $H_2O$ | 3.5 | 50,000 | 1996– |
| SNO | $D_2O$ | 3.5 | 1,000 | 1999–2006 |
| KamLAND | Liquid scintillator | 0.5/5.5 | 1,000 | 2001– |
| Borexino | Liquid scintillator | 0.19 | 300 | 2007–2021 |

14.6.1.2 *Detection of solar neutrinos and the solar neutrino problem*

Experiments that observe solar neutrinos are summarized in Table 14.2. Starting in the late 1960's, R. Davis and collaborators carried out a pioneering solar neutrino experiment in the Homestake mine [44], utilizing the reaction $\nu_e + {}^{37}\mathrm{Cl} \to e^- + {}^{37}\mathrm{Ar}$. Since this process has an energy threshold of 814 keV, the fluxes of the $^7$Be and $^8$B are the most relevant. The detector contained $\sim 615$ t of $C_2Cl_4$. The produced $^{37}$Ar, with a half-life of 34.8 days, was chemically extracted and introduced into a low-background proportional chamber every few months. Auger electrons from $^{37}$Ar electron capture were counted to determine the neutrino-$^{37}$Cl reaction rate.

From the beginning of the experiment the observed number of neutrinos was nearly one-third

of the SSM prediction. Since this discrepancy could not be traced to deficiencies in either the experiment or theoretical framework it became known as the "solar neutrino problem." The final result from the Homestake experiment was $2.56 \pm 0.16 \pm 0.16$ SNU [45], where SNU (solar neutrino unit) is a unit of event rate with 1 SNU = $10^{-36}$ captures per second per atom. This can be compared with the SSM prediction of $8.46^{+0.87}_{-0.88}$ SNU [46].

Detecting neutrinos from other production processes was recognized as important to investigate the origin of the solar neutrino problem. The *pp* neutrinos are particularly useful for this purpose as they are the most abundant and have the smallest flux uncertainty. They can be observed using a radiochemical reaction with gallium, $\nu_e + {}^{71}\mathrm{Ga} \to e^- + {}^{71}\mathrm{Ge}$, which has an energy threshold of 233 keV. According to the SSM, more than half of the events on $^{71}$Ga are due to *pp* neutrinos, with the second most dominant contribution coming from $^{7}$Be neutrinos. Generated $^{71}$Ge nuclei decay via electron capture with a half-life of 11.4 days and can be chemically extracted. The SAGE experiment in Baksan [47] used about 50 t of liquid metallic gallium as a target, whereas the GALLEX experiment at LNGS [48] used 101 t of $GaCl_3$, containing 30.3 t of gallium. Both experiments used natural gallium, 39.9% of which is the $^{71}$Ga isotope. GALLEX was followed by its successor, the GNO experiment. The measured capture rates were $69.3 \pm 4.1 \pm 3.6$ SNU for GALLEX+GNO [49] and $65.4^{+3.1+2.6}_{-3.0-2.8}$ SNU for SAGE [50], which are well below the SSM prediction of $127.9^{+8.1}_{-8.2}$ SNU [46].

While radiochemical detectors measure the reaction rate integrated between extractions, the first real-time measurement of solar neutrinos was realized by the Kamiokande experiment [51] and later by its successor, Super-Kamiokande. The Kamiokande detector was an upright cylindrical 3,000-t water Cherenkov detector in the Kamioka mine that operated throughout the 1980's. Super-Kamiokande started operations in 1996, employing a similar, but much larger design containing 50 kt of ultrapure water [4]. An inner detector volume corresponding to a 32 kt water mass is viewed by more than 11,000 inward-facing 50 cm diameter photomultiplier tubes (PMTs). Kamiokande and Super-Kamiokande observe solar neutrinos using $\nu$-$e$ elastic scattering (ES), $\nu_x + e^- \to \nu_x + e^-$. This reaction occurs via both charged and neutral current (NC) pathways and is therefore sensitive to all active neutrino flavors. However, the cross-section for $\nu_e$, which is the only flavor to interact via the charged current, is about six times larger than that for $\nu_\mu$ or $\nu_\tau$. Since the energy threshold was 6.5 MeV in Kamiokande and is 3.5 MeV[5] for the present Super-Kamiokande these experiments are primarily sensitive to $^{8}$B neutrinos.

The results from both Kamiokande [52] and Super-Kamiokande [53] show significantly smaller solar neutrino rates compared to predictions. Super-Kamiokande's most recent solar neutrino flux measurement is $(2.345 \pm 0.014 \pm 0.036) \times 10^6$ cm$^{-2}$s$^{-1}$ [54], while the prediction based on the SSM is $(5.46 \pm 0.66) \times 10^6$ cm$^{-2}$s$^{-1}$ [55]. No significant zenith angle variation or spectral distortions were observed in the initial phase of Super-Kamiokande, which placed strong constraints on the solution of the solar neutrino problem [56].

#### 14.6.1.3 *Solution of the solar neutrino problem*

The SNO experiment in Canada used 1,000 t of heavy water ($D_2O$) contained in a spherical acrylic vessel which was surrounded by a water ($H_2O$) shield. An array of PMTs installed on a stainless steel structure detected Cherenkov radiation produced in both the $D_2O$ and $H_2O$. SNO observed $^{8}$B neutrinos using the ES channel as well as two other interactions specific to its $D_2O$ target, the CC $\nu_e + d \to e^- + p + p$ and the NC $\nu_x + d \to \nu_x + p + n$ interactions. Importantly, the CC interaction is sensitive to only $\nu_e$, while the NC interaction is sensitive to all active flavors of neutrinos with equal cross-sections for all. By comparing measurements of these different

[4] Recently, gadolinium (0.01% by weight in 2020, 0.03% in 2022) has been loaded to the water to enhance the detector's neutron tagging capabilities.

[5] Based on the recoil electron's kinetic energy

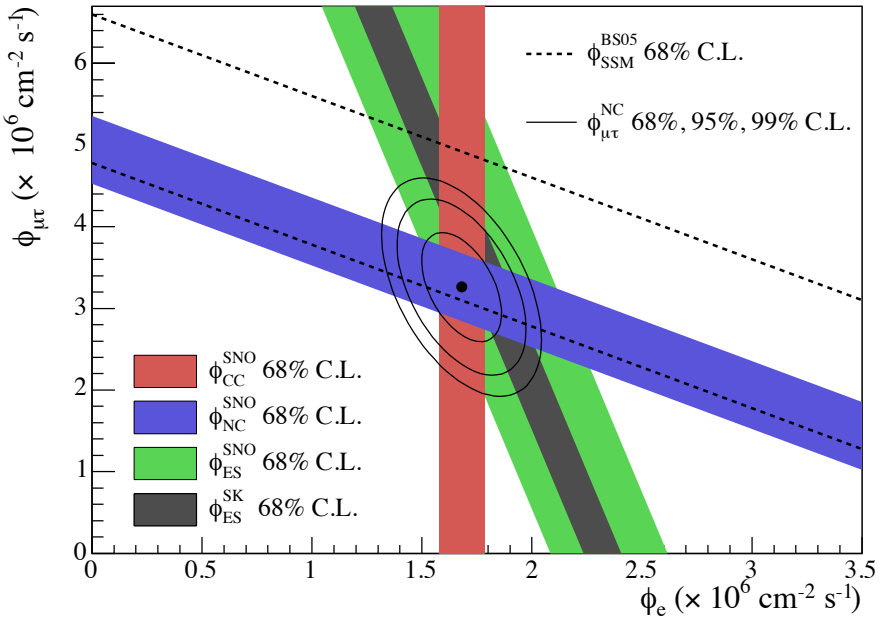


**Figure 14.2:** Fluxes of $^8$B solar neutrinos, $\phi(\nu_e)$, and $\phi(\nu_{\mu,\tau})$, deduced from the SNO's CC, ES, and NC results [58]. The Super-Kamiokande ES flux is from [59]. The BS05(OP) standard solar model prediction [40] is also shown. The bands represent the $1\sigma$ error. The contours show the 68%, 95%, and 99% joint probability for $\phi(\nu_e)$ and $\phi(\nu_{\mu,\tau})$. The figure is from [58].

interactions, SNO provides a model-independent test of neutrino flavor change [57].

In 2001 SNO reported its initial CC measurement [60], which when combined with the high statistics measurement of $\nu$-$e$ elastic scattering from Super-Kamiokande [61], provided direct evidence for the existence of a non-$\nu_e$ component in solar neutrino flux. SNO's subsequent NC result in 2002 [62] established the existence of this component with $5.3\sigma$ significance. Figure 14.2 shows SNO's measured electron neutrino ($\phi(\nu_e)$) and combined muon and tau neutrino fluxes ($\phi(\nu_{\mu,\tau})$) at various confidence levels together with prediction from the SSM. These results together with measurements from the reactor neutrino experiment KamLAND (see Sec. 14.6.4), finally proved that the so-called large mixing angle (LMA) solution, which describes MSW-driven adiabatic flavor transitions in the solar matter, was the resolution of the solar neutrino problem. From a combined result of three phases of SNO data [63], the total flux of $^8$B solar neutrino is found to be $(5.25 \pm 0.16^{+0.11}_{-0.13})$ cm$^{-2}$s$^{-1}$, consistent with the SSM prediction. This consistency is one of the major accomplishments of SSM.

In order to understand the SSM as well as to study the MSW effect on solar neutrinos, it is important to measure fluxes other than the $^8$B. The Borexino experiment at Gran Sasso detected solar neutrino via $\nu$-e scattering using 300 t of ultra-pure liquid scintillator. It achieved a 0.19 MeV energy threshold with 5% energy resolution at 1 MeV, enabling Borexino to make the first real-time detection of $^7$Be solar neutrinos [65]. Further, the experiment also measured the *pep* [66], *pp* [67], and CNO [68] neutrino fluxes for the first time. Together with its $^8$B [69] neutrino flux, Borexino provides both high- and low-energy measurements to probe the solar MSW effect. Figure 14.3 shows the survival probability of solar $\nu_e$ as a function of neutrino energy with data from Borexino [70,71] and SNO+SK $^8$B measurements overlaid with the theoretical curve from the MSW-LMA solution. The data are consistent with the prediction. Though not included in the figure, the KamLAND experiment has also measured $^8$B [72] and $^7$Be [73] solar neutrinos.

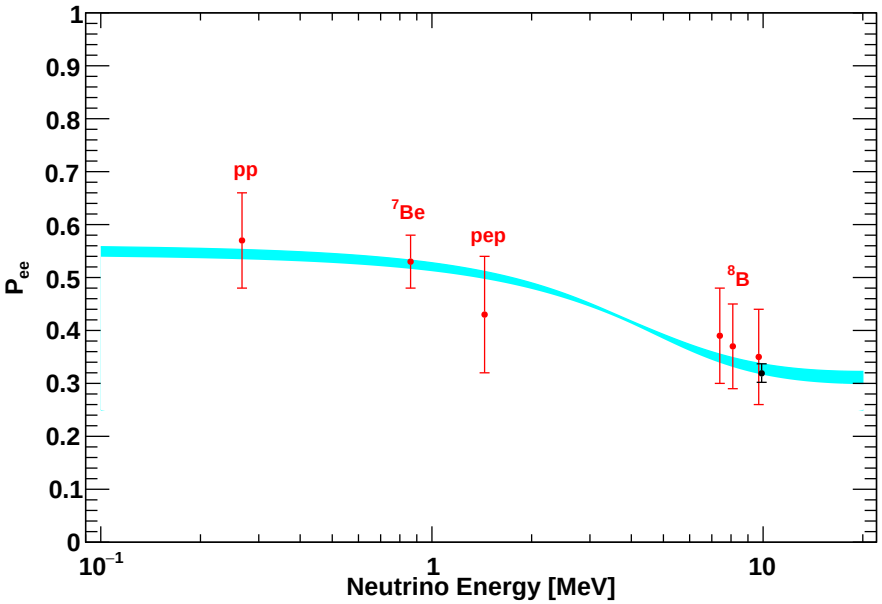


**Figure 14.3:** Electron neutrino survival probability as a function of neutrino energy. The points represent, from left to right, the Borexino pp, $^{7}$Be, pep, and $^{8}$B data (red points) and the SNO+SK $^{8}$B data (black point). The three Borexino $^{8}$B data points correspond, from left to right, to the low-energy (LE) range, LE+HE range, and the high-energy (HE) range. The electron neutrino survival probabilities from experimental points are determined using a high metallicity SSM from [55]. The error bars represent the $\pm 1\sigma$ experimental + theoretical uncertainties. The curve corresponds to the $\pm 1\sigma$ prediction of the MSW-LMA solution using the parameter values given in [64]. This figure is provided by A. Ianni.

Matter effects within the Earth are also expected to affect the propagation of solar neutrinos when they are detected during the night. Comparison of the measured event rates during daytime and nighttime therefore provides a clean and direct test of those matter effects on neutrino oscillations. Super-Kamiokande reported an indication of a day-night asymmetry in the $^{8}$B solar neutrino flux [54]. This asymmetry, defined as the difference of the average interaction rate during the day and the average at night divided by the average of the two, is $(-3.3 \pm 1.0(\text{stat.}) \pm 0.5(\text{syst.}))\%$, corresponding to a statistical significance of $2.9\sigma$.

### 14.6.2 *Atmospheric Neutrinos*

#### 14.6.2.1 *Atmospheric neutrino flux*

Atmospheric neutrinos are produced by the decays of hadrons, pions and kaons at low energies, generated in the interactions of cosmic rays and nucleons in the Earth's atmosphere. They have energies ranging from ∼0.1 GeV to TeV and beyond. Since the cosmic ray flux impinges on the atmosphere from all directions, atmospheric neutrinos can travel between ∼10 and $\sim 10^4$ km before detection. This combination of energies and pathlengths make them a broad probe of the $L/E$ nature of oscillations (c.f. Equation 14.39). Importantly for oscillation studies, the atmospheric neutrino flux below 100 GeV is composed of electron and muon neutrinos as well as their antineutrinos, where as the tau flavors do not populate the flux appreciably until higher energies.

Based on the dominant atmospheric neutrino production modes, it is possible to understand the ratios of the different flavors' fluxes without detailed calculations. From the decay chain of the

charged pion $\pi^+ \to \mu^+\nu_\mu$ and the subsequent muon decay $\mu^+ \to e^+\nu_e\bar{\nu}_\mu$ (and the charge conjugate decays for the $\pi^-$ chain), the flux ratio $(\nu_\mu+\bar{\nu}_\mu)/(\nu_e+\bar{\nu}_e)$ is expected to be around 2 at low energies ($\sim 1$ GeV), where most muons decay in the atmosphere. At higher energies some muons will reach the Earth before decaying, increasing this ratio. Further, at O(10) GeV and above, the isotropy of the primary cosmic ray flux implies the neutrino fluxes are up-down symmetric above O(1) GeV. At lower energies the cosmic rays are deflected in the geomagnetic field, inducing up-down asymmetries in the neutrino flux.

Atmospheric neutrino fluxes are calculated in detail using the primary cosmic ray spectrum and particle composition as well as hadronic interaction cross sections to simulate interactions in the atmosphere. Generated particles are tracked through the atmosphere accounting for additional interactions with air nuclei before decaying to produce neutrinos. Effects from solar activity and the propagation in the geomagnetic field are taken into account. Several groups have produced flux estimates for terrestrial detectors [74–77]. Typically the absolute flux is uncertain to 10–20%, depending upon the energy range, while the flux ratios are more precisely constrained, varying by less than 5%.

14.6.2.2 *Observation of atmospheric neutrino oscillations*

The first detection of atmospheric neutrinos was reported in the 1960's by the underground experiments in the Kolar Gold Field in India [78] and in South Africa [79]. In the 1980's, experiments searching for nucleon decays started operations with detectors large enough to observe their dominant background source, atmospheric neutrinos. Among the early experiments were the water Cherenkov experiments, Kamiokande [80] and IMB [81], and the iron tracking calorimeters, Frejus [82] and NUSEX [83]. These detectors identify the incident atmospheric neutrino flavor via its charged current interactions with nuclei, which produce the corresponding flavor of charged lepton.

Early atmospheric neutrino measurements focused on the flux ratio, $\nu_\mu/\nu_e \equiv (\nu_\mu+\bar{\nu}_\mu)/(\nu_e+\bar{\nu}_e)$, as well as the double ratio of this quantity with its expected value, $(\nu_\mu/\nu_e)_{\rm obs}/(\nu_\mu/\nu_e)_{\rm exp}$, in order to reduce the impact of flux uncertainties. The Kamiokande experiment reported an indication of a deficit of the $(\nu_\mu + \bar{\nu}_\mu)$ flux [80], which IMB also observed [81]. However, observations from the iron calorimeters, Frejus [82] and NUSEX [83], were consistent with predictions. This discrepancy became known as the atmospheric neutrino anomaly. Kamiokande later reported studies with a larger sub-GeV ($< 1.33$ GeV) [84] data as well as with multi-GeV ($> 1.33$ GeV) [85] samples that strengthened the muon flavor deficit observation. The latter reported an analysis of zenith angle distributions, which showed an indication that the muon disappearance probability is dependent on the zenith angle and hence the travel length of neutrinos. However, the statistical significance was not sufficient to provide a conclusive interpretation.

The resolution of the atmospheric neutrino anomaly was achieved by Super-Kamiokande, which reported compelling evidence for atmospheric neutrino oscillations in 1998 [86]. Zenith angle ($\theta_z$, with $\theta_z = 0$ for vertically downward-going) data showed a clear deficit of upward-going muon-like neutrino events, while no significant asymmetry was observed for electron-like events. Defining the up-down asymmetry as $A = (U - D)/(U + D)$, where $U$ is the number of upward-going ($-1 < \cos\theta_{\rm z} < -0.2$) events and $D$ is the number of downward-going ($0.2 < \cos\theta_{\rm z} < 1.0$) events, the Super-Kamiokande multi-GeV muon-like data alone had $A = -0.296 \pm 0.048 \pm 0.001$, a $6\sigma$ deviation from zero. Other data samples, including the sub-GeV ($< 1.33$ GeV) muon-like, upward through going, and upward stopping $\mu$ samples, which together a span several decades in neutrino energy showed similar distortions of varying degrees. Super-Kamiokande's results were later confirmed by other atmospheric neutrino observations from MACRO [87] and Soudan2 [88].

Although the energy and zenith-angle-dependent muon neutrino disappearance observed with atmospheric neutrinos could be consistently explained by neutrino oscillations predominantly be-

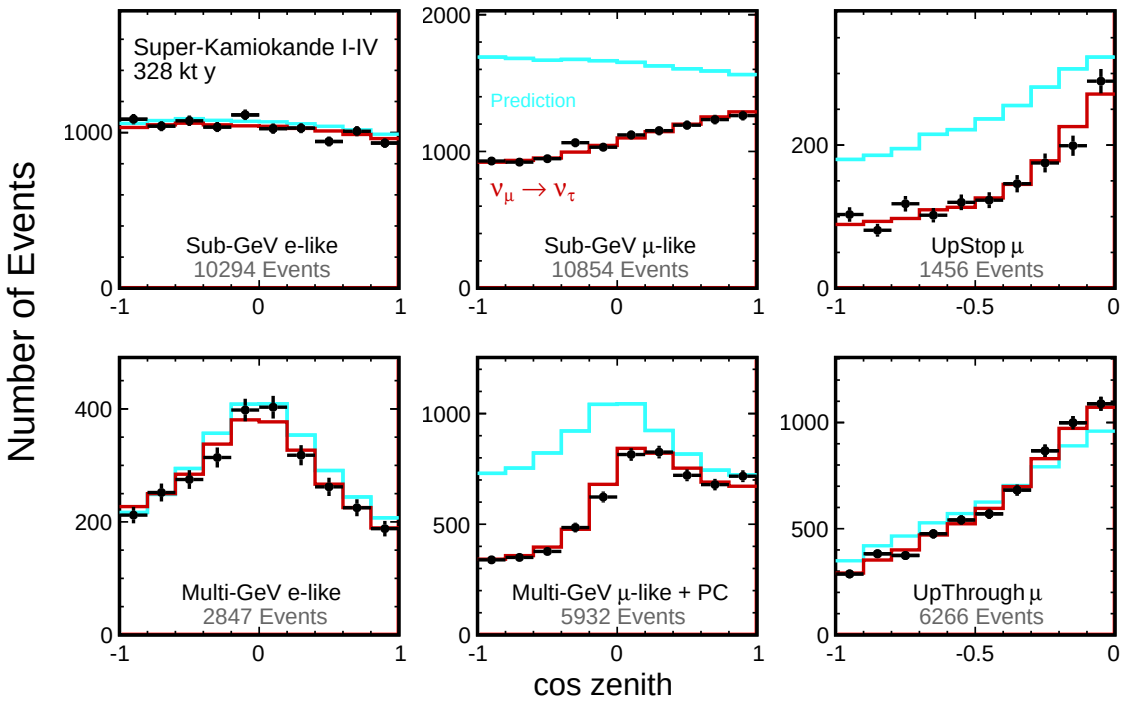


**Figure 14.4:** Zenith angle distributions of Super-Kamiokande atmospheric neutrino events corresponding to a 328 kton-year exposure of the detector. Fully contained 1-ring $e$-like and $\mu$-like events with visible energy $< 1.33$ GeV (sub-GeV) and $> 1.33$ GeV (multi-GeV), as well as upward stopping and upward through going $\mu$ samples are shown. Partially contained (PC) events are combined with multi-GeV $\mu$-like events. Blue histograms show the non-oscillated Monte Carlo prediction and red histograms show the best-fit expectation for neutrino oscillations. (Figure is provided by the Super-Kamiokande Collaboration)

tween $\nu_\mu$ and $\nu_\tau$, other exotic explanations such as neutrino decay [89] and decoherence [90] could not be ruled out initially. Using a selected sample from Super-Kamiokande's atmospheric data with good measured $L/E$ resolution, the $L/E$ dependence of the survival probability was measured [91]. The observed dip in the $L/E$ distribution was consistent with the expectation from neutrino oscillation, strongly disfavoring alternative models.

The strongest experimental proof of $\nu_\mu$-$\nu_\tau$ oscillations in atmospheric neutrino experiments is observation of the appearance of oscillation-induced $\nu_\tau$. However, the high production threshold of the $\tau$ in CC $\nu_\tau$ interactions, 3.5 GeV, coupled with its short lifetime (0.3 ps) and decays into several particles, makes identifying $\nu_\tau$ appearance events experimentally challenging. Nonetheless, Super-Kamiokande has reported evidence of tau neutrino appearance using atmospheric neutrino data with $4.6\sigma$ significance [92]. Recently, IceCube has also reported evidence ($3.2\sigma$) of $\nu_\tau$ appearance [93] using atmospheric neutrinos. Definitive observation of $\nu_\tau$ appearance, however, was made by the long-baseline experiment, OPERA (See Sec. 14.6.3.3).

14.6.2.3 *Neutrino oscillation measurements using atmospheric neutrinos*

Figure 14.4 shows the zenith angle distributions of atmospheric neutrino data from Super-Kamiokande. For a wide range of neutrino energies and path lengths, the observed distributions are consistent with the expectation from neutrino oscillation. Upward-going atmospheric neutrinos with energies from a few to ∼10 GeV provide information for the determination of the neutrino

mass ordering [94].

Neutrino telescopes primarily built for high-energy neutrino astronomy, such as ANTARES and IceCube, also measure neutrino oscillations with atmospheric neutrinos. ANTARES consists of a sparse array of PMTs deployed under the Mediterranean Sea at a depth of about 2.5 km that instruments a $10^5$ m$^3$ volume. Similarly, the IceCube detector is located in the Antarctic ice near the South Pole with PMTs deployed depths between 1.45 and 2.45 km. The bottom center of the detector houses DeepCore, a low energy extension to the experiment instrumenting a $\sim 10^7$ m$^3$ volume with a denser PMT array. Both ANTARES [95], with a 20 GeV threshold, and IceCube [96], with events reconstructed above about 5 GeV, have observed atmospheric $\nu_\mu$ disappearance. Despite the larger threshold, the latter's oscillation constraints have similar precision to those from long-baseline accelerator experiments.

There are several projects for atmospheric neutrino observations either proposed or under preparation. The atmospheric neutrino observation program is included in the plans for future neutrino telescopes such as the IceCube Upgrade [97] and the ORCA detector of KM3NeT project [98]. Indeed, with only 5% of the detector installed and instrumenting a $4 \times 10^5$ m$^3$ volume, the ORCA6 detector has observed atmospheric neutrino oscillations [99]. In India a 50 kt magnetized iron tracking calorimeter ICAL is planned at the INO [100]. Future large underground detectors, Hyper-Kamiokande in Japan [101] and DUNE in US [102] will also study the atmospheric neutrinos.

### 14.6.3 *Accelerator Neutrinos*

14.6.3.1 *Accelerator neutrino beams*

Conventional neutrino beams are produced with accelerators by colliding high-energy protons onto a target, producing $\pi$ and $K$, which are then allowed to decay in a low-density volume, producing neutrinos. Undecayed mesons and muons are stopped in beam dumps or soil downstream of this volume. Since pions are the most abundant product of the proton-target collisions, a conventional neutrino beams are predominantly composed of muon-type neutrinos (or antineutrinos). A comprehensive description of accelerator neutrino beams is found in [103].

Focusing devices called magnetic horns are used to concentrate the neutrino beam flux in the desired direction [104]. A magnetic horn is a pulsed electromagnet with toroidal magnetic fields that focus (or defocus) the charged particles that are neutrino parents. One can therefore enrich the beam in either neutrinos or antineutrinos by selecting the direction of the horn's current, and hence the magnetic field direction, to focus positive or negative particles, respectively. Even with this focusing, there are still neutrinos from the opposite charge-sign particle decays, so-called *wrong sign* neutrinos, contaminating the beam. There is also a small amount of $\nu_e$ and $\bar{\nu}_e$ contamination coming primarily from kaon and muon decays.

To maximize the sensitivity of an experiment, the ratio of the baseline and neutrino energy $(L/E)$ is chosen to match the oscillation effects to be studied. Maximizing the flux of neutrinos with the desired energy, while suppressing other energies, is important for precise oscillation studies. The energy of neutrinos from pion decays is given by

$$E_\nu = \frac{[1 - (m_\mu/m_\pi)^2]E_\pi}{1 + \gamma^2\theta^2}, \tag{14.71}$$

where $E_\nu$ and $E_\pi$ are the energy of neutrino and pion, respectively, $\theta$ is the angle between the pion and neutrino directions, and $\gamma = E_\pi/m_\pi$. For $\theta = 0$, representing so-called *on-axis* neutrinos, the neutrino energy is linearly proportional to the pion energy. In this scenario a narrow band neutrino beam can be made by selecting pions with a desired momentum. Both the MINOS [105] and K2K [106] experiments were operated on-axis. On the other hand, for other angles, the neutrino energy is not strongly dependent on the parent pion energy for a wide range energies, but is instead

dependent on the *off-axis* angle $\theta$. Using this relation a narrow band neutrino beam centered around the energy determined by $\theta$ can be produced. This off-axis beam method was first introduced in the BNL E889 proposal [107] and adopted in T2K [108] and NOvA [109] experiments. For a list of neutrino beamlines, see also Chapter 33 of this *Review*, "Neutrino Beam Lines at High-Energy Proton Synchrotrons."

The so-called atmospheric mass splitting observed by atmospheric neutrino oscillation experiments, $\Delta m^2 \sim 2.5 \times 10^{-3}$ eV$^2$, gives rise to a first maximum in the oscillation probability when $L/E \sim 500$ km/GeV. As indicated in Table 14.1, accelerator experiments studying oscillations around this mass splitting have baselines with a $\sim 1$ GeV neutrino beam require a baseline of a few hundred to a thousand km. For this reason such experiments are termed "long-baseline" experiments. On the other hand, for neutrino oscillations at the $\Delta m^2 \sim 1$ eV$^2$ scale, as has been reported in some experiments, a $\sim 1$ km baseline is needed for the same neutrino energies. Accordingly, these experiments are often called "short-baseline" experiments.

Determining the flux of a neutrino beam is done using Monte Carlo simulation of the beamline constrained by in-situ measurements of the primary proton beam as well as beamline components. An important ingredient to the neutrino flux prediction is the hadron production and interaction cross-sections, not only for modeling the initial particle generation in the target, but also to track their subsequent interactions with materials in the beamline, such as the magnetic focusing horns and shielding materials. Data from dedicated hadron production experiments [110–113] are used to tune the beam simulation and to constrain flux uncertainties. The uncertainty on the predicted neutrino flux for the most relevant energy region is 5–10% based on the latest hadron production data [114–116].

14.6.3.2 *Near detectors and neutrino interaction cross sections*

Many long-baseline experiments use two detectors to reduce systematic uncertainties arising from neutrino flux and neutrino-nucleus interactions. Near detectors, situated close enough to the neutrino production target that oscillation effects are small, follow two generic design schemes. They either use the same detection technology as the far detector, itself situated at baseline long enough to observe significant oscillation effects, or they consist of sub-detectors with complementary functions to obtain detailed information of the neutrino beam and neutrino-nucleus interactions. The near detectors provide in-situ measurements of the neutrino flux, energy spectrum, and interaction cross-sections, which are then used as inputs to predict the event rate at the far detector. However, even with a two-detector configuration, the neutrino flux and energy spectrum is inevitably different between the near and the far detectors, due to distortions from the oscillation effect. Further, while near detectors observe the neutrino beam as line source, the same beam appears as point source at the far detector.

As modern experiments use heavy nuclei as the neutrino interaction target, primary interactions on correlated nucleons as well as the particles produced in subsequent interactions within the nuclear environment can alter the observed final state, potentially biasing oscillation measurements. In order to make precise oscillation measurements at long-baseline experiments, a detailed understanding of neutrino-nucleus interactions is therefore crucial, particularly for experiments where final-state hadronic activity is not observable. The current status of neutrino cross-sections is summarized in Chapter 52 of this *Review*, "Neutrino Cross Section Measurements."

14.6.3.3 *Long-baseline experiments*

Table 14.3 summarizes long-baseline neutrino oscillation experiments. K2K was the first long-baseline experiment and used a neutrino beam directed towards Super-Kamiokande with a 250 km baseline. Neutrinos were generated with the KEK 12 GeV proton synchrotron and had an average energy of 1.3 GeV. The experiment used a set of fine-grained detectors and a 1 kt water

**Table 14.3:** List of long-baseline neutrino oscillation experiments

| Name | Beamline | Far Detector | L (km) | $E_\nu$ (GeV) | Year | Orientation |
|---|---|---|---|---|---|---|
| K2K | KEK-PS | Water Cherenkov | 250 | 1.3 | 1999–2004 | On-axis |
| MINOS | NuMI | Iron-scintillator | 735 | 3 | 2005–2013 | On-axis |
| MINOS+ | NuMI | Iron-scintillator | 735 | 7 | 2013–2016 | On-axis |
| OPERA | CNGS | Emulsion hybrid | 730 | 17 | 2008–2012 | On-axis |
| ICARUS | CNGS | Liquid argon TPC | 730 | 17 | 2010–2012 | On-axis |
| T2K | J-PARC | Water Cherenkov | 295 | 0.6 | 2010– | Off-axis |
| NOvA | NuMI | Liquid scint. tracking calorimeter | 810 | 2 | 2014– | Off-axis |
| DUNE | LBNF | Liquid argon TPC | 1300 | 2–3 | On-axis | |
| Hyper-Kamiokande | J-PARC | Water Cherenkov | 295 | 0.6 | Off-axis | |

Cherenkov detector located 300 m downstream of the neutrino production target for its near detectors. K2K confirmed the muon neutrino disappearance originally reported by Super-Kamiokande's atmospheric neutrino observation [117].

The MINOS experiment used a beam from Fermilab and a detector located 735 km away in the Soudan mine. Neutrinos were produced in the NuMI beamline using 120 GeV protons from the Main Injector. Both the near and far detectors were iron-scintillator tracking calorimeters, 0.98 kt and 5.4 kt, respectively, with toroidal magnetic fields to enable charge-sign selection of muons. By varying the relative positions of the neutrino target and focusing horns, the energy spectrum of neutrinos from NuMI could be changed. Most of the MINOS data were taken in the "low energy" configuration, which produced a peak energy of around 3 GeV. For a three-year period starting in 2013 the experiment was operated as MINOS+ with NuMI in the "medium energy" configuration which produced a peak neutrino energy of around 7 GeV. MINOS and MINOS+ combined accelerator and atmospheric neutrino data in both disappearance and appearance modes to measure oscillation parameters [118, 119].

In Europe, the CNGS neutrino beamline provided a neutrino beam with a mean energy of 17 GeV along a 750 km baseline from CERN to LNGS. The beam energy was chosen so that oscillation-induced $\nu_\tau$ had enough energy to undergo CC interactions and therefore provide confirmation of $\nu_\tau$ appearance. Since there are no $\nu_\tau$ in the beam before oscillations, no near detector was needed. The OPERA experiment's single detector used consisted of an emulsion-lead target with about 1.25 kt total mass, complemented by electronic detectors. The excellent spatial resolution of the emulsion enabled the event-by-event identification of $\tau$ leptons. Ultimately, OPERA observed ten $\nu_\tau$ CC candidate events with an expected background of $2.0\pm0.4$ [120], observing $\nu_\mu \to \nu_\tau$ appearance with a significance of $6.1\sigma$. Another neutrino experiment, ICARUS [121], which used 600 t liquid argon time projection chambers (TPCs), was operated at Gran Sasso from 2010 to 2012.

This first generation of long-baseline experiments confirmed the existence of neutrino oscillations in the $\nu_\mu \to \nu_\tau$ channel dominated by the atmospheric mixing parameters. Oscillations from $\nu_\mu$ to $\nu_e$, induced by non-zero $\theta_{13}$ (see Eq. 14.33), became the focus of second-generation experiments, which are still running today. This appearance channel opens the possibility of studying several still-open problems in neutrino mixing, including neutrino $CP$ violation, determination of the neutrino mass ordering, and determination of the $\theta_{23}$ octant.

The T2K experiment started in 2010 using a newly constructed high-intensity proton synchrotron at J-PARC and Super-Kamiokande as its far detector, located 295 km away. It employs

a set of near detectors at about 280 m from the production target with several nuclear targets, including water. T2K is the first long-baseline experiment to employ the off-axis technique, directing its beam 2.5° away from Super-Kamiokande. At this angle the neutrino energy spectrum peaks at 0.6 GeV, which corresponds to first oscillation maximum for the atmospheric mass splitting, $\Delta m^2 \sim 2.5 \times 10^{-3}$ eV$^2$.

In 2011, T2K reported the first indication of $\nu_\mu \to \nu_e$ oscillations with a statistical significance of $2.5\sigma$ [122]. Later T2K established oscillation into this appearance channel with more than $7\sigma$ 2014 [123]. Figure 14.5 shows T2K's muon neutrino and electron neutrino candidates' kinematic distributions from both its neutrino and antineutrino beam data. Using a combined analysis of all of its data, T2K reported a hint of $CP$ violation at the $2\sigma$ level [124].

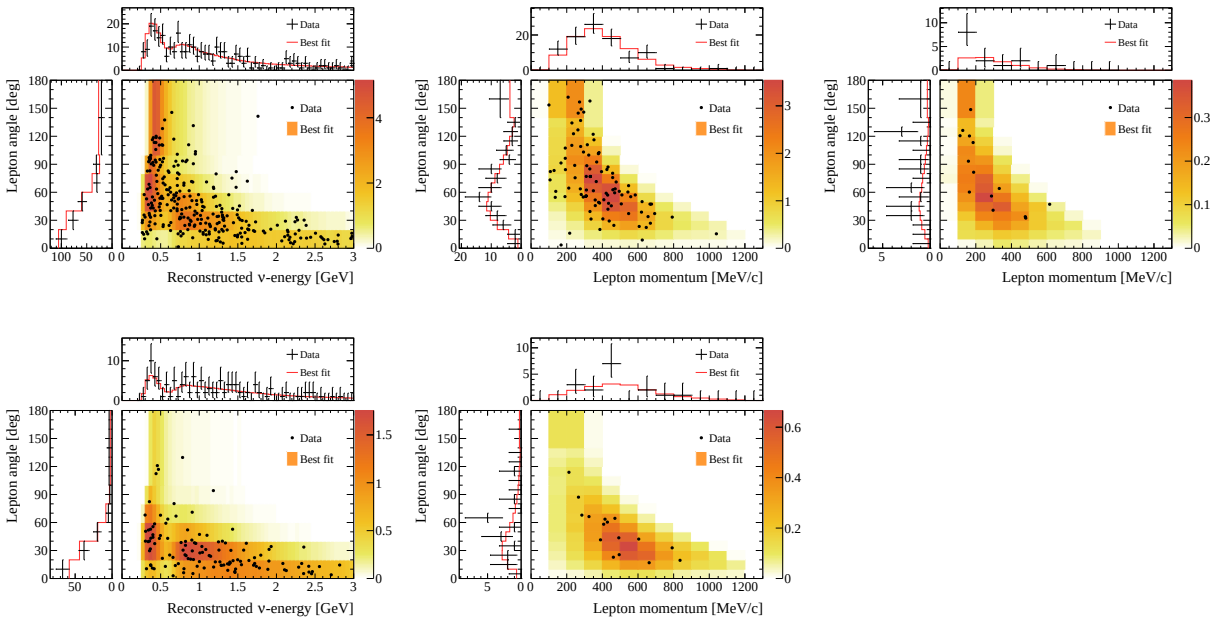


**Figure 14.5:** Observed kinematic distributions from T2K compared to the expectations with the best-fit parameters [124]. Top and bottom panels correspond to data from neutrino and antineutrino beam mode, respectively. Left, middle, and right panels show distributions for single ring $\mu$-like events, single ring $e$-like events with no associated decay electron, and single ring $e$-like events with one associated decay electron (only for neutrino beam mode data), respectively.

The NOvA experiment uses the upgraded NuMI beamline in an off-axis configuration, with functionally equivalent near and far detectors. Its 14 kt far detector is located near Ash River, Minnesota, 810 km away from the neutrino source. The near detector is around 1 km downstream of the production target and has a total active mass of 290 t. Both detectors are tracking calorimeters consisting of planes of polyvinyl chloride cells filled with liquid scintillator and alternately arrayed vertical and horizontal orientations. At 14.6 mrad off-axis of the NuMI beam, the neutrino energy at the far detector peaks at around 2 GeV.

NOvA's physics run started in 2014 and quickly confirmed oscillations from $\nu_\mu$ to $\nu_e$ [125], The experiment started operating its antineutrino beam in 2016 and has reported an observation of $\bar{\nu}_e$ appearance in its $\bar{\nu}_\mu$ beam with $4.4\sigma$ significance [126]. Figure 14.6 shows reconstructed neutrino energy distributions from NOvA [127]. The data do not show a strong asymmetry in the rates of $\nu_e$ and $\bar{\nu}_e$ appearance, excluding $\delta_{\rm CP} = 90°$ for the inverted mass ordering ($m_3 < m_1 < m_2$, see

Sec. 14.7 for definitions) at more than $3\sigma$ and disfavoring $\delta_{\rm CP} = 270°$ assuming the normal mass ordering ($m_1 < m_2 < m_3$, see Sec. 14.7 for definitions) at more than $2\sigma$.

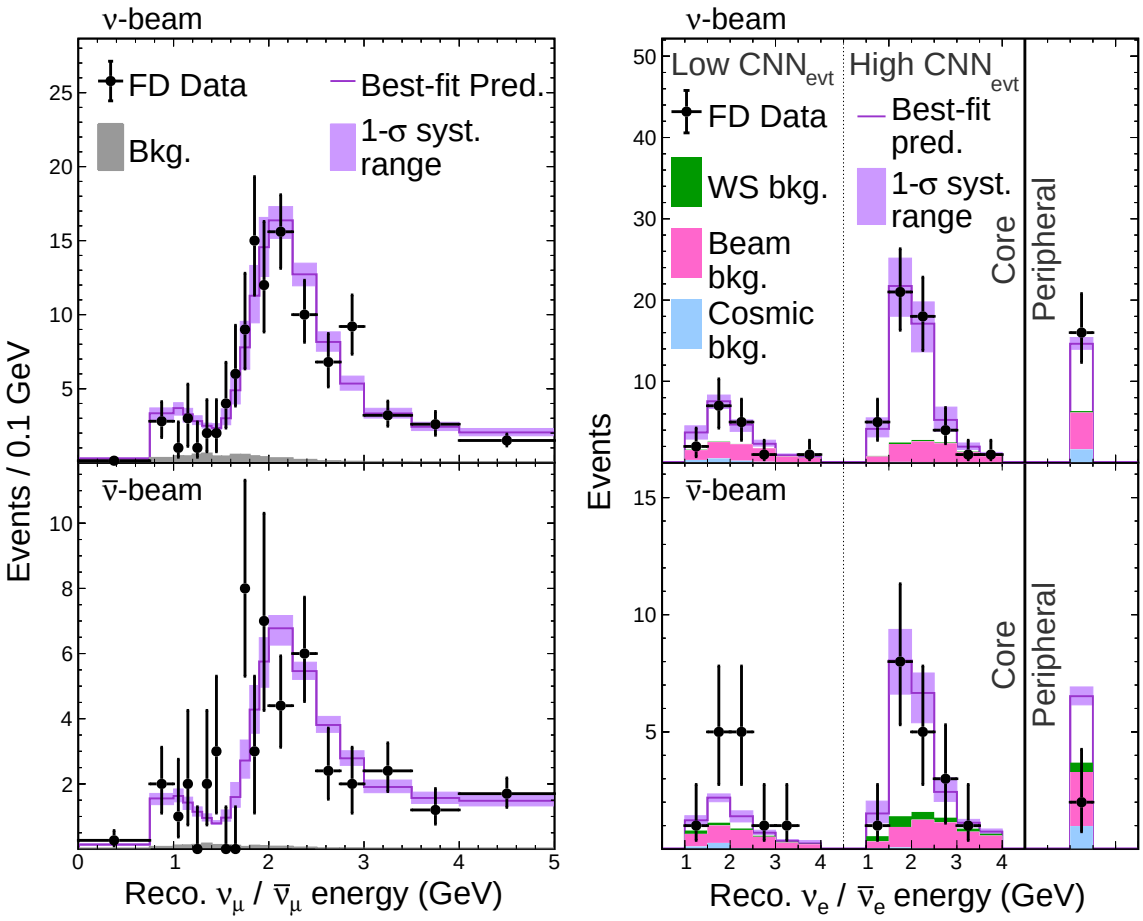


**Figure 14.6:** Reconstructed neutrino energy distributions from the NOvA far detector [127]. Top plots are for neutrino beam mode, and bottom plots are for antineutrino beam mode. Left: muon-type candidates. Right: electron-type candidates, split into a low and high purity sample as well as the event counts in the peripheral sample, which occurred near the edge of the detector.

Two large-scale next-generation long-baseline experiments are currently under construction. DUNE [102] sends neutrinos from Fermilab to the Sanford Underground Research Facility in South Dakota, a 1,300 km-long baseline. The DUNE far detector will consist of four liquid argon time projection modules, each with at least a 10 kt fiducial mass. When operations start DUNE will use a 1.2 MW beam that can later be upgraded to 2.4 MW.

In Japan the Hyper-Kamiokande experiment [101] is being built to succeed Super-Kamiokande and T2K as the next-generation large water Cherenkov experiment. Its far detector will have a total water mass of 260 kt. Hyper-Kamiokande will use the T2K near detectors and receive a 1.3 MW beam from an upgraded J-PARC neutrino accelerator and beamline. Both DUNE and Hyper-Kamiokande will have rich physics programs including long-baseline neutrino oscillation studies, searches for nucleon decays, and observations of supernova neutrinos.

14.6.3.4 *Short-baseline experiments*

The LSND experiment searched for neutrino oscillation using neutrinos from stopped pions at Los Alamos. An 800 MeV linac was used to produce pions that stopped in the target. Most of the generated $\pi^-$s were absorbed by the nuclei within the target, while $\pi^+$s and daughter $\mu^+$s decay to produce neutrinos. Accordingly, $\nu_\mu$, $\bar{\nu}_\mu$, and $\nu_e$ dominate the resulting flux, with minimal contamination from $\bar{\nu}_e$. The LSND detector was a tank filled with 167 t of diluted liquid scintillator, located about 30 m from the neutrino source. LSND searched for $\bar{\nu}_\mu \to \bar{\nu}_e$ appearance using the inverse beta decay process, $\bar{\nu}_e + p \to e^+ + n$, and found an excess of $87.9 \pm 22.4 \pm 6.0$ events over the expected background [128]. Interpreting this excess as a two-flavor oscillation yields a mass squared splitting of O(1) eV$^2$.

The KARMEN experiment was performed at the ISIS neutron spallation facility at Rutherford Appleton Laboratory and also used neutrinos from stopped pions. Using the KARMEN 2 detector, a segmented liquid scintillation calorimeter with a total volume of 65 m$^3$ located at a mean distance of 17.7 m from the ISIS target, the experiment searched for $\bar{\nu}_\mu \to \bar{\nu}_e$ oscillations. No excess of signal was seen above the background expectation, which excluded a large region of the oscillation parameter space favored by LSND [129].

To further test the LSND result, the MiniBooNE experiment at Fermilab was performed with the same average L/E, but with a larger energy and longer baseline. It used the booster neutrino beam (BNB) beam produced by the 8 GeV protons of the Fermilab booster impinging on a beryllium target surrounded by single magnetic horn. Neutrino and antineutrino beams with peak energies of 600 and 400 MeV, respectively, were directed towards the MiniBoonNE detector, 12.2 m diameter sphere filled with 818 t of mineral oil located 541 m from the target. MiniBooNE reported excesses of both $\nu_e$ (neutrino beam) and $\bar{\nu}_e$ (antineutrino beam) events. The combined $\nu_e$ and $\bar{\nu}_e$ excess was $638.0 \pm 52.1 \pm 122.2$ over backgrounds, which corresponds to $4.8\sigma$ significance [130]. When interpreted as an oscillation signal, the MiniBooNE allowed region is consistent with both the LSND and KARMEN results in parts of the oscillation parameter space.

The short-baseline neutrino (SBN) program at Fermilab BNB [131] is designed to further investigate the reported excess. Whereas both LSND and MiniBooNE were single-detector experiments, the SBN program comprises three liquid argon time projection chambers at different baselines viewing the same neutrino beamline. The 85 t MicroBooNE detector was operated at 470 m from the target, the 112 t Short-Baseline Near Detector is operated at 110 m, and the 476 t ICARUS is located at 600 m downstream. The latter was transplanted to Fermilab after refurbishment at CERN and serves as the SBN far detector. As of this writing, MicroBooNE is the only experiment that has published results from SBN, observing no excess of $\nu_e$ events [132] and no evidence of light sterile neutrino oscillations [133]. ICARUS (SBND) has been taking data since 2022 (2024).

The JSNS$^2$ experiment at J-PARC has started a search for neutrino oscillations with $\Delta m^2 \sim 1$ eV$^2$ [134]. It observes neutrinos from muon decay at rest produced by the 1 MW proton beam from the 3 GeV J-PARC Rapid Cycling Synchrotron. With a 17 t fiducial mass detector filled with gadolinium-loaded liquid scintillator of located 24 m from the production target, JSNS$^2$ aims to provide a direct test of the LSND anomaly. The second phase of the experiment, which will add a second detector at 48 m, is now in preparation.

### 14.6.4 *Reactor Antineutrinos*

14.6.4.1 *Reactor antineutrino flux*

Nuclear reactors are intense sources of MeV-scale $\bar{\nu}_e$ which are generated in the nuclear fission of heavy isotopes, mainly $^{235}$U, $^{238}$U, $^{239}$Pu, and $^{241}$Pu. The $\bar{\nu}_e$ flux can be estimated based on the thermal power output and fuel composition of the reactor as a function of time. On average, about six $\bar{\nu}_e$ are emitted with about 200 MeV of energy per fission. Therefore, a 1 GW$_{\rm th}$ (thermal power)

reactor produces about $2 \times 10^{20}$ $\bar{\nu}_e$ per second.

Detailed estimates of the $\bar{\nu}_e$ flux and energy spectrum can be obtained by either summing up the spectra of the various decays from each fission fragment using available nuclear data, or by using measurements of the cumulative electron spectra associated with the beta decays of those fission fragments. Since the fission of the four main fuel isotopes involves thousands of beta-decay branches, a complete *ab initio* flux calculation is challenging. Cumulative electron spectra for $^{235}$U, $^{239}$Pu, and $^{241}$Pu were measured at the Institut Laue-Langevin (ILL) reactor in Grenoble, France in the 1980s [135–137]. Predictions of the $\bar{\nu}_e$ flux from $^{238}$U often use a summation calculation from [138] together with the ILL results.

A 2011 calculation of the reactor $\bar{\nu}_e$ flux [139] uses an improved *ab initio* approach for $^{238}$U as well as combined information from nuclear databases and electron spectra measured at ILL for $^{235}$U, $^{239}$Pu, and $^{241}$Pu. Another calculation [140] is provided for $^{235}$U, $^{239}$Pu, and $^{241}$Pu based on the ILL measurement of electron spectra, taking into account higher-order corrections and minimizing the use of nuclear databases. Both calculations predict a few percent higher normalization for the energy-averaged antineutrino fluxes of $^{235}$U, $^{239}$Pu, and $^{241}$Pu compared to the original analyses of ILL data. However, the reactor antineutrino flux measurement at Daya Bay [141–144] are consistent with a lower flux. Reactor flux calculations have recently been updated [145–147] and are now in better agreement with the Daya Bay data. Despite this improvement, a $\bar{\nu}_e$ excesses relative to predictions, both old and new, at around 5 MeV has been observed by recent reactor experiments [144, 148–150].

**Table 14.4:** List of reactor antineutrino oscillation experiments

| Name | Reactor power ($GW_{th}$) | Baseline (km) | Detector mass (t) | Year |
|---|---|---|---|---|
| KamLAND | various | 180 (ave.) | 1,000 | 2001– |
| Double Chooz | 4.25×2 | 1.05 | 8.3 | 2011–2018 |
| Daya Bay | 2.9×6 | 1.65 | 20×4 | 2011–2020 |
| RENO | 2.8×6 | 1.38 | 16 | 2011–2023 |
| JUNO | 26.6 (total) | 53 | 20,000 | 2025– |

14.6.4.2 *Reactor antineutrino oscillation experiments*

Charged current interactions are not possible at reactor neutrino energies if the produced $\bar{\nu}_e$ oscillate into $\bar{\nu}_\mu$ or $\bar{\nu}_\tau$. For this reason, $\bar{\nu}_e$ disappearance is the only channel available to study neutrino flavor change at reactor experiments. Inverse beta decay $\bar{\nu}_e + p \rightarrow e^+ + n$ provides a clean way to detect $\bar{\nu}_e$ in this energy region. A delayed-coincidence measurement of the prompt $e^+$ and delayed $\gamma$ rays emitted when the $n$ thermalizes and captures on a nucleus allows for efficient background suppression. Further, energy from the prompt $e^+$, $E_p$, can be used to form a simple, but robust estimator for the neutrino energy, $E_{\bar{\nu}} \sim E_p + 0.8$ MeV. Liquid scintillator is often used to realize large detectors since they have high light yield and offer many hydrogen nuclei that serve as both the inverse beta decay target and neutron capture nucleus. To increase the neutron detection efficiency, the scintillator may be loaded with gadolinium because of its large neutron capture cross-section. Additionally, gadolinium neutron captures liberate $\gamma$ rays whose total energy is about 8 MeV, making it easier to detect than the 2.2 MeV produced by capture on hydrogen.

Table 14.4 shows a list of reactor antineutrino experiments measuring neutrino oscillations. As was also shown in Table 14.1, experiments are designed with different baselines because of the different scale of mass splittings found by solar and atmospheric neutrino experiments. Experiments

with O(100) km baseline are sensitive to $\Delta m^2$ of $10^{-4}$–$10^{-5}$ eV$^2$, while $\sim 1$ km baseline results in a sensitivity in the range of $10^{-2}$–$10^{-3}$ eV$^2$.

The KamLAND detector consists of 1,000 t of ultra-pure liquid scintillator contained in a 13-m diameter spherical balloon [151]. It is located in the original Kamiokande cavern, where the $\bar{\nu}_e$ flux is dominated by a few reactors, whose average distance from the detector is ∼180 km. KamLAND reported first results in 2002 showing that the ratio of the observed number of $\bar{\nu}_e$ events and unoscillated expectations is $0.611 \pm 0.085 \pm 0.041$, which was evidence for reactor $\bar{\nu}_e$ disappearance at the 99.95% confidence level [151]. This result confirmed the large value of the mixing angle corresponding to the LMA solution reported by solar neutrino experiments. KamLAND also showed evidence of $\bar{\nu}_e$ spectrum distortion consistent with the expectation from neutrino oscillations [152]. Figure 14.7 shows KamLAND's ratio of the observed $\bar{\nu}_e$ spectrum to the expectation without oscillations as a function of $L_0/E$, $L_0 = 180$ km. A clear oscillatory signature can be seen.

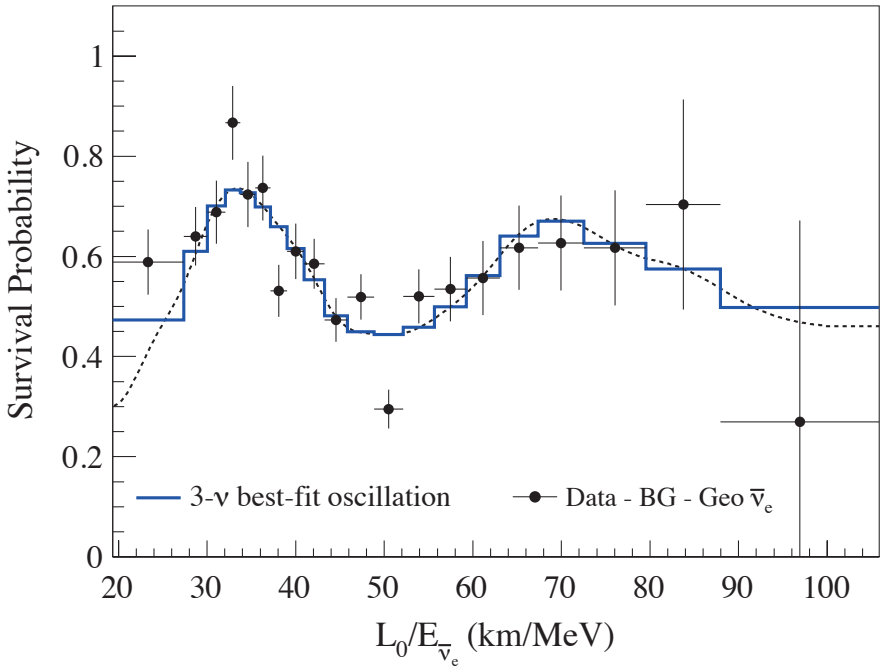


**Figure 14.7:** Ratio of the observed $\bar{\nu}_e$ spectrum to the expectation for no-oscillation versus $L_0/E$ for the KamLAND data. $L_0 = 180$ km is the flux-weighted average reactor baseline. The 3-$\nu$ histogram is the best-fit survival probability curve from the three-flavor unbinned maximum-likelihood analysis using only the KamLAND data. This figure is taken from [153].

Following the establishment of neutrino oscillations with atmospheric, solar, accelerator, and reactor experiments, measurement of the remaining mixing angle, $\theta_{13}$, was recognized as the next major milestone. A reactor neutrino experiment with a ∼1 km baseline can make an almost pure measurement of $\sin^2 2\theta_{13}$ from the disappearance of $\bar{\nu}_e$. In order to be sensitive to a small value of of this angle, experiments with multiple detectors, emulating the near- and far-detector strategy of accelerator experiments, were proposed. Three experiments were realized: Double Chooz in France, Daya Bay in China, and RENO in Korea.

These three experiments employ a similar detector design optimized for the precise measurement of reactor antineutrinos. Each detector consists of a cylindrical stainless steel vessel that houses two nested acrylic cylindrical vessels. A gadolinium-doped liquid scintillator in the innermost vessel

is used as the primary antineutrino target. It is surrounded by an undoped liquid scintillator layer that fills the larger acrylic vessel to contain $\gamma$ rays emitted from the target volume. Light from the liquid scintillator is detected by an array of PMTs mounted on the stainless steel vessel. Finally, mineral oil fills the region between the stainless steel vessel and acrylic volumes to shield them from radioactivity in the detector PMTs and surrounding rock. The region outside of the stainless steel vessel is instrumented as a veto detector filled with either liquid scintillator (Double Chooz) or with water (Daya Bay and RENO) detector.

The Double Chooz detector concept used a gadolinium-doped liquid scintillator with a mass of 8.3 t. Its far detector was located at a baseline of ∼1050 m from two 4.25 $GW_{th}$ reactors and started physics data taking in 2011. The near detector, located at ∼400 m from the reactors, was completed in the end of 2014. Double Chooz finished data taking in early 2018.

Daya Bay has two near detector sites with flux-weighted baselines of 470 m and 576 m, respectively, and one far site located underground and 1648 m from six reactors each with 2.9 $GW_{th}$. Daya Bay operated from 2011 until 2020 and used eight antineutrino detectors in total: two detectors in each of the near detector halls and four detectors in the far detector hall. Each detector contains 20 t of gadolinium-loaded liquid scintillator.

RENO has two identical detectors located at 294 m and 1383 m from the center of an array of six 2.8 $GW_{th}$ reactors. The mass of the gadolinium-loaded liquid scintillator is 16 t per detector. RENO took data with both near and far detectors from 2011 until 2023.

All three reactor neutrino experiments published their first results in 2012. Double Chooz reported results first, announcing an indication of reactor electron antineutrino disappearance with a ratio of observed to expected events of $R = 0.944 \pm 0.016 \pm 0.04$, which ruled out the no-oscillation hypothesis at 94.6% CL [154]. Shortly thereafter, Daya Bay observed $R = 0.940 \pm 0.011 \pm 0.004$, corresponding to $5.2\sigma$ significance of non-zero value of $\theta_{13}$ [155]. RENO also reported $R = 0.920 \pm 0.009 \pm 0.014$, indicating a non-zero value of $\theta_{13}$ with a significance of $4.9\sigma$ [156].

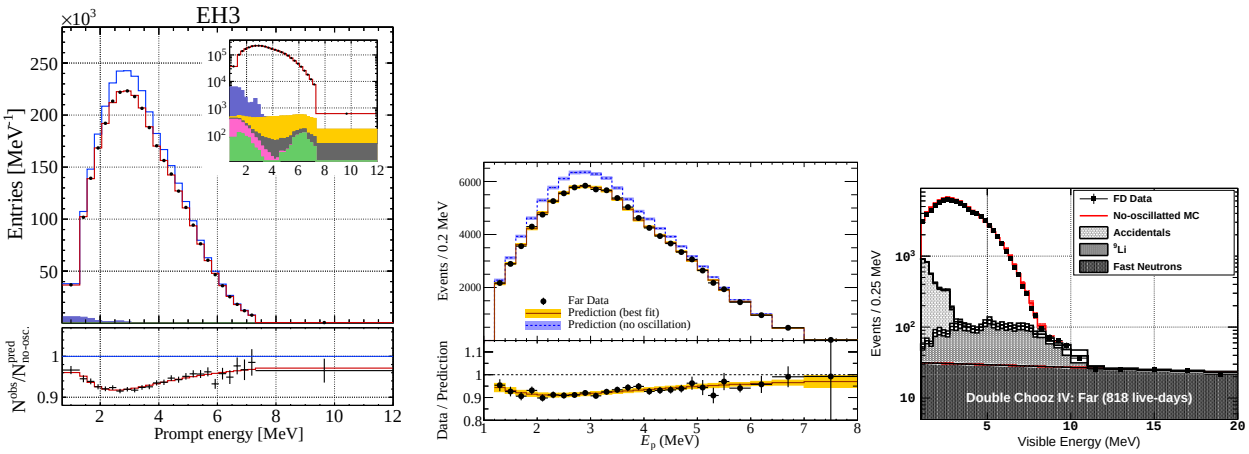


**Figure 14.8:** Energy spectra for prompt events at the far detectors for Daya Bay [157], RENO [148], and Double Chooz [149].

Both Daya Bay [157] and RENO [148, 158] report results constraining the mass-squared difference as well as the mixing angle using both relative near-far $\bar{\nu}_e$ rate and energy spectra information. Double Chooz has reported an analysis based on both far and near detectors [149] for the mixing angle, using neutron capture on any element (primarily gadolinium and hydrogen) to increase the effective target mass.

**Table 14.5:** List of reactor antineutrino experiments for O($eV^2$) oscillations

| Name | Reactor power ($MW_{th}$) | Baseline (m) | Detector mass (t) | Detector technology | $\sigma_E/E$ @1 MeV(%) | S/B |
|---|---|---|---|---|---|---|
| NEOS | 2,800 | 24 | 1 | Gd-LS | 5 | 22 |
| DANSS | 3,100 | 10–13 | 0.9 | Gd-PS | 34 | ∼30 |
| STEREO | 57 | 9–11 | 1.7 | Gd-LS | 10 | 0.9 |
| PROSPECT | 85 | 7–9 | 4 | $^6$Li-LS | 4.5 | 1.3 |
| NEUTRINO-4 | 100 | 6–12 | 1.5 | Gd-LS | 16 | 0.5 |
| SoLid | 80 | 6–9 | 1.6 | $^6$Li-PS | 14 | |

Figure 14.8 shows the energy spectra of the prompt signals observed in the far detectors of the three experiments. In all three experiments, an excess of $\bar{\nu}_e$ events over the expected energy spectrum has been observed around 5 MeV, as mentioned earlier. This excess is observed in both near and far detectors and scales with the reactor power. Due to cancellation between the near and far detectors, their neutrino oscillation measurements are not affected by this anomaly.

At a baseline of ∼50 km and with excellent energy measurement, reactor antineutrino experiments have significant sensitivity to the mass ordering by observing the precise distortion of the $\bar{\nu}_e$ spectrum over several oscillations in the detector. The JUNO experiment started taking data in August 2025 and is designed for this goal. It consists of a 20 kt liquid scintillator that is located 53 km from two nuclear power plants in China [159, 160]. In addition to the mass ordering, JUNO can make precision measurements of other oscillation parameters, including the solar parameters, and is large enough to host a broad program of non-oscillation physics.

14.6.4.3 *Reactor experiments sensitive to O(1) $eV^2$ oscillations*

Possible hints of neutrino oscillations at a scale of $\Delta m^2 \sim 1$ $eV^2$ (see Sec. 14.8) have motivated reactor experiments at a distance of ∼10 m from the core. Recent experiments searching for ∼1 $eV^2$ oscillation at reactors are summarized in Table 14.5. Some use commercial reactors as the antineutrino flux which can provide a large flux and therefore provide high statistical precision. Others use research reactors, which despite the orders-of-magnitude smaller flux, often have other advantages, such as easier access to short baselines, simpler fuel composition and smaller core sizes.

For these studies detectors typically use organic scintillators, either liquid scintillator (LS) or solid plastic scintillator (PS), which have hydrogen for the inverse beta decay target. To identify the signal delayed-coincidence with neutron capture on either gadolinium (Gd), as discussed above, or $^6$Li is used. Following neutron capture on $^6$Li, the excited nuclei decays into a triton and an $\alpha$. The effect of neutrino oscillation appears as a distortion of energy spectrum. In order to reduce reactor neutrino spectrum uncertainties, some experiments compare spectra at different baselines either by using a segmented detector or by moving the detector.

NEOS [150, 161] uses about 1 t of gadolinium-loaded liquid scintillator in an unsegmented detector. It is located at 23.7 m from the center of a commercial reactor and is covered by an overburden of about 20 meters of water equivalent. Using 180 days of data, NEOS and RENO have ruled out oscillations with $0.1 < |\Delta m^2| < 7 eV^2$ [161].

DANSS [162] is another experiment using a commercial reactor. The detector is highly segmented, consisting of 2,500 plastic scintillator strips, each with size $1 \times 4 \times 100$ $cm^3$ and coated with a thin gadolinium-loaded reflective layer. The detector is placed on a movable platform below the reactor core, which enables the distance to the core to vary from 10.7 to 12.7 m. DANSS did

not observe oscillations with a mass splitting of O(1) $eV^2$ [162].

The STEREO detector [163, 164] has six identical target cells each 37 cm in length, a $\sim 2m^3$ total volume, filled with gadolinium-loaded liquid scintillator. They are placed at distances ranging from 9.4 to 11.1 m from the compact (80 cm high, 40 cm diameter) core of the ILL research reactor. Using a data sample with more than 100,000 detected antineutrinos, STEREO has rejected neutrino mixing with $\Delta m^2$ between 0.1 and 10 $eV^2$ over a variety of mixing angles [164].

The PROSPECT detector [165] consists of a segmented 4 t $^6$Li-doped liquid scintillator detector. It covers a baseline range of 7–9 m from the highly enriched $^{235}$U reactor core of the High Flux Isotope Reactor (HFIR) at Oak Ridge National Laboratory. Thin reflecting panels divide the LS volume into an 11 × 14 two-dimensional array of 154 optically isolated rectangular segments ($14.5 \times 14.5 \times 117.6$ $cm^3$). PROSPECT found no significant indication of oscillations in the range $0.1 < |\Delta m^2| < 15$ $eV^2$ [165].

NEUTRINO-4 [166,167] uses a gadolinium-loaded liquid scintillator detector segmented in $10 \times 5$ sections with a total volume of 1.8 $m^3$. The detector is installed on a movable platform and can be moved to baselines spanning 6–12 m from the SM-3 reactor core in Russia. Using data collected between 2014 and 2021, NEUTRINO-4 observed an indication of oscillations consistent with $\Delta m^2 = 7.3 \pm 0.13(\text{stat.}) \pm 1.16(\text{syst.})$ and a mixing angle $\sin^2 2\theta = 0.36 \pm 0.12(\text{stat.})$ at $2.9\sigma$ significance.

The SoLid detector [168] is a finely segmented detector made of $5 \times 5 \times 5$ $cm^3$ plastic scintillator cubes and $^6$LiF:ZnS sheets. Using the difference of scintillation time constants between the ZnS and plastic scintillator, $n$-$\gamma$ separation is achieved. A detector with 1.6 t of active volume is installed at a distance of 6–9 m from the research reactor core at the BR2 reactor in Belgium.

## 14.7 Combined Analysis of Experimental Results: The $3\nu$ Paradigm

From the experimental situation described in Sec. 14.6 we conclude that

- Atmospheric $\nu_\mu$ and $\bar{\nu}_\mu$ disappear most likely converting to $\nu_\tau$ and $\bar{\nu}_\tau$. The results show an energy and distance dependence perfectly described by mass-induced oscillations.
- Accelerator $\nu_\mu$ and $\bar{\nu}_\mu$ disappear over distances of $\sim$ 200 to 800 km. The energy spectrum of the results show a clear oscillatory behavior also in accordance with mass-induced oscillations with a wavelength in agreement with the effect observed in atmospheric neutrinos.
- Accelerator $\nu_\mu$ and $\bar{\nu}_\mu$ appear as $\nu_e$ and $\bar{\nu}_e$ at distances $\sim$ 200 to 800 km.
- Solar $\nu_e$ convert to $\nu_\mu$ and/or $\nu_\tau$. The observed energy dependence of the effect is well described by massive neutrino conversion in the Sun matter according to the MSW effect
- Reactor $\bar{\nu}_e$ disappear over distances of $\sim$ 200 km and $\sim$ 1.5 km with different probabilities. The observed energy spectra show two different mass-induced oscillation wavelengths: at short distances in agreement with the one observed in accelerator $\nu_\mu$ disappearance, and a long distance compatible with the required parameters for MSW conversion in the Sun.

The minimum scenario to describe these results requires the mixing between the three flavour neutrinos of the standard model in three distinct mass eigenstates. In this case $U$ in Eq. (14.32) is a $3 \times 3$ matrix analogous to the CKM matrix for the quarks [21], but due to the possible Majorana nature of the neutrinos it can depend on six independent parameters: three mixing angles and three phases. There are several possible conventions for the ranges of the angles and ordering of the states. The community finally agreed to a parametrization of the leptonic mixing matrix as in Eq. (14.33). The angles $\theta_{ij}$ can be taken without loss of generality to lie in the first quadrant, $\theta_{ij} \in [0, \pi/2]$, and the phase $\delta_{\rm CP} \in [0, 2\pi]$. Values of $\delta_{\rm CP}$ different from 0 and $\pi$ imply $CP$ violation in neutrino oscillations in vacuum [169–171]. The Majorana phases $\eta_1$ and $\eta_2$ play no role in neutrino oscillations [170, 172]. Hence for the study of neutrino oscillations in the $3\nu$ mixing scenario one

can use the parametrization in Eq. (14.34) irrespective of whether neutrinos are Dirac or Majorana particles. Indeed, Majorana phases are very hard to measure since they are only physical if neutrino mass is non-zero, and therefore, the amplitude of any process involving them is suppressed by a factor $m_\nu/E$ to some power where $E$ is the energy involved in the process, which is typically much larger than the neutrino mass. The most sensitive experimental probe of Majorana phases is the rate of neutrinoless $\beta\beta$ decay discussed in Secs. 14.9.3 and 14.9.2.

In this convention there are two non-equivalent orderings for the spectrum of neutrino masses:

– Spectrum with Normal Ordering (NO) with $m_1 < m_2 < m_3$
– Spectrum Inverted ordering (IO) with $m_3 < m_1 < m_2$.

Furthermore, the data show a hierarchy between the mass splittings, $\Delta m^2_{21} \ll |\Delta m^2_{31}| \simeq |\Delta m^2_{32}|$ with $\Delta m^2_{ij} \equiv m^2_i - m^2_j$.

In this section, we follow the convention used in the listing section of the PDG and discuss the results for both, NO and IO, using $\Delta m^2_{21}$, which is always the smallest mass splitting, and $\Delta m^2_{32}$, which up to a sign, is the largest mass splitting for IO, while for NO the largest mass splitting is $\Delta m^2_{31} = \Delta m^2_{32} + \Delta m^2_{21}$.

With what we know of the mass differences (see table 14.7) and the neutrino mass scale (see Sec. 14.9), depending on the value of the lightest neutrino mass, the neutrino mass spectrum can be further classified in:

– Normal Hierarchical Spectrum (NH): $m_1 \ll m_2 < m_3$,
$\Rightarrow m_2 \simeq \sqrt{\Delta m^2_{21}} \sim 8.6 \times 10^{-3}\text{eV}, m_3 \simeq \sqrt{\Delta m^2_{32} + \Delta m^2_{21}} \sim 0.05\text{eV}$,

– Inverted Hierarchical Spectrum (IH): $m_3 \ll m_1 < m_2$,
$\Rightarrow m_1 \simeq \sqrt{|\Delta m^2_{32} + \Delta m^2_{21}|} \sim 0.0492\text{eV}, m_2 \simeq \sqrt{|\Delta m^2_{32}|} \sim 0.05\text{eV}$,

– Quasidegenerate Spectrum (QD): $m_1 \simeq m_2 \simeq m_3 \gg \sqrt{|\Delta m^2_{32}|}$.

Sometimes in the literature the determination of the neutrino mass spectrum is referred to as determination of the neutrino hierarchy. However, as described above, with what we know so far of the neutrino mass scale, the neutrino spectrum may or may not be hierarchical. Therefore determination of neutrino mass ordering is a more precise expression, and it is the one used in this review.

In total, the 3-$\nu$ oscillation analysis of the existing data involves six parameters: 2 mass differences (one of which can be positive or negative), 3 mixing angles, and the $CP$ phase. The different experiments described in Sec. 14.6 provide information on different subsets of these parameters. The precise statistical analysis of the data requires the numerical evaluation of the corresponding oscillation probabilities by solving the evolution equation of the neutrino ensemble from their source to the experiment. Nevertheless, the dominant effects in the different experiments can be qualitatively understood in terms of approximate expressions for the oscillation probabilities which, for convenience, we briefly summarize here.

### 14.7.1 *3$\nu$ Oscillation Probabilities*

The relevant survival probabilities for solar and KamLAND experiments in the framework of three neutrino oscillations can be written as:

$$P^{3\nu}_{ee} = \sin^4\theta_{13} + \cos^4\theta_{13} P^{2\nu}_{ee}(\Delta m^2_{21}, \theta_{12})\,, \tag{14.72}$$

where we have used the fact that $L^{\rm osc}_{0,32} = 4\pi E_\nu/\Delta m^2_{32}$ is much shorter than the distance traveled by both solar and KamLAND neutrinos, so that the oscillations related to $L^{\rm osc}_{0,32}$ are averaged. In the presence of matter effects $P^{2\nu}_{ee}(\Delta m^2_{21}, \theta_{12})$ should be calculated, taking into account the evolution in an effective matter density $n^{\rm eff}_e = n_e \cos^2\theta_{13}$. For $10^{-5} \lesssim \Delta m^2/{\rm eV}^2 \lesssim 10^{-4}$, $P^{2\nu}_{ee}(\Delta m^2_{21}, \theta_{12})$ presents the following asymptotic behaviors [173]:

$$P^{2\nu,{\rm sun}}_{ee} \simeq 1 - \frac{1}{2}\sin^2(2\theta_{12}) \qquad \text{for } E_\nu \lesssim \text{few} \times 100 \text{ keV}\,, \tag{14.73}$$

$$P^{2\nu,{\rm sun}}_{ee} \simeq \sin^2(\theta_{12}) \qquad \text{for } E_\nu \gtrsim \text{few} \times 1 \text{ MeV}\,, \tag{14.74}$$

$$P^{2\nu,{\rm kam}}_{ee} = 1 - \sin^2(2\theta_{12}) \sin^2 \frac{\Delta m^2_{21} L}{4E_\nu}. \tag{14.75}$$

At present most of the precision of the solar analysis is provided by SNO and SK, for which the relevant MSW survival probability provides a direct measurement of $\sin^2\theta_{12}$, as seen in Eq. (14.74). In the MSW regime, the determination of $\Delta m^2_{21}$ in solar experiments comes dominantly from the ratio between the solar potential and the $\Delta m^2_{21}$ term required to simultaneously describe the CC/NC data at SNO and the undistorted spectra of $^8$B neutrinos as measured in both SK and SNO. Conversely, KamLAND $\bar\nu_e$ survival probability proceeds dominantly as vacuum oscillations and provides a most precise determination of $\Delta m^2_{21}$ via the strong effect of the oscillating phase in the distortion of the reactor energy spectrum. On the contrary, it yields a weaker constraint on $\theta_{12}$ as the vacuum oscillation probability depends on the double-valued and "flatter" function $\sin^2(2\theta_{12})$.

In what respects the interpretation of $\nu_\mu$ disappearance data, at LBL experiments, the $\nu_\mu$ survival probability can be expanded in the small parameters $\sin\theta_{13}$ and $\alpha \equiv \Delta m^2_{21}/\Delta m^2_{31}$ to good accuracy as [174, 175]

$$P_{\nu_\mu\to\nu_\mu} \approx 1 - \sin^2 2\theta_{\mu\mu} \sin^2 \frac{\Delta m^2_{\mu\mu} L}{4E_\nu} \approx 1 - \cos^2\theta_{13} \sin^2(2\theta_{23}) \sin^2 \frac{\Delta m^2_{32} L}{4E_\nu} + \mathcal{O}(\alpha, s^2_{13})\,, \tag{14.76}$$

with

$$\begin{aligned} \sin^2\theta_{\mu\mu} &= \cos^2\theta_{13}\sin^2\theta_{23}\,, \\ \Delta m^2_{\mu\mu} &= \sin^2\theta_{12}\Delta m^2_{31} + \cos^2\theta_{12}\Delta m^2_{32} \\ &\quad + \cos\delta_{\rm CP}\sin\theta_{13}\sin 2\theta_{12}\tan\theta_{23}\Delta m^2_{21}. \end{aligned}$$

At present $\nu_\mu$ disappearance results at LBL provide the best determination of $|\Delta m^2_{32}|$ and $\theta_{23}$, but as seen above, the probability is symmetric with respect to the octant of $\theta_{\mu\mu}$, which implies symmetry around $s^2_{23} = 0.5/c^2_{13}$.

The relevant oscillation probability for $\nu_e$ appearance at LBL experiments can be expanded at the second order in the small parameters $\sin\theta_{13}$ and $\alpha$, and assuming a constant matter density it takes the form [176–178]:

$$\begin{aligned} P_{\nu_\mu\to\nu_e,(\bar\nu_\mu\to\bar\nu_e)} \approx 4\,\sin^2\theta_{13}\,\sin^2\theta_{23} \frac{\sin^2\Delta(1-A)}{(1-A)^2} + \alpha^2 \sin^2 2\theta_{12}\,\cos^2\theta_{23} \frac{\sin^2 A\Delta}{A^2} \\ + 8\,\alpha\, J^{\rm max}_{\rm CP} \cos(\Delta \pm \delta_{\rm CP}) \frac{\sin A\Delta}{A} \frac{\sin\Delta(1-A)}{1-A}\,, \end{aligned} \tag{14.77}$$

with

$$J^{\rm max}_{\rm CP} = \cos\theta_{12}\sin\theta_{12}\cos\theta_{23}\sin\theta_{23}\cos^2\theta_{13}\sin\theta_{13}\,, \tag{14.78}$$

and

$$\Delta \equiv \frac{\Delta m^2_{31} L}{4E_\nu}\,, \quad A \equiv \frac{2E_\nu V}{\Delta m^2_{31}}\,, \tag{14.79}$$

where $V$ is the effective matter potential in the Earth's crust. Results on $\nu_e$ appearance at LBL provide us with the dominant information on leptonic $CP$ violation. Furthermore, $\alpha$, $\Delta$, and $A$ are sensitive to the sign of $\Delta m^2_{32}$ (*i.e.*, the type of the neutrino mass ordering). The plus (minus) sign in Eq. (14.77) applies for neutrinos (antineutrinos), and for antineutrinos $V \to -V$, which implies $A \to -A$. Numerically one finds for a typical Earth crust matter density of 3 g/cm$^3$ that at T2K with $E \sim 0.7$ GeV, matter effects cause $\sim \pm 10\%$ differences in the rates, whereas in NOvA with $E \sim 2$ GeV, we can have $|A| \sim 0.2$. Also, $\alpha^2 \approx 10^{-3}$, which implies that the second term in the first line of Eq. (14.77) gives a very small contribution compared to the other terms. Also, the first term in Eq. (14.77) (which dominates for large $\theta_{13}$) depends on $\sin^2\theta_{23}$ and therefore is sensitive to the octant.

The $\nu_e$ survival probability relevant for reactor experiments with medium baseline (MBL), $L \sim 1$ km, can be approximated as [175, 179]:

$$P_{\nu_e \to \nu_e} = 1 - \sin^2 2\theta_{13} \sin^2 \frac{\Delta m^2_{ee} L}{4E_\nu} + \mathcal{O}(\alpha^2)\,, \tag{14.80}$$

where

$$\Delta m^2_{ee} = \cos^2\theta_{12}\Delta m^2_{31} + \sin^2\theta_{12}\Delta m^2_{32}\,. \tag{14.81}$$

These MBL reactor experiments provide the most precise determination of $\theta_{13}$. Furthermore there is an additional effect sensitive to the mass ordering when comparing the disappearance of $\nu_\mu$ at LBL experiments – which is symmetric with respect to the sign of $\Delta m^2_{\mu\mu}$ given in Eq. (14.7.1) – with that of $\nu_e$ disappearance at MBL reactors which is symmetric with respect to the slightly different effective mass-squared difference $\Delta m^2_{ee}$ given in Eq. (14.81).

**Table 14.6:** Experiments contributing to the present determination of the oscillation parameters.

| Experiment | Dominant | Important |
|---|---|---|
| Solar Experiments | $\theta_{12}$ | $\Delta m^2_{21}$, $\theta_{13}$ |
| Reactor LBL (KamLAND) | $\Delta m^2_{21}$ | $\theta_{12}$, $\theta_{13}$ |
| Reactor MBL (Daya-Bay, Reno, D-Chooz) | $\theta_{13}$, $\lvert\Delta m^2_{31,32}\rvert$ | |
| Atmospheric Experiments (IC-DC,SK) | $\theta_{23}$, $\lvert\Delta m^2_{31,32}\rvert$, sign($\Delta m^2_{31,32}$) | $\theta_{13}$, $\delta_{\rm CP}$ |
| Accel LBL $\nu_\mu$,$\bar\nu_\mu$, Disapp (T2K, NO$\nu$A, MINOS, K2K) | $\lvert\Delta m^2_{31,32}\rvert$, $\theta_{23}$ | |
| Accel LBL $\nu_e$,$\bar\nu_e$ App (T2K, NO$\nu$A, MINOS) | $\delta_{\rm CP}$, $\theta_{23}$, sign($\Delta m^2_{31,32}$) | $\theta_{13}$ |

Finally, for atmospheric neutrinos, the fluxes contain $\nu_e$, $\nu_\mu$, $\bar\nu_e$, and $\bar\nu_\mu$, and for a good fraction of the events, neutrinos travel through the Earth's matter. In the context of $3\nu$ mixing, the dominant oscillation channel of atmospheric neutrinos is $\nu_\mu \to \nu_\tau$ driven by $|\Delta m^2_{32}|$ with an amplitude controlled by $\theta_{23}$ with subleading oscillation modes, triggered by $\Delta m^2_{21}$ and/or $\theta_{13}$, which depend on the octant of $\theta_{23}$, on the mass ordering, and on $\delta_{\rm CP}$. In that respect, an interesting observable is the deviation of $e$-like events relative to the no-oscillation prediction $N^0_e$, since in the two-flavour limit one expects $N_e = N^0_e$ . Such deviation can be written in the following way (see, *e.g.*, [180]):

$$\begin{aligned}\frac{N_e}{N^0_e} - 1 \approx\ & (r\sin^2\theta_{23} - 1)P_{2\nu}(\Delta m^2_{32}, \theta_{13}) + (r\cos^2\theta_{23} - 1)P_{2\nu}(\Delta m^2_{21}, \theta_{12}) \\ & - \sin\theta_{13}\sin 2\theta_{23}\, r\, \Re(A^*_{ee}A_{\mu e})\,.\end{aligned} \tag{14.82}$$

Here $r \equiv \Phi_\mu/\Phi_e$ is the flux ratio with $r \approx 2$ in the sub-GeV range and $r \approx 2.6 \to 4.5$ in the multi-GeV range. $P_{2\nu}(\Delta m^2, \theta)$ is an effective two-flavour oscillation probability, and $A_{ee}$, $A_{\mu e}$ are elements

of a transition amplitude matrix. The three terms appearing in Eq. (14.82) have a well-defined physical interpretation. The first term is important in the multi-GeV range and is controlled by the mixing angle $\theta_{13}$ in $P_{2\nu}(\Delta m^2_{32}, \theta_{13})$. This probability can be strongly affected by resonant matter effects [181–186]. Depending on the mass ordering, the resonance will occur either for neutrinos or antineutrinos. The second term is important for sub-GeV events, and it takes into account the effect of oscillations due to $\Delta m^2_{21}$ and $\theta_{12}$ [187–190]. Via the pre-factor containing the flux ratio $r$, both the first and second terms in Eq. (14.82) depend on the octant of $\theta_{23}$, though in opposite directions: the multi-GeV (sub-GeV) excess is suppressed (enhanced) for $\theta_{23} < 45°$. Finally, the last term in Eq. (14.82) is an interference term between $\theta_{13}$ and $\Delta m^2_{21}$ amplitudes and this term shows also dependence on the $CP$ phase $\delta_{\rm CP}$ [180, 190].

Subdominant three neutrino effects can also affect $\mu$-like events. For example, for multi-GeV muon events one can write the excess in $\mu$-like events as [191, 192]

$$\frac{N_\mu}{N^0_\mu} - 1 \approx \sin^2\theta_{23}\left(\frac{1}{r} - \sin^2\theta_{23}\right) P_{2\nu}(\Delta m^2_{32}, \theta_{13}) - \frac{1}{2}\sin^2 2\theta_{23}\left[1 - \Re(A_{33})\right] . \tag{14.83}$$

The first term is controlled by $\theta_{13}$ and is subject to resonant matter effects, similar to the first term in Eq. (14.82), though with a different dependence on $\theta_{23}$ and the flux ratio. In the second term, $A_{33}$ is a probability amplitude satisfying $P_{2\nu}(\Delta m^2_{32}, \theta_{13}) = 1 - |A_{33}|^2$. In the limit $\theta_{13} = 0$ we have $\Re(A_{33}) = \cos(\Delta m^2_{32} L/2E)$, such that the second term in Eq. (14.83) just describes two-flavour $\nu_\mu \to \nu_\mu$ vacuum oscillations.

### 14.7.2 *3ν Oscillation Analysis*

We summarize in Table 14.6 the different experiments which dominantly contribute to the present determination of the different parameters in the chosen convention.

The table illustrates that the determination of the leptonic parameters requires global analyses of the data from the different experiments. Over the years, these analyses have been in the hands of a few phenomenological groups. We show in Table 14.7 the results from the latest analyses in Refs. [193–196]. For the sake of comparison, all results are presented in the convention of the listing section as described above.

The table displays the dependence of the present determination of the parameters on variations of the statistical analysis performed by the different groups and on the data samples included. In that last respect, the main difference resides in the latest results from Super-Kamiokande [197, 199] and IceCube/DeepCore [198, 200] atmospheric data which, at present, can only be included in these analysis by directly adding the tabulated $\chi^2$ map provided by the experiments [197, 198].

Altogether the different analyses find consistent results, in particular on the better-known parameters, $\theta_{12}$, $\theta_{13}$ and $\Delta m^2_{21}$ and $|\Delta m^2_{32}|$. The issues which still require clarification are the mass ordering discrimination, the determination of $\theta_{23}$ and the leptonic $CP$ phase $\delta_{\rm CP}$:

- The analysis without including the atmospheric $\chi^2$ tables from Refs. [197, 198] show no statistically significant preference for any ordering. Including them, the best fit is for the normal mass ordering with inverted ordering disfavoured with a $\Delta\chi^2$ slightly above $2\sigma$. The result emerges from opposite trends in the long-baseline accelerator appearance data from T2K and NOvA on the one hand, and in the combination of the disappearance channels from accelerator and reactor experiments on the other hand. In the former case, at the time of this review, the tension between T2K and NOvA for NO has reached $\sim 2\sigma$ with the latest NOvA update, whereas they are perfectly consistent for IO. There are ongoing efforts for a joint T2K+NOvA analysis by the collaborations (their preliminary joint analysis [201] performed with previous data samples fully agrees with the results from the analysis of the phenomenological groups).

**Table 14.7:** $3\nu$ oscillation parameters obtained from different global analyses of neutrino data. In all cases, the numbers labeled as NO (IO) are obtained assuming NO (IO), *i.e.*, relative to the respective local minimum. SK-ATM and IC24 makes reference to the tabulated $\chi^2$ maps from Super-Kamiokande [197] and IceCube/DeepCore [198] atmospheric data.

| | Ref. [193] w/o SK-ATM & IC24 | | Ref. [193] w SK-ATM & IC24 | | Ref. [194] w SK-ATM & IC24 | | Ref. [195] w SK-ATM* | |
|---|---|---|---|---|---|---|---|---|
| NO | $\Delta\chi^2 = 0.6$ | | Best Fit Ordering | | Best Fit Ordering | | Best Fit Ordering | |
| Param | bfp $\pm1\sigma$ | $3\sigma$ range | bfp $\pm1\sigma$ | $3\sigma$ range | bfp $\pm1\sigma$ | $3\sigma$ range | bfp $\pm1\sigma$ | $3\sigma$ range |
| $\frac{\sin^2\theta_{12}}{10^{-1}}$ | $3.07^{+0.12}_{-0.11}$ | $2.75 \to 3.45$ | $3.08^{+0.12}_{-0.11}$ | $2.75 \to 3.45$ | $3.03^{+0.14}_{-0.12}$ | $2.64 \to 3.45$ | $3.04^{+0.16}_{-0.16}$ | $2.57 \to 3.55$ |
| $\theta_{12}/^\circ$ | $33.68^{+0.73}_{-0.70}$ | $31.63 \to 35.95$ | $33.68^{+0.73}_{-0.70}$ | $31.63 \to 35.95$ | $33.40^{+0.87}_{-0.75}$ | $30.92 \to 35.97$ | $33.46^{+0.99}_{-1.1}$ | $30.46 \to 36.57$ |
| $\frac{\sin^2\theta_{23}}{10^{-1}}$ | $5.61^{+0.12}_{-0.15}$ | $4.30 \to 5.96$ | $4.70^{+0.17}_{-0.13}$ | $4.35 \to 5.85$ | $4.73^{+0.23}_{-0.13}$ | $4.37 \to 5.81$ | $5.60^{+0.13}_{-0.22}$ | $4.32 \to 5.96$ |
| $\theta_{23}/^\circ$ | $48.5^{+0.7}_{-0.9}$ | $41.0 \to 50.4$ | $43.3^{+1.0}_{-0.9}$ | $41.3 \to 49.9$ | $43.4^{+1.3}_{-0.8}$ | $41.4 \to 49.7$ | $48.4^{+0.7}_{-1.2}$ | $41.2 \to 50.5$ |
| $\frac{\sin^2\theta_{13}}{10^{-2}}$ | $2.195^{+0.054}_{-0.058}$ | $2.023 \to 2.376$ | $2.215^{+0.056}_{-0.058}$ | $2.030 \to 2.388$ | $2.23^{+0.04}_{-0.06}$ | $2.06 \to 2.38$ | $2.20^{+0.07}_{-0.04}$ | $2.05 \to 2.38$ |
| $\theta_{13}/^\circ$ | $8.52^{+0.11}_{-0.11}$ | $8.18 \to 8.87$ | $8.56^{+0.11}_{-0.11}$ | $8.19 \to 8.89$ | $8.59^{+0.08}_{-0.12}$ | $8.25 \to 8.87$ | $8.53^{+0.14}_{-0.08}$ | $8.23 \to 8.87$ |
| $\delta_{\rm CP}/^\circ$ | $177^{+19}_{-20}$ | $96 \to 422$ | $212^{+26}_{-41}$ | $124 \to 364$ | $216^{+31}_{-23}$ | $131 \to 365$ | $202^{+29}_{-22}$ | $137 \to 360$ |
| $\frac{\Delta m^2_{21}}{10^{-5}\ \text{eV}^2}$ | $7.49^{+0.19}_{-0.20}$ | $6.92 \to 8.05$ | $7.49^{+0.19}_{-0.20}$ | $6.92 \to 8.05$ | $7.37^{+0.15}_{-0.16}$ | $6.93 \to 7.93$ | $7.55^{+0.22}_{-0.20}$ | $6.98 \to 8.19$ |
| $\frac{\Delta m^2_{32}}{10^{-3}\ \text{eV}^2}$ | $2.459^{+0.025}_{-0.023}$ | $2.388 \to 2.531$ | $2.438^{+0.021}_{-0.019}$ | $2.376 \to 2.503$ | $2.458^{+0.020}_{-0.020}$ | $2.396 \to 2.521$ | $2.42^{+0.02}_{-0.02}$ | $2.35 \to 2.49$ |
| IO | Best Fit Ordering | | $\Delta\chi^2 = 6.1$ | | $\Delta\chi^2 = 5.0$ | | $\Delta\chi^2 = 7.7$ | |
| $\frac{\sin^2\theta_{12}}{10^{-1}}$ | $3.08^{+0.12}_{-0.11}$ | $2.75 \to 3.45$ | $3.08^{+0.12}_{-0.11}$ | $2.75 \to 3.45$ | $3.03^{+0.14}_{-0.12}$ | $2.64 \to 3.45$ | $3.04^{+0.16}_{-0.16}$ | $2.57 \to 3.55$ |
| $\theta_{12}/^\circ$ | $33.68^{+0.73}_{-0.70}$ | $31.63 \to 35.95$ | $33.68^{+0.73}_{-0.70}$ | $31.63 \to 35.95$ | $33.40^{+0.87}_{-0.75}$ | $30.92 \to 35.97$ | $33.46^{+0.99}_{-1.1}$ | $30.46 \to 36.57$ |
| $\frac{\sin^2\theta_{23}}{10^{-1}}$ | $5.62^{+0.12}_{-0.15}$ | $4.37 \to 5.97$ | $5.50^{+0.12}_{-0.15}$ | $4.40 \to 5.84$ | $5.45^{+0.15}_{-0.17}$ | $4.43 \to 5.83$ | $5.57^{+0.14}_{-0.20}$ | $4.34 \to 5.93$ |
| $\theta_{23}/^\circ$ | $48.6^{+0.7}_{-0.9}$ | $41.4 \to 50.6$ | $47.9^{+0.7}_{-0.9}$ | $41.5 \to 49.8$ | $47.6^{+0.9}_{-1.0}$ | $41.7 \to 50.0$ | $48.3^{+0.8}_{-1.1}$ | $41.2 \to 50.3$ |
| $\frac{\sin^2\theta_{13}}{10^{-2}}$ | $2.224^{+0.056}_{-0.057}$ | $2.053 \to 2.397$ | $2.221^{+0.056}_{-0.056}$ | $2.060 \to 2.409$ | $2.23^{+0.07}_{-0.04}$ | $2.08 \to 2.41$ | $2.23^{+0.05}_{-0.06}$ | $2.06 \to 2.39$ |
| $\theta_{13}/^\circ$ | $8.58^{+0.11}_{-0.11}$ | $8.24 \to 8.91$ | $8.59^{+0.11}_{-0.11}$ | $8.25 \to 8.93$ | $8.59^{+0.13}_{-0.08}$ | $8.29 \to 8.93$ | $8.58^{+0.10}_{-0.12}$ | $8.25 \to 8.89$ |
| $\delta_{\rm CP}/^\circ$ | $285^{+25}_{-28}$ | $201 \to 348$ | $274^{+22}_{-25}$ | $201 \to 335$ | $274^{+25}_{-27}$ | $193 \to 329$ | $270^{+23}_{-25}$ | $200 \to 355$ |
| $\frac{\Delta m^2_{21}}{10^{-5}\ \text{eV}^2}$ | $7.49^{+0.19}_{-0.19}$ | $6.92 \to 8.05$ | $7.49^{+0.19}_{-0.19}$ | $6.92 \to 8.05$ | $7.37^{+0.15}_{-0.16}$ | $6.93 \to 7.93$ | $7.55^{+0.22}_{-0.20}$ | $6.98 \to 8.19$ |
| $\frac{\Delta m^2_{32}}{10^{-3}\ \text{eV}^2}$ | $-2.510^{+0.024}_{-0.025}$ | $-2.584 \to -2.438$ | $-2.484^{+0.020}_{-0.020}$ | $-2.547 \to -2.421$ | $-2.502^{+0.021}_{-0.020}$ | $-2.564 \to -2.440$ | $-2.48\pm^{+0.02}_{-0.02}$ | $-2.53 \to -2.40$ |

*This analysis does not include the latest results of T2K and NOvA presented in the Intern. Conference Neutrino 2024.

Conversely, the determination of $|\Delta m^2_{3\ell}|$ from $\nu_\mu$ and $\nu_e$ disappearance agrees better for NO than for IO.

- There is no statistically significant preference for the octact of $\theta_{23}$ in any of the analysis.
- The determination of the leptonic CP phase strongly depends on the mass ordering. For normal ordering the best-fit point is very close to the CP-conserving value of 180° (with $\Delta\chi^2 < 1$) while for inverted ordering, the best fit points for both data variants are close to maximal CP violation $\delta_{\rm CP} = 270°$ (within $1\sigma$).

### 14.7.3 *Convention-independent Measures of Leptonic CP Violation in 3ν Mixing*

In the framework of $3\nu$ mixing leptonic $CP$ violation can also be quantified in terms of the leptonic Jarlskog invariant [202], defined by:

$$\Im[U_{\alpha i}U^*_{\alpha j}U^*_{\beta i}U_{\beta j}] \equiv \sum_{\gamma=e,\mu,\tau}\sum_{k=1,2,3} J_{\rm CP}\,\epsilon_{\alpha\beta\gamma}\,\epsilon_{ijk} \equiv J^{\rm max}_{\rm CP}\,\sin\delta_{\rm CP}\,. \tag{14.84}$$

With the convention in Eq. (14.33) $J^{\rm max}_{\rm CP}$ is the combination of mixing angles in Eq. (14.78). For example, from the analysis in Ref. [193]

$$J^{\rm max}_{\rm CP} = 0.0333 \pm 0.0007\,(\pm 0.0017)\,, \tag{14.85}$$

at $1\sigma$ ($3\sigma$) for both orderings, while the the dependence of the prefered value of $\delta_{\rm CP}$ on the octant implies a a value $J_{\rm CP}^{\rm best} = 0.0015$ (-0.032) in normal (inverted) ordering.

The status of the determination of leptonic $CP$ violation can also be graphically displayed by projecting the results of the global analysis in terms of leptonic unitarity triangles [203–205]. Since in the analysis $U$ is unitary by construction, any given pair of rows or columns can be used to define a triangle in the complex plane. There are a total of six possible triangles corresponding to the unitary conditions

$$\sum_{i=1,2,3} U_{\alpha i} U^*_{\beta i} = 0 \text{ with } \alpha \neq \beta\,, \qquad \sum_{\alpha=e,\mu,\tau} U_{\alpha i} U^*_{\alpha j} = 0 \text{ with } i \neq j\,. \tag{14.86}$$

As an illustration we show in Fig. 14.9 the recasting of the allowed regions of the analysis in Ref. [193] in terms of one leptonic unitarity triangle. We show the triangle corresponding to the unitarity conditions on the first and third columns (after the shown rescaling), which is the equivalent to the one usually shown for the quark sector. In this figure, the absence of $CP$ violation would imply a flat triangle, *i.e.*, $\Im(z) = 0$. So the CL at which leptonic $CP$ violation is being observed would be given by the CL at which the region crosses the horizontal axis. Notice however, that this representation is made *under the assumption of a unitary $U$ matrix* and therefore does not provide any test of unitarity in the leptonic sector.

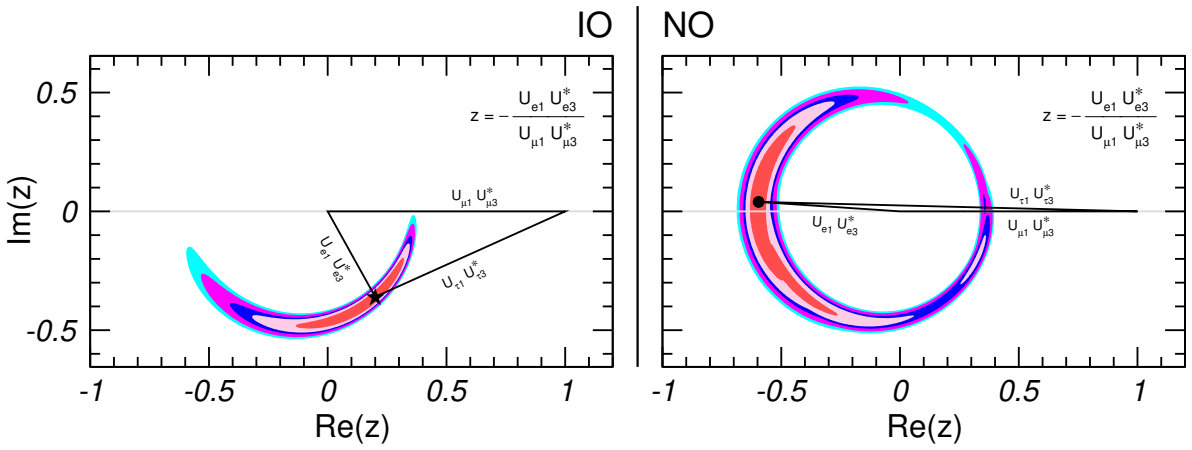


**Figure 14.9:** Leptonic unitarity triangle for the first and third columns of the mixing matrix. After scaling and rotating the triangle so that two of its vertices always coincide with $(0, 0)$ and $(1, 0)$ the figure shows the $1\sigma$, 90%, $2\sigma$, 99%, $3\sigma$ CL (2 dof) allowed regions of the third vertex for the IO (left) and NO (right) from the analysis in Ref. [193].

## 14.8 Beyond $3\nu$: Additional Neutrinos at the eV Scale

As mentioned in Sec. 14.1, whatever the extension of the SM we want to consider, it must contain only three light active neutrinos. Therefore if we need more than three light massive neutrinos, we must add sterile neutrinos to the particle content of the model.

Historically, models with extended light neutrino sectors were invoked to explain a set of anomalies observed at short baselines and which could not be explained within the $3\nu$ framework but could be interpreted as hints for the existence of additional neutrino states with masses at the eV scale. These anomalies have been under study by the experimental community with a set of follow-up measurements performed at SBL both at reactors and accelerators (see the corresponding subsections in Sec. 14.6.4 and Sec. 14.6.3). In brief:

- the LSND experiment [128] reported evidence for $\bar{\nu}_\mu \to \bar{\nu}_e$ transitions with $E/L \sim 1$ eV$^2$, where $E$ and $L$ are the neutrino energy and the distance between source and detector, respectively (see *Short Baseline Experiments* subsection of Sec.14.6.3).
- this effect was further explored by the MiniBooNE experiment [206], which reported a yet unexplained event excess in the low-energy region of the electron neutrino and antineutrino event spectra. No significant excess is found at higher neutrino energies. Interpreting the data in terms of oscillations, parameter values consistent with the ones from LSND were obtained. The MicroBooNE experiment [207] was designed to identify the nature of the low-energy MiniBooNE excess and was able to exclude that it was composed enterely of $\nu_e$ at 99%CL [208] and rule out part of the sterile neutrino oscillation parameter space [133].
- the calculations of the neutrino flux emitted by nuclear reactors in Refs. [139, 140] predicted a neutrino rate that was a few percent higher than observed in short-baseline ($L \lesssim 100$ m) reactor experiments at the time. This "reactor anomaly" could be explained by assuming $\bar{\nu}_e$ disappearance due to averaged oscillations with $\Delta m^2 \sim 1$ eV$^2$ [209]. Over the years the flux predictions from [139, 140] have not been supported by the reactor antineutrino flux measurement at Daya Bay [141, 142] pointing to a lower flux from $^{235}$U, in particular. In addition, several reactor experiments NEOS, STEREO, PROSPECT, DANSS, SOLID and Neutrino4 have searched, and, all except the last one, have excluded a L/E variation compatible with $\Delta m^2 \sim 1$ eV$^2$ oscillations. In the last years the reactor flux calculations have been revisited [145–147] and in most cases lower fluxes are predicted, in agreement with the flux measurement at Daya Bay [144]. These new fluxes, correspondingly eliminate the significance of the anomaly [210].
- radioactive source experiments at the Gallium solar neutrino experiments both in SAGE and GALLEX/GNO obtained an event rate lower than expected. This result was confirmed by the BEST experiment [211]. If not due to uncertainties in the interaction cross-section, this effect by itself can be explained by the hypothesis of $\nu_e$ disappearance due to oscillations with $\Delta m^2 \gtrsim 1$ eV$^2$ ("Gallium anomaly") [212–214]. This intepretation, however is in tension with the analysis of solar neutrino experiments [215], and most recently has been excluded with high significance by KATRIN [216] (see left panel in Fig. 14.10, taken from Ref. [217]).

As mentioned above, historically, these anomalies opened the question of whether they could all be consistently described in combination with the rest of the neutrino data – in particular with the negative results on the disappearance of $\nu_\mu$ at short distances – by extending the neutrino mass and mixing framework to account for some additional sterile states.

Quantitatively one can start by adding a fourth massive neutrino state to the spectrum and perform a global data analysis to answer this question. In this case there are six possible four-neutrino schemes that can, in principle, accommodate the results of solar+KamLAND and atmospheric+LBL neutrino experiments as well as the SBL result. They can be divided into two classes: (2+2) and (3+1). In (2+2) schemes, there are two pairs of close masses (one pair responsible for solar results and the other for atmospheric [218]) separated by the $\mathcal{O}(\text{ eV})$ gap. In this case the transition into the sterile neutrino is a solution of either the solar or the atmospheric neutrino problem, or the sterile neutrino takes part in both. Consequently, a (2+2)-spectrum is easier to test because the required mixing of sterile neutrinos in either solar and/or atmospheric oscillations would modify their effective matter potential in the Sun and in the Earth, giving distinctive effects in the solar and/or atmospheric neutrino observables. Those distinctive effects were not observed so oscillations into sterile neutrinos did not describe well either solar or atmospheric data. Consequently, as soon as the early 2000's 2+2 spectra could be ruled out already beyond 3-4 $\sigma$.

On the contrary, for a (3+1)-spectrum (and more generally for a $3 + N$-spectrum with an

arbitrary $N$ number of sterile states), the sterile neutrino(s) could be only slightly mixed with the active ones and mainly provide a description of the SBL results. In this case, the oscillation probabilities for experiments working at $E/L \sim 1$ eV$^2$ take a simple form:

$$P_{\alpha\alpha} = 1 - \sin^2 2\theta_{\alpha\alpha} \sin^2 \Delta\,, \qquad P_{\mu e} = \sin^2 2\theta_{\mu e} \sin^2 \Delta\,, \tag{14.87}$$

where $\Delta \equiv \Delta m^2_{41} L/4E$ and one can define effective mixing angles

$$\sin^2 2\theta_{\alpha\alpha} \equiv 4|U_{\alpha 4}|^2(1 - |U_{\alpha 4}|^2)\,, \qquad \sin^2 2\theta_{\mu e} \equiv 4|U_{\mu 4}|^2|U_{e4}|^2\,. \tag{14.88}$$

In here $\alpha = e, \mu$ and $U_{\alpha 4}$ are the elements of the lepton mixing matrix describing the mixing of the 4th neutrino mass state with the electron and muon flavour. In this scenario, there is no sensitivity to $CP$ violation in the the $\Delta$ driven oscillations, so the relations above are valid for both neutrinos and antineutrinos. At linear order in the mixing elements one can derive a relation between the amplitudes of appearance and disappearance probabilities:

$$4 \sin^2 2\theta_{\mu e} \approx \sin^2 2\theta_{ee} \sin^2 2\theta_{\mu\mu}\,. \tag{14.89}$$

This relation implies a constraint between the possible results in disappearance and appearance experiments which jeopardizes a consistent description of all of the SBL anomalies. Over the years, different groups have performed a variety of such global analyses leading to different quantitative conclusions on the statistical quality of the global fit (see for example [219–224]).

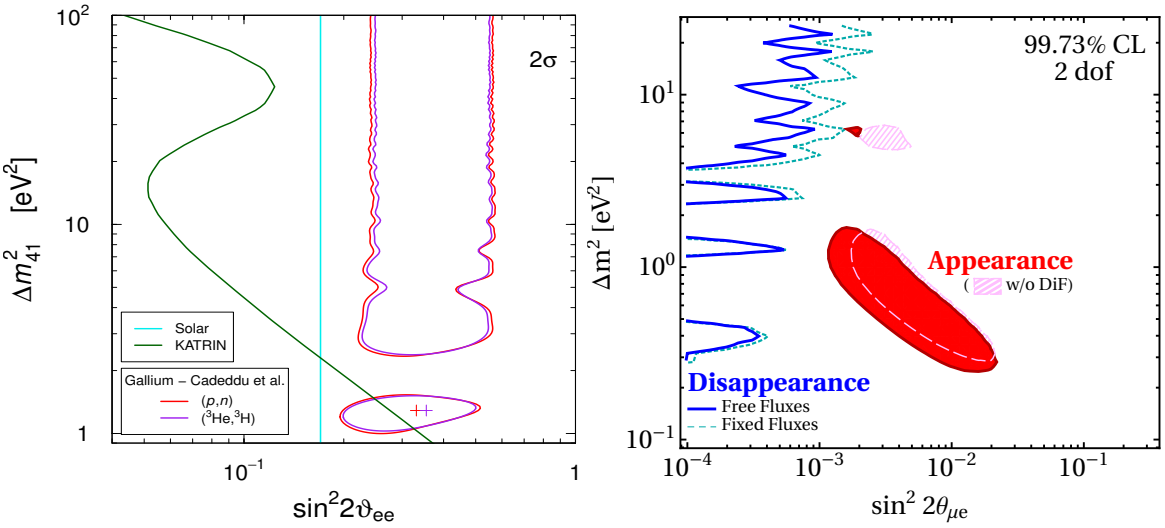


**Figure 14.10:** *Left*: Status of the intepretation of the Gallium anomaly in 3+1 scenarios from Ref. [217]. The contours *Right*: Preferred region of short-baseline appearance experiments (red region), compared to the region excluded by disappearance experiments (blue line) from Ref. [224].

But, generically, the results of all global analysis show that there is significant tension between groups of different data sets – in particular between appearance and disappearance results – and Eq. (14.89) makes it difficult to obtain a good global fit as illustrated in the right panel of Fig. 14.10 taken from Ref. [224] which concluded that 3+1 scenario is excluded at $4.7\sigma$ level pointing to the need of some additional form of new physics or to a combination of BSM and SM effects to account for all the anomalies. See Ref. [225] for a recent review on the subject. Cosmological observations can provide complementary information on the number of relativistic neutrino states in thermal equilibrium in the early Universe and on the sum of their masses, which sets further constraints on light sterile neutrino scenarios (see Chapter 26 of this *Review*, "Neutrinos in cosmology").

## 14.9 Laboratory Probes of $\nu$ Mass Scale and its Nature

As described in Secs.14.4 and 14.5, neutrino flavour oscillations in vacuum and flavour transitions in matter only depend on the differences between the neutrino masses-squared, $\Delta m^2_{ij}$, and on the mixing matrix elements, $U_{ij}$. However, they are insensitive to the absolute mass scale for the neutrinos, $m_i$. They also give us no information on whether they are Dirac or Majorana particles.

Clearly, the observation of flavour oscillations implies a lower bound on the mass of the heavier neutrino in $\Delta m^2_{ij}$, $|m_i| \geq \sqrt{\Delta m^2_{ij}}$ for $\Delta m^2_{ij} > 0$. However, there is no upper bound on $m_i$. In particular, oscillation results allow the neutrino spectrum to be approximately degenerate at a mass scale that is much higher than the $\sqrt{\Delta m^2_{ij}}$ that they determine. Information of the mass scale of the neutrino is provided by other types of experiments. Here we briefly summarize the most sensitive laboratory probes of the neutrino mass scale and on whether they are Dirac or Majorana particles. Cosmological observations provide, albeit indirectly, complementary information on the neutrino mass scale as it is reviewed in Chapter 26 of this *Review*, "Neutrinos in cosmology".

### 14.9.1 *Constraints from Kinematics of Weak Decays*

The only model-independent information on the neutrino masses, rather than mass differences, can be extracted from the energy-momentum conservation relation in reactions in which a neutrino or an antineutrino is involved.

Historically these bounds were labeled as limits on the mass of the flavour neutrino states corresponding to the charged flavour involved in the decay. Fermi proposed in 1933 such a kinematic search for the $\nu_e$ neutrino mass (which we will label here as $m^{\rm eff}_{\nu_e}$) in the end part of the beta spectra in $^3$H beta decay $^3\mathrm{H} \rightarrow ^3\mathrm{He} + e^- + \bar{\nu}_e$.

Because $^3$H beta decay is a superallowed transition, the nuclear matrix elements are energy independent, so the electron spectrum is determined exclusively by the phase space

$$\frac{dN}{dE} = C\, p\, E\, (Q-T)\sqrt{(Q-T)^2 - (m^{\rm eff}_{\nu_e})^2}\, F(E) \;\equiv\; R(E)\,\sqrt{(E_0-E)^2 - (m^{\rm eff}_{\nu_e})^2}\,. \tag{14.90}$$

$E_0$ is the mass difference between the inital and final nucleus, $E = T + m_e$ is the total electron energy, $p$ its momentum, $Q \equiv E_0 - m_e$ is the maximum kinetic energy of the electron and final state Coulomb interactions are contained in the Fermi function $F(E)$. $R(E)$ in the second equality contains all the $m_\nu$-independent factors.

The Kurie function is defined as $K(T) \equiv \sqrt{\frac{dN}{dE}\,\frac{1}{pEF(E)}}$. From Eq. (14.90), we see that if $m^{\rm eff}_{\nu_e}$=0 $K(T)$ would depend linearly on $T$. A non-vanishing neutrino mass then provokes a distortion from the straight-line $T$-dependence at the endpoint, So for $m^{\rm eff}_{\nu_e} = 0$, $T_{\rm max} = Q$, while for $m^{\rm eff}_{\nu_e} \neq 0$, $T_{\rm max} = Q - m^{\rm eff}_{\nu_e}$. In $^3$H beta decay $Q = 18.6$ KeV is very small and therefore, this decay is more sensitive to this $m^{\rm eff}_{\nu_e}$-induced distortion.

The most recent result on the kinematic search for neutrino mass in tritium decay is from KATRIN [226], an experiment which has found so far no indication of $m^{\rm eff}_{\nu_e} \neq 0$ and sets an upper limit

$$m^{\rm eff}_{\nu_e} < 0.45 \text{ eV}\,, \tag{14.91}$$

at 90% CL improving over the previous bound from the Mainz [227] and Troitsk [228] experiments which constrained $m^{\rm eff}_{\nu_e} < 2.2$ eV at 95% CL. KATRIN continues running and should soon reach its target sensitivity limit of $m^{\rm eff}_{\nu_e} \sim 0.3$ eV. Future experimental efforts on tritium beta decay include KATRIN++, PTOLEMY, and Project-8. In particular, Project 8 is exploring a new technique for $\beta$-spectrometry based on cyclotron radiation [229].

An alternative isotope to Tritium is $^{163}$Ho [230] which presents the advantage of a smaller $Q =$ 2.8 KeV. It decays via electron capture to $^{163}$Dy. Currently, there are two experiments exploring

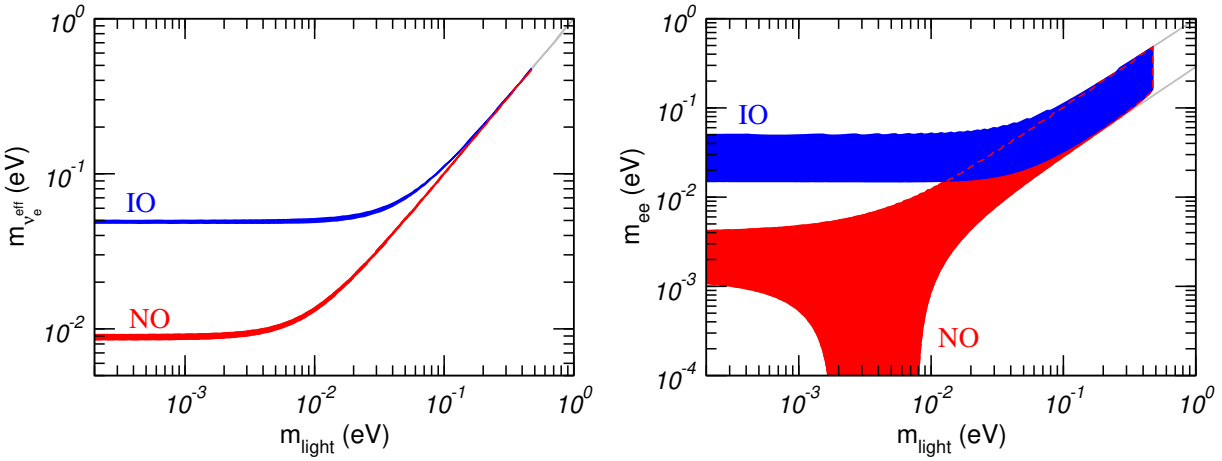


**Figure 14.11:** Allowed 95% CL ranges (1 dof) for the neutrino mass observable determined in $^3$H beta decay (left panel) and in $0\nu\beta\beta$ (right panel) in the framework of $3\nu$ mixing as a function of the lightest neutrino mass. The ranges are obtained by projecting the results of the global analysis of oscillation data (w/o SK-atm) in Ref. [193]. The region for each ordering is defined with respect to its local minimum.

this decay to probe the neutrino mass: ECHo [231], and HOLMES [232]. These experiments are complementary to tritium-based searches from a technical point of view. Also, the decay of $^{163}$Ho determines the effective electron neutrino mass as opposed to antineutrino in Tritium.

For the other flavours the present limits compiled in the listing section of the PDG read

$$m_{\nu_\mu}^{\rm eff} < 190 \text{ keV (90\% CL)} \qquad \text{from} \qquad \pi^- \to \mu^- + \bar{\nu}_\mu \,, \tag{14.92}$$

$$m_{\nu_\tau}^{\rm eff} < 18.2 \text{ MeV (95\% CL)} \qquad \text{from} \qquad \tau^- \to n\pi + \nu_\tau \,. \tag{14.93}$$

In the presence of mixing and for neutrinos with small mass differences, the distortion of the beta spectrum is given by the sum of the individual spectra generated incoherently by each neutrino massive state weighted with the relevant mixing matrix element squared [233]:

$$\frac{dN}{dE} = R(E) \sum_i |U_{ei}|^2 \sqrt{(E_0 - E)^2 - m_i^2}\, \Theta(E_0 - E - m_i) \,. \tag{14.94}$$

The step function $\Theta(E_0 - E - m_i)$ arises because a neutrino with a given mass $m_i$ can only be produced if the available energy is larger than its mass. Equation (14.94) shows the two main effects of the neutrino masses and mixings on the electron energy spectrum: First, kinks appear at the electron energies $E_e^{(i)} = E \sim E_0 - m_i$ with sizes that are determined by $|U_{ei}|^2$. Second, the endpoint shifts to $E_{\rm ep} = E_0 - m_0$, where $m_0$ is the lightest neutrino mass. Corrections are induced once the energy resolution of the experiment is considered. [234, 235]

In the 3-$\nu$ mixing scenario, the distortion of the spectrum can still be effectively described by a single parameter – which we denote as $m_{\nu_e}^{\rm eff}$ – if for all neutrino states $E_0 - E = Q - T \gg m_i$. In this case, one can expand Eq. (14.94) as:

$$\frac{dN}{dE} \simeq R(E) \sum_i |U_{ei}|^2 \sqrt{(E_0 - E)^2 - (m_{\nu_e}^{\rm eff})^2} \,, \tag{14.95}$$

with

$$(m_{\nu_e}^{\rm eff})^2 = \frac{\sum_i m_i^2 |U_{ei}|^2}{\sum_i |U_{ei}|^2} = \sum_i m_i^2 |U_{ei}|^2 \,, \tag{14.96}$$

where unitarity is assumed in the second equality. In this approximation, the distortion of the endpoint of the spectrum is described by a single parameter, and with the present results from KATRIN, it is bounded to be

$$0.45 \text{ eV} \geq m_{\nu_e}^{\rm eff} = \sqrt{\sum_i m_i^2 |U_{ei}|^2} = \begin{cases} \sqrt{m_0^2 + \Delta m_{21}^2 (1 - c_{13}^2 c_{12}^2) + \Delta m_{32}^2 s_{13}^2} & \text{in NO}\,, \\ \sqrt{m_0^2 - \Delta m_{21}^2 c_{13}^2 c_{12}^2 - \Delta m_{32}^2 c_{13}^2} & \text{in IO}\,, \end{cases} \tag{14.97}$$

where $m_0 = m_1\,(m_3)$ is the lightest neutrino mass in the NO (IO) spectrum. Correspondingly the bounds in Eqs.(14.92) and (14.93) apply to the combinations $\sum_i m_i^2 |U_{\alpha i}|^2$ for $\alpha = \mu$ and $\tau$ respectively. So with the values known of the mixing matrix elements, the strongest constraint on the absolute value of the neutrino mass comes from Tritium beta decay.

From Eq. (14.97) we see that, given the present knowledge of the neutrino mass differences and their mixing from oscillation experiments, it is possible to translate the experimental information of $m_{\nu_e}^{\rm eff}$ on a corresponding range for the lightest neutrino mass and that such relation depends on the ordering of the states. We plot in Fig. 14.11 the recasting of the allowed regions of the analysis in Ref. [193] in terms of the allowed range $m_{\nu_e}^{\rm eff}$ as a function of $m_{\rm light} \equiv m_0$. In particular, one finds that the results of oscillation experiments imply a lower bound on $m_{\nu_e}^{\rm eff} > 0.048$ (0.0085) eV for IO (NO) at 95% CL.

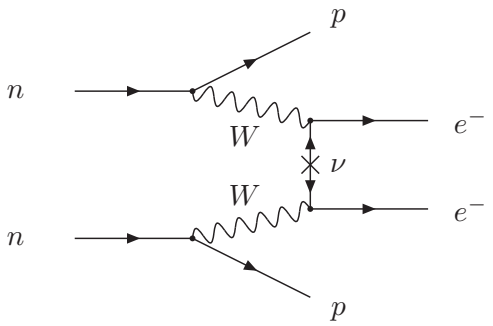


**Figure 14.12:** Feynman diagram for neutrinoless double-beta decay.

### 14.9.2 *Dirac vs. Majorana: Neutrinoless Double-beta Decay*

The most sensitive probe to whether neutrinos are Dirac or Majorana states is the neutrinoless double beta decay ($0\nu\beta\beta$):

$$(A, Z) \to (A, Z+2) + e^- + e^- . \tag{14.98}$$

In the presence of neutrino masses and mixing, the process in Eq. (14.98) can be generated at lower order in perturbation theory by the term represented in Fig. 14.12. The corresponding amplitude is proportional to the product of the two leptonic currents

$$M_{\alpha\beta} \propto [\bar{e}\gamma_\alpha(1-\gamma_5)\nu_e]\,[\bar{e}\gamma_\beta(1-\gamma_5)\nu_e] \propto \sum_i (U_{ei})^2\,[\bar{e}\gamma_\alpha(1-\gamma_5)\nu_i]\,[\bar{e}\gamma_\beta(1-\gamma_5)\nu_i]\,. \tag{14.99}$$

The neutrino propagator in Fig. 14.12 can only arise from the contraction $\langle 0\,|\,\nu_i(x)\nu_i(y)^T\,|\,0\rangle$. However, if the neutrino is a Dirac particle $\nu_i$ field annihilates a neutrino state and creates an antineutrino state, and neutrino and antineutrino states are different, so the contraction $\langle 0\,|\,\nu_i(x)\nu_i(y)^T\,|\,0\rangle =$

0 and $M_{\alpha\beta} = 0$. On the other hand, if $\nu_i$ is a Majorana particle, neutrino and antineutrino are described by the same field and $\langle 0 \,|\, \nu_i(x)\nu_i(y)^T \,|\, 0\rangle \neq 0$.

The conclusion is that in order to induce the $0\nu\beta\beta$ decay, neutrinos must be Majorana particles. This is consistent with the fact that the process (14.98) violates the total lepton number by two units. Conversely, if $0\nu\beta\beta$ decay is observed, massive neutrinos cannot be Dirac states [236].

It is important to stress that neutrinoless double-beta decay could be dominantly induced by other new physics effects beyond that of Majorana neutrino masses. Consequently, the connection between the observation or limitation of the neutrinoless double beta decay and the neutrino mass can only be made under some assumption about the source of total lepton number violation in the model.

The observable determined by the experiments is the half-life of the decay. Under the assumption that the Majorana neutrino mass is the only source of lepton number violation at low energies, the decay half-life is given by:

$$(T^{0\nu}_{1/2})^{-1} = G^{0\nu} \left| M^{0\nu} \right|^2 \left( \frac{m_{ee}}{m_e} \right)^2 , \tag{14.100}$$

where $G^{0\nu}$ is the phase space integral taking into account the final atomic state, $|M^{0\nu}|$ is the nuclear matrix element of the transition, and $m_{ee}$ is the *effective Majorana mass of* $\nu_e$,

$$\begin{aligned} m_{ee} &= \left| \sum_i m_i U_{ei}^2 \right| \\ &= \begin{cases} \left| m_0 c_{12}^2 c_{13}^2 + \sqrt{\Delta m_{21}^2 + m_0^2}\, s_{12}^2 c_{13}^2 e^{2i(\eta_2 - \eta_1)} + \sqrt{\Delta m_{32}^2 + \Delta m_{21}^2 + m_0^2}\, s_{13}^2 e^{-2i(\delta_{\rm CP} + \eta_1)} \right| & \text{in NO}\,, \\ \left| m_0 s_{13}^2 + \sqrt{m_0^2 - \Delta m_{32}^2}\, s_{12}^2 c_{13}^2 e^{2i(\eta_2 + \delta_{\rm CP})} + \sqrt{m_0^2 - \Delta m_{32}^2 - \Delta m_{21}^2}\, c_{12}^2 c_{13}^2 e^{2i(\eta_1 + \delta_{\rm CP})} \right| & \text{in IO}\,, \end{cases} \end{aligned} \tag{14.101}$$

which, in addition to the masses and mixing parameters that affect the tritium beta decay spectrum, also depends on the leptonic $CP$-violating phases. We plot in Fig. 14.11 the recasting of the allowed regions of the analysis in Ref. [193] in terms of the allowed range $m_{ee}$ as a function of $m_{\rm light} \equiv m_0$ for the two orderings. As a consequence of the dependence on the unknown Majorana phases, the allowed range of $m_{ee}$ for a given value of $m_{\rm light}$ and ordering is substantially broader than that of $m^{\rm eff}_{\nu_e}$. Nevertheless, the results of oscillation experiments imply a lower bound on the effective Majorana mass for the IO, which at 95%CL reads $m_{ee} > 0.016$ eV.

From Eq. (14.100) we see that nuclear structure details enter the relation between the decay rate (or lifetime) and the effective Majorana mass. As a consequence, uncertainties in the nuclear structure calculations result in a spread of $m_{ee}$ values for a given $T^{0\nu}_{1/2}$ by a factor of 2–3 [237].

We present in Sec. 14.9.3 a brief description of the experimental searches for neutrinoless double-beta decay. At the time of writing of this review, the strongest bound on $0\nu\beta\beta$ decay lifetimes came for Xenon and Germanium from the KamLAND-Zen [238] and GERDA [239] experiments, respectively. They have set a bound on the corresponding half-lives of $T^{0\nu}_{1/2} > 3.8 \times 10^{26}$ yr, and $T^{0\nu}_{1/2} > 1.8 \times 10^{26}$ yr, at 90% CL. Using a variety of nuclear matrix element calculations, the corresponding upper bounds on the effective Majorana mass are

$$m_{ee} < 28 - 122 \text{ meV} \tag{14.102}$$

$$m_{ee} < 79 - 180 \text{ meV}\,. \tag{14.103}$$

### 14.9.3 *Experimental Search for Neutrinoless Double-beta Decay*

There are 35 candidate nuclei for double-beta decay. Currently, experiments using $^{136}$Xe and $^{76}$Ge have reported the most sensitive searches for $0\nu\beta\beta$. In order to optimize the ability to observe

this process it is important to pursue searches with as many isotopes as possible. Indeed, different isotopes require different, complementary detection technologies, offer different uncertainties from nuclear matrix elements, different backgrounds, and further enable investigation of the mechanism behind the $0\nu\beta\beta$.

The $0\nu\beta\beta$ signature has two electrons whose energies sum to the $Q$-value of the nuclear transition. Their energies can be measured with ionization, scintillation, or through phonons, depending upon the detector technology. In some experiments, a combination of two techniques is used to enhance sensitivity. Assuming a background-free measurement, the sensitivity to the half-life is proportional to the product of the signal detection efficiency $\varepsilon$, the source mass $M$, and the measurement time $t$. If instead there are backgrounds, it is proportional to $\varepsilon\sqrt{\frac{Mt}{b\Delta E}}$, where $b$ is the background rate, and $\Delta E$ is the energy resolution.

Among experiments using ionization detection, ultra-high-purity germanium detectors provides the best sensitivity due to their high energy resolution and low background. GERDA has achieved a background level of $(5.2^{+1.6}_{-1.3}) \times 10^{-4}$ counts/(keV·kg·year) [239], which enabled a background-free search. The final result from GERDA on the $0\nu\beta\beta$ half-life of $^{76}$Ge limits it to $T_{1/2} > 1.8{\times}10^{26}$ years at 90% CL. The Majorana Demonstrator achieved energy resolution of 2.5 keV FWHM (full width at half maximum) at the Q-value (2.039 MeV) [240] and set a half-life limit of $T_{1/2} > 8.3 \times 10^{25}$ years at 90% CL. The GERDA and Majorana collaborations have united and formed, together with new groups, the LEGEND collaboration. LEGEND has adopted a phased approach toward the deployment of a tonne of enriched Ge detectors [241]. The first phase of LEGEND based on approximately 200 kg of enriched Ge uses the GERDA infrastructure at LNGS and has sharted taking it's first data. The second phase of LEGEND has been approved as a one ton experiment in a new cryostat reaching a discovery sensitivity of half-lifes beyond $10^{28}$ years. In China, CDEX-300$\nu$ will use 225 kg of enriched Ge is under preparation [242] in the existing CEDX-DM infrastructure at the China Jinping Underground Laboratory.

Liquid scintillator detectors have a simple structure that can be used in existing large detectors with low background environments. By adding an inner balloon to contain xenon-loaded liquid scintillator to the KamLAND detector, KamLAND-Zen uses 745 kg of xenon that is 90.9% enriched in $^{136}$Xe. KamLAND-Zen reported a half-life limit of $> 3.8 \times 10^{26}$ years at 90% CL [238]. The SNO detector has also been upgraded to hold liquid scintillator for the SNO+ experiment [243]. SNO+ will be loaded with 0.5% natural tellurium, corresponding to approximately 1.3 t of $^{130}$Te in order to search for $0\nu\beta\beta$.

With a time projection chamber, one can utilize both ionization and scintillation signals. EXO-200 used a liquid xenon time projection chamber with enriched Xe and reported a half-life limit of $T_{1/2} > 3.5 \times 10^{25}$ years at 90% CL [244] for $^{136}$Xe. Based on the technology validated by EXO-200, nEXO plans to use about 5,000 kg of enriched xenon [245]. NEXT has been developing a high-pressure xenon gas time projection chamber with electroluminescent amplification and optical readouts. An energy resolution of 1% FWHM at the Q-value of $^{136}$Xe $0\nu\beta\beta$ has demonstrated with NEXT-White detector [246].

CUORE uses a cryogenic bolometer to measure the recoil electron energies in a calorimetric way. The detector is composed of 988 $TeO_2$ bolometers with a total mass of 742 kg, corresponding to 206 kg of $^{130}$Te, and was operated at 10 mK. CUORE set a half-life limit of $T_{1/2} > 3.5 \times 10^{25}$ years at 90% CL for $^{130}$Te [247]. In order to further reduce backgrounds for future searches based on the CUORE technology, CUPID proposes to simultaneously measure the calorimetric signal and the scintillation light with a tonne-scale bolometric detector. A prototype has been used to demonstrate the technology and also to search for $0\nu\beta\beta$ with $^{82}$Se [248] and $^{100}$Mo [249].

AMoRE also uses the simultaneous detection of heat and scintillation. Using $^{100}$Mo-enriched

and $^{48}$Ca-depleted $CaMoO_4$ crystals with a total mass of 6.2 kg (AMoRE-I) were operated in Yangyang underground laboratory located in South Korea, searching for $0\nu\beta\beta$ with $^{100}$Mo [250]. The AMoRE-I experiment has established a half-life limit of $T_{1/2} > 2.9\times10^{24}$ with this isotope [251].

A tracker-calorimeter technique is employed in NEMO. Source isotopes are hosted in thin foils surrounded by a tracking detector, which in turn is surrounded by a calorimeter. Full topological event reconstruction with this configuration enables background rejection and which can provide additional event information in the event of a discovery. The NEMO-3 experiment used seven isotopes, the largest of which was 7 kg of $^{100}$Mo. No evidence of a signal was found in a 34.3 kg-yr exposure of this isotope, resulting in a lower limit of $T_{1/2} > 1.1 \times 10^{24}$ [252].

***References***


[1] J. N. Bahcall, *NEUTRINO ASTROPHYSICS* (1989), ISBN 9780521379755.

[2] R. N. Mohapatra and P. B. Pal, World Sci. Lect. Notes Phys. **60**, 1 (1998), [World Sci. Lect. Notes Phys.72,1(2004)].

[3] C. W. Kim and A. Pevsner, Contemp. Concepts Phys. **8**, 1 (1993).

[4] B. Kayser, F. Gibrat-Debu and F. Perrier, World Sci. Lect. Notes Phys. **25**, 1 (1989).

[5] C. Giunti and C. W. Kim, *Fundamentals of Neutrino Physics and Astrophysics* (2007), ISBN 9780198508717.

[6] M. C. Gonzalez-Garcia and Y. Nir, Rev. Mod. Phys. **75**, 345 (2003), [hep-ph/0202058].

[7] M. C. Gonzalez-Garcia and M. Maltoni, Phys. Rept. **460**, 1 (2008), [arXiv:0704.1800].

[8] A. Pilaftsis, Z. Phys. **C55**, 275 (1992), [hep-ph/9901206].

[9] P. Minkowski, Phys. Lett. **67B**, 421 (1977).

[10] P. Ramond, in "International Symposium on Fundamentals of Quantum Theory and Quantum Field Theory," (1979), [hep-ph/9809459].

[11] M. Gell-Mann, P. Ramond and R. Slansky, Conf. Proc. **C790927**, 315 (1979), [arXiv:1306.4669].

[12] T. Yanagida, Conf. Proc. C **7902131**, 95 (1979).

[13] R. N. Mohapatra and G. Senjanovic, Phys. Rev. Lett. **44**, 912 (1980).

[14] J. Schechter and J. W. F. Valle, Phys. Rev. **D21**, 309 (1980).

[15] J. Schechter and J. W. F. Valle, Phys. Rev. **D22**, 2227 (1980).

[16] J. Schechter and J. W. F. Valle, Phys. Rev. **D24**, 1883 (1981), [Erratum: Phys. Rev.D25,283(1982)].

[17] Z. Maki, M. Nakagawa and S. Sakata, Prog. Theor. Phys. **28**, 870 (1962).

[18] Y. Katayama *et al.*, Prog. Theor. Phys. **28**, 675 (1962).

[19] B. Pontecorvo, Zh. Eksp. Teor. Fiz. **53**, 1717 (1967).

[20] N. Cabibbo, Phys. Rev. Lett. **10**, 531 (1963).

[21] M. Kobayashi and T. Maskawa, Prog. Theor. Phys. **49**, 652 (1973).

[22] S. Antusch *et al.*, JHEP **10**, 084 (2006), [hep-ph/0607020].

[23] S. Antusch and O. Fischer, JHEP **10**, 094 (2014), [arXiv:1407.6607].

[24] V. N. Gribov and B. Pontecorvo, Phys. Lett. **28B**, 493 (1969).

[25] E. Akhmedov, in "International Conference on History of the Neutrino: 1930-2018 Paris, France, September 5-7, 2018," (2019), [arXiv:1901.05232].

[26] L. Wolfenstein, Phys. Rev. D **17**, 2369 (1978).

[27] A. Halprin, Phys. Rev. **D34**, 3462 (1986).

[28] A. J. Baltz and J. Weneser, Phys. Rev. **D37**, 3364 (1988).

[29] P. D. Mannheim, Phys. Rev. **D37**, 1935 (1988).

[30] L. Landau, Phys. Z. Sov. **2**, 46 (1932).

[31] C. Zener, Proc. Roy. Soc. Lond. **A137**, 696 (1932).

[32] E. Majorana, Nuovo Cim. **9**, 43 (1932).

[33] E. C. G. Stueckelberg, Helv. Phys. Acta **5**, 369 (1932).

[34] T.-K. Kuo and J. T. Pantaleone, Rev. Mod. Phys. **61**, 937 (1989).

[35] S. J. Parke, Phys. Rev. Lett. **57**, 1275 (1986).

[36] W. C. Haxton, Phys. Rev. Lett. **57**, 1271 (1986).

[37] S. T. Petcov, Phys. Lett. B **191**, 299 (1987).

[38] S. P. Mikheyev and A. Y. Smirnov, Sov. J. Nucl. Phys. **42**, 913 (1985).

[39] J. N. Bahcall *et al.*, Rev. Mod. Phys. **54**, 767 (1982).

[40] J. N. Bahcall, A. M. Serenelli and S. Basu, Astrophys. J. **621**, L85 (2005), [arXiv:astro-ph/0412440].

[41] A. M. Serenelli, W. C. Haxton and C. Pena-Garay, Astrophys. J. **743**, 24 (2011), [arXiv:1104.1639].

[42] F. L. Villante, Phys. Lett. **B742**, 279 (2015), [arXiv:1410.2796].

[43] A. Serenelli, Eur. Phys. J. **A52**, 4, 78 (2016), [arXiv:1601.07179].

[44] R. Davis, Jr., D. S. Harmer and K. C. Hoffman, Phys. Rev. Lett. **20**, 1205 (1968).

[45] B. T. Cleveland *et al.*, Astrophys. J. **496**, 505 (1998).

[46] C. Pena-Garay and A. Serenelli (2008), [arXiv:0811.2424].

[47] J. N. Abdurashitov *et al.* (SAGE), J. Exp. Theor. Phys. **95**, 181 (2002), [Zh. Eksp. Teor. Fiz.122,211(2002)], [arXiv:astro-ph/0204245].

[48] W. Hampel *et al.* (GALLEX), Phys. Lett. **B447**, 127 (1999).

[49] M. Altmann *et al.* (GNO), Phys. Lett. **B616**, 174 (2005), [hep-ex/0504037].

[50] J. N. Abdurashitov *et al.* (SAGE), Phys. Rev. **C80**, 015807 (2009), [arXiv:0901.2200].

[51] K. S. Hirata *et al.* (Kamiokande-II), Phys. Rev. Lett. **63**, 16 (1989).

[52] Y. Fukuda *et al.* (Kamiokande), Phys. Rev. Lett. **77**, 1683 (1996).

[53] Y. Fukuda *et al.* (Super-Kamiokande), Phys. Rev. Lett. **81**, 1158 (1998), [Erratum: Phys.Rev.Lett. 81, 4279 (1998)], [hep-ex/9805021].

[54] K. Abe *et al.* (Super-Kamiokande), Phys. Rev. D **94**, 5, 052010 (2016), [arXiv:1606.07538].

[55] N. Vinyoles *et al.*, Astrophys. J. **835**, 2, 202 (2017), [arXiv:1611.09867].

[56] S. Fukuda *et al.* (Super-Kamiokande), Phys. Rev. Lett. **86**, 5656 (2001), [hep-ex/0103033].

[57] H. H. Chen, Phys. Rev. Lett. **55**, 1534 (1985).

[58] B. Aharmim *et al.* (SNO), Phys. Rev. **C72**, 055502 (2005), [arXiv:nucl-ex/0502021].

[59] S. Fukuda *et al.* (Super-Kamiokande), Phys. Lett. **B539**, 179 (2002), [hep-ex/0205075].

[60] Q. R. Ahmad *et al.* (SNO), Phys. Rev. Lett. **87**, 071301 (2001), [arXiv:nucl-ex/0106015].

[61] S. Fukuda *et al.* (Super-Kamiokande), Phys. Rev. Lett. **86**, 5651 (2001), [hep-ex/0103032].

[62] Q. R. Ahmad *et al.* (SNO), Phys. Rev. Lett. **89**, 011301 (2002), [arXiv:nucl-ex/0204008].

[63] B. Aharmim *et al.* (SNO), Phys. Rev. **C88**, 025501 (2013), [arXiv:1109.0763].
[64] J. Bergstrom *et al.*, JHEP **03**, 132 (2016), [arXiv:1601.00972].
[65] C. Arpesella *et al.* (Borexino), Phys. Lett. B **658**, 101 (2008), [arXiv:0708.2251].
[66] G. Bellini *et al.* (Borexino), Phys. Rev. Lett. **108**, 051302 (2012), [arXiv:1110.3230].
[67] M. Agostini *et al.* (BOREXINO), Nature **562**, 7728, 505 (2018).
[68] M. Agostini *et al.* (BOREXINO), Nature **587**, 577 (2020), [arXiv:2006.15115].
[69] G. Bellini *et al.* (Borexino), Phys. Rev. D **82**, 033006 (2010), [arXiv:0808.2868].
[70] M. Agostini *et al.* (Borexino), Phys. Rev. D **100**, 8, 082004 (2019), [arXiv:1707.09279].
[71] M. Agostini *et al.* (Borexino), Phys. Rev. D **101**, 6, 062001 (2020), [arXiv:1709.00756].
[72] S. Abe *et al.* (KamLAND), Phys. Rev. **C84**, 035804 (2011), [arXiv:1106.0861].
[73] A. Gando *et al.* (KamLAND), Phys. Rev. **C92**, 5, 055808 (2015), [arXiv:1405.6190].
[74] M. Honda *et al.*, Phys. Rev. **D92**, 2, 023004 (2015), [arXiv:1502.03916].
[75] G. D. Barr *et al.*, Phys. Rev. **D74**, 094009 (2006), [arXiv:astro-ph/0611266].
[76] G. Battistoni *et al.*, Astropart. Phys. **19**, 269 (2003), [Erratum: Astropart. Phys.19,291(2003)], [hep-ph/0207035].
[77] J. Evans *et al.*, Phys. Rev. **D95**, 2, 023012 (2017), [arXiv:1612.03219].
[78] C. V. Achar *et al.*, Phys. Lett. **18**, 196 (1965).
[79] F. Reines *et al.*, Phys. Rev. Lett. **15**, 429 (1965).
[80] K. S. Hirata *et al.* (Kamiokande-II), Phys. Lett. B **205**, 416 (1988).
[81] D. Casper *et al.*, Phys. Rev. Lett. **66**, 2561 (1991).
[82] K. Daum *et al.* (Frejus), Z. Phys. **C66**, 417 (1995).
[83] M. Aglietta *et al.* (NUSEX), Europhys. Lett. **8**, 611 (1989).
[84] K. S. Hirata *et al.* (Kamiokande-II), Phys. Lett. **B280**, 146 (1992).
[85] Y. Fukuda *et al.* (Kamiokande), Phys. Lett. **B335**, 237 (1994).
[86] Y. Fukuda *et al.* (Super-Kamiokande), Phys. Rev. Lett. **81**, 1562 (1998), [hep-ex/9807003].
[87] M. Ambrosio *et al.* (MACRO), Phys. Lett. **B517**, 59 (2001), [hep-ex/0106049].
[88] M. C. Sanchez *et al.* (Soudan 2), Phys. Rev. **D68**, 113004 (2003), [hep-ex/0307069].
[89] V. D. Barger *et al.*, Phys. Rev. Lett. **82**, 2640 (1999), [arXiv:astro-ph/9810121].
[90] E. Lisi, A. Marrone and D. Montanino, Phys. Rev. Lett. **85**, 1166 (2000), [hep-ph/0002053].
[91] Y. Ashie *et al.* (Super-Kamiokande), Phys. Rev. Lett. **93**, 101801 (2004), [hep-ex/0404034].
[92] Z. Li *et al.* (Super-Kamiokande), Phys. Rev. **D98**, 5, 052006 (2018), [arXiv:1711.09436].
[93] M. G. Aartsen *et al.* (IceCube), Phys. Rev. **D99**, 3, 032007 (2019), [arXiv:1901.05366].
[94] K. Abe *et al.* (Super-Kamiokande), Phys. Rev. **D97**, 7, 072001 (2018), [arXiv:1710.09126].
[95] A. Albert *et al.* (ANTARES), JHEP **06**, 113 (2019), [arXiv:1812.08650].
[96] R. Abbasi *et al.* ((IceCube Collaboration)‖, IceCube), Phys. Rev. Lett. **134**, 9, 091801 (2025), [arXiv:2405.02163].
[97] M. G. Aartsen *et al.* (IceCube-Gen2), J. Phys. G **48**, 6, 060501 (2021), [arXiv:2008.04323].
[98] S. Adrian-Martinez *et al.* (KM3Net), J. Phys. **G43**, 8, 084001 (2016), [arXiv:1601.07459].
[99] S. Aiello *et al.* (KM3NeT), JHEP **10**, 206 (2024), [arXiv:2408.07015].
[100] S. Ahmed *et al.* (ICAL), Pramana **88**, 5, 79 (2017), [arXiv:1505.07380].

[101] K. Abe *et al.* (Hyper-Kamiokande) (2018), [arXiv:1805.04163].
[102] B. Abi *et al.* (DUNE), JINST **15**, 08, T08008 (2020), [arXiv:2002.02967].
[103] S. E. Kopp, Phys. Rept. **439**, 101 (2007), [arXiv:physics/0609129].
[104] S. van der Meer (1961), CERN-61-07.
[105] D. G. Michael *et al.* (MINOS), Nucl. Instrum. Meth. A **596**, 190 (2008), [arXiv:0805.3170].
[106] S. H. Ahn *et al.* (K2K), Phys. Lett. B **511**, 178 (2001), [hep-ex/0103001].
[107] D. Beavis *et al.* (E899) (1995), BNL-52459.
[108] K. Abe *et al.* (T2K), Nucl. Instrum. Meth. A **659**, 106 (2011), [arXiv:1106.1238].
[109] D. S. Ayres *et al.* (NOvA) (2007).
[110] M. G. Catanesi *et al.* (HARP), Nucl. Instrum. Meth. **A571**, 527 (2007).
[111] J. M. Paley *et al.* (MIPP), Phys. Rev. **D90**, 3, 032001 (2014), [arXiv:1404.5882].
[112] N. Abgrall *et al.* (NA61), JINST **9**, P06005 (2014), [arXiv:1401.4699].
[113] M. Pavin *et al.* (EMPHATIC), Phys. Rev. D **106**, 11, 112008 (2022), [arXiv:2106.15723].
[114] N. Abgrall *et al.* (NA61/SHINE), Eur. Phys. J. C **76**, 2, 84 (2016), [arXiv:1510.02703].
[115] N. Abgrall *et al.* (NA61/SHINE), Eur. Phys. J. C **79**, 2, 100 (2019), [arXiv:1808.04927].
[116] H. Adhikary *et al.* (NA61/SHINE) (2023), [arXiv:2306.02961].
[117] M. H. Ahn *et al.* (K2K), Phys. Rev. **D74**, 072003 (2006), [hep-ex/0606032].
[118] P. Adamson *et al.* (MINOS), Phys. Rev. Lett. **112**, 191801 (2014), [arXiv:1403.0867].
[119] P. Adamson *et al.* (MINOS+), Phys. Rev. Lett. **125**, 13, 131802 (2020), [arXiv:2006.15208].
[120] N. Agafonova *et al.* (OPERA), Phys. Rev. Lett. **120**, 21, 211801 (2018), [Erratum: Phys. Rev. Lett.121,no.13,139901(2018)], [arXiv:1804.04912].
[121] C. Rubbia *et al.*, JINST **6**, P07011 (2011), [arXiv:1106.0975].
[122] K. Abe *et al.* (T2K), Phys. Rev. Lett. **107**, 041801 (2011), [arXiv:1106.2822].
[123] K. Abe *et al.* (T2K), Phys. Rev. Lett. **112**, 061802 (2014), [arXiv:1311.4750].
[124] K. Abe *et al.* (T2K), Eur. Phys. J. C **83**, 9, 782 (2023), [arXiv:2303.03222].
[125] P. Adamson *et al.* (NOvA), Phys. Rev. Lett. **118**, 23, 231801 (2017), [arXiv:1703.03328].
[126] M. A. Acero *et al.* (NOvA), Phys. Rev. Lett. **123**, 15, 151803 (2019), [arXiv:1906.04907].
[127] M. A. Acero *et al.* (NOvA), Phys. Rev. D **106**, 3, 032004 (2022), [arXiv:2108.08219].
[128] A. Aguilar-Arevalo *et al.* (LSND), Phys. Rev. **D64**, 112007 (2001), [hep-ex/0104049].
[129] B. Armbruster *et al.* (KARMEN), Phys. Rev. **D65**, 112001 (2002), [hep-ex/0203021].
[130] A. A. Aguilar-Arevalo *et al.* (MiniBooNE), Phys. Rev. D **103**, 5, 052002 (2021), [arXiv:2006.16883].
[131] M. Antonello *et al.* (MicroBooNE, LAr1-ND, ICARUS-WA104) (2015), [arXiv:1503.01520].
[132] P. Abratenko *et al.* (MicroBooNE), Phys. Rev. Lett. **128**, 24, 241801 (2022), [arXiv:2110.14054].
[133] P. Abratenko *et al.* (MicroBooNE), Phys. Rev. Lett. **130**, 1, 011801 (2023), [arXiv:2210.10216].
[134] S. Ajimura *et al.* (JSNS2), Nucl. Instrum. Meth. A **1014**, 165742 (2021), [arXiv:2104.13169].
[135] F. Von Feilitzsch, A. A. Hahn and K. Schreckenbach, Phys. Lett. **118B**, 162 (1982).
[136] K. Schreckenbach *et al.*, Phys. Lett. **160B**, 325 (1985).

[137] A. A. Hahn *et al.*, Phys. Lett. **B218**, 365 (1989).

[138] P. Vogel *et al.*, Phys. Rev. **C24**, 1543 (1981).

[139] T. A. Mueller *et al.*, Phys. Rev. **C83**, 054615 (2011), [arXiv:1101.2663].

[140] P. Huber, Phys. Rev. **C84**, 024617 (2011), [Erratum: Phys. Rev.C85,029901(2012)], [arXiv:1106.0687].

[141] F. P. An *et al.* (Daya Bay), Phys. Rev. Lett. **116**, 6, 061801 (2016), [Erratum: Phys. Rev. Lett.118,no.9,099902(2017)], [arXiv:1508.04233].

[142] F. P. An *et al.* (Daya Bay), Phys. Rev. Lett. **118**, 25, 251801 (2017), [arXiv:1704.01082].

[143] D. Adey *et al.* (Daya Bay), Phys. Rev. D **100**, 5, 052004 (2019), [arXiv:1808.10836].

[144] F. P. An *et al.* (Daya Bay), Phys. Rev. Lett. **134**, 20, 201802 (2025), [arXiv:2501.00746].

[145] V. Kopeikin, M. Skorokhvatov and O. Titov, Phys. Rev. D **104**, 7, L071301 (2021), [arXiv:2103.01684].

[146] M. Estienne *et al.*, Phys. Rev. Lett. **123**, 2, 022502 (2019), [arXiv:1904.09358].

[147] L. Hayen *et al.*, Phys. Rev. C **100**, 5, 054323 (2019), [arXiv:1908.08302].

[148] G. Bak *et al.* (RENO), Phys. Rev. Lett. **121**, 20, 201801 (2018), [arXiv:1806.00248].

[149] H. de Kerret *et al.* (Double Chooz), Nature Phys. **16**, 5, 558 (2020), [arXiv:1901.09445].

[150] Y. J. Ko *et al.* (NEOS), Phys. Rev. Lett. **118**, 12, 121802 (2017), [arXiv:1610.05134].

[151] K. Eguchi *et al.* (KamLAND), Phys. Rev. Lett. **90**, 021802 (2003), [hep-ex/0212021].

[152] T. Araki *et al.* (KamLAND), Phys. Rev. Lett. **94**, 081801 (2005), [hep-ex/0406035].

[153] A. Gando *et al.* (KamLAND), Phys. Rev. **D88**, 3, 033001 (2013), [arXiv:1303.4667].

[154] Y. Abe *et al.* (Double Chooz), Phys. Rev. Lett. **108**, 131801 (2012), [arXiv:1112.6353].

[155] F. P. An *et al.* (Daya Bay), Phys. Rev. Lett. **108**, 171803 (2012), [arXiv:1203.1669].

[156] J. K. Ahn *et al.* (RENO), Phys. Rev. Lett. **108**, 191802 (2012), [arXiv:1204.0626].

[157] F. P. An *et al.* (Daya Bay), Phys. Rev. Lett. **130**, 16, 161802 (2023), [arXiv:2211.14988].

[158] S. Jeon *et al.* (RENO), Phys. Rev. D **111**, 11, 112006 (2025).

[159] A. Abusleme *et al.* (JUNO), Prog. Part. Nucl. Phys. **123**, 103927 (2022), [arXiv:2104.02565].

[160] A. Abusleme *et al.* (JUNO), Chin. Phys. C **46**, 12, 123001 (2022), [arXiv:2204.13249].

[161] Z. Atif *et al.* (RENO, NEOS), Phys. Rev. D **105**, 11, L111101 (2022), [arXiv:2011.00896].

[162] I. Alekseev *et al.* (DANSS), Phys. Lett. **B787**, 56 (2018), [arXiv:1804.04046].

[163] H. Almazán *et al.* (STEREO), Phys. Rev. D **102**, 5, 052002 (2020), [arXiv:1912.06582].

[164] H. Almazán *et al.* (STEREO), Nature **613**, 7943, 257 (2023), [arXiv:2210.07664].

[165] M. Andriamirado *et al.* (PROSPECT), Phys. Rev. D **103**, 3, 032001 (2021), [arXiv:2006.11210].

[166] A. P. Serebrov *et al.* (NEUTRINO-4), Pisma Zh. Eksp. Teor. Fiz. **109**, 4, 209 (2019), [JETP Lett.109,no.4,213(2019)], [arXiv:1809.10561].

[167] A. P. Serebrov *et al.*, Phys. Rev. D **104**, 3, 032003 (2021), [arXiv:2005.05301].

[168] Y. Abreu *et al.* (SoLid), JINST **16**, 02, P02025 (2021), [arXiv:2002.05914].

[169] N. Cabibbo, Phys. Lett. **72B**, 333 (1978).

[170] S. M. Bilenky, J. Hosek and S. T. Petcov, Phys. Lett. **94B**, 495 (1980).

[171] V. D. Barger, K. Whisnant and R. J. N. Phillips, Phys. Rev. Lett. **45**, 2084 (1980).

[172] P. Langacker *et al.*, Nucl. Phys. **B282**, 589 (1987).

[173] S. Goswami and A. Yu. Smirnov, Phys. Rev. **D72**, 053011 (2005), [hep-ph/0411359].

[174] N. Okamura, Prog. Theor. Phys. **114**, 1045 (2006), [hep-ph/0411388].

[175] H. Nunokawa, S. J. Parke and R. Zukanovich Funchal, Phys. Rev. **D72**, 013009 (2005), [hep-ph/0503283].

[176] A. Cervera *et al.*, Nucl. Phys. **B579**, 17 (2000), [Erratum: Nucl. Phys.B593,731(2001)], [hep-ph/0002108].

[177] M. Freund, Phys. Rev. **D64**, 053003 (2001), [hep-ph/0103300].

[178] E. K. Akhmedov *et al.*, JHEP **04**, 078 (2004), [hep-ph/0402175].

[179] H. Minakata *et al.*, Phys. Rev. **D74**, 053008 (2006), [hep-ph/0607284].

[180] O. L. G. Peres and A. Yu. Smirnov, Nucl. Phys. **B680**, 479 (2004), [hep-ph/0309312].

[181] S. Petcov, Phys.Lett. **B434**, 321 (1998), [hep-ph/9805262].

[182] E. K. Akhmedov *et al.*, Nucl.Phys. **B542**, 3 (1999), [hep-ph/9808270].

[183] E. K. Akhmedov, Nucl.Phys. **B538**, 25 (1999), [hep-ph/9805272].

[184] M. Chizhov, M. Maris and S. Petcov (1998), SISSA-53-98-EP, [hep-ph/9810501].

[185] M. Chizhov and S. Petcov, Phys.Rev.Lett. **83**, 1096 (1999), [hep-ph/9903399].

[186] E. K. Akhmedov, M. Maltoni and A. Y. Smirnov, JHEP **0705**, 077 (2007), [hep-ph/0612285].

[187] C. Kim and U. Lee, Phys.Lett. **B444**, 204 (1998), [hep-ph/9809491].

[188] O. Peres and A. Y. Smirnov, Phys.Lett. **B456**, 204 (1999), [hep-ph/9902312].

[189] M. Gonzalez-Garcia, M. Maltoni and A. Y. Smirnov, Phys.Rev. **D70**, 093005 (2004), [hep-ph/0408170].

[190] E. K. Akhmedov, M. Maltoni and A. Y. Smirnov, JHEP **0806**, 072 (2008), [arXiv:0804.1466].

[191] J. Bernabeu, S. Palomares Ruiz and S. Petcov, Nucl.Phys. **B669**, 255 (2003), [hep-ph/0305152].

[192] S. Petcov and T. Schwetz, Nucl.Phys. **B740**, 1 (2006), [hep-ph/0511277].

[193] I. Esteban *et al.*, JHEP **12**, 216 (2024), [arXiv:2410.05380].

[194] F. Capozzi *et al.*, Phys. Rev. D **111**, 9, 093006 (2025), [arXiv:2503.07752].

[195] M. Tortola, Neutrinos global fit (2024), Talk at XV Latin American Symposium on High Energy Physics, URL `https://indico.nucleares.unam.mx/event/2125/contribution/40`.

[196] P. F. de Salas *et al.*, JHEP **02**, 071 (2021), [arXiv:2006.11237].

[197] Atmospheric neutrino oscillation analysis with neutron tagging and an expanded fiducial volume in Super-Kamiokande I-V (2024), ZENODO.

[198] Data release for neutrino oscillation parameters using convolutional neural networks with 9.3 years of data in IceCube DeepCore (2024), .

[199] T. Wester *et al.* (Super-Kamiokande) (2023), [arXiv:2311.05105].

[200] R. Abbasi *et al.* (IceCube) (2024), [arXiv:2405.02163].

[201] J. Wolcott (NOvA) FERMILAB-SLIDES-24-0130-PPD (2024).

[202] C. Jarlskog, Phys. Rev. Lett. **55**, 1039 (1985).

[203] M. C. Gonzalez-Garcia, M. Maltoni and T. Schwetz, JHEP **11**, 052 (2014), [arXiv:1409.5439].

[204] Y. Farzan and A. Yu. Smirnov, Phys. Rev. **D65**, 113001 (2002), [hep-ph/0201105].

[205] A. Dueck, S. Petcov and W. Rodejohann, Phys. Rev. **D82**, 013005 (2010), [arXiv:1006.0227].

[206] A. Aguilar-Arevalo *et al.* (MiniBooNE) (2012), [arXiv:1207.4809].

[207] R. Acciarri *et al.* (MicroBooNE), JINST **12**, 02, P02017 (2017), [arXiv:1612.05824].

[208] P. Abratenko *et al.* ((MicroBooNE Collaboration)*, MicroBooNE), Phys. Rev. Lett. **135**, 8, 081802 (2025), [arXiv:2412.14407].

[209] G. Mention *et al.*, Phys. Rev. **D83**, 073006 (2011), [arXiv:1101.2755].

[210] C. Giunti *et al.*, Phys. Lett. B **829**, 137054 (2022), [arXiv:2110.06820].

[211] V. V. Barinov *et al.*, Phys. Rev. Lett. **128**, 23, 232501 (2022), [arXiv:2109.11482].

[212] M. A. Acero, C. Giunti and M. Laveder, Phys. Rev. **D78**, 073009 (2008), [arXiv:0711.4222].

[213] C. Giunti and M. Laveder, Phys. Rev. **C83**, 065504 (2011), [arXiv:1006.3244].

[214] C. Giunti *et al.*, JHEP **10**, 164 (2022), [arXiv:2209.00916].

[215] M. C. Gonzalez-Garcia, M. Maltoni and J. P. Pinheiro, Phys. Lett. B **862**, 139297 (2025), [arXiv:2411.16840].

[216] H. Acharya *et al.* (KATRIN) (2025), [arXiv:2503.18667].

[217] M. Cadeddu *et al.* (2025), [arXiv:2507.13103].

[218] J. J. Gomez-Cadenas and M. C. Gonzalez-Garcia, Z. Phys. **C71**, 443 (1996), [hep-ph/9504246].

[219] C. Giunti and M. Laveder, Phys. Rev. **D84**, 093006 (2011), [arXiv:1109.4033].

[220] J. M. Conrad *et al.*, Adv. High Energy Phys. **2013**, 163897 (2013), [arXiv:1207.4765].

[221] J. Kopp *et al.*, JHEP **05**, 050 (2013), [arXiv:1303.3011].

[222] G. H. Collin *et al.*, Phys. Rev. Lett. **117**, 22, 221801 (2016), [arXiv:1607.00011].

[223] S. Gariazzo *et al.*, JHEP **06**, 135 (2017), [arXiv:1703.00860].

[224] M. Dentler *et al.*, JHEP **08**, 010 (2018), [arXiv:1803.10661].

[225] M. A. Acero *et al.*, J. Phys. G **51**, 12, 120501 (2024), [arXiv:2203.07323].

[226] M. Aker *et al.* (KATRIN), Science **388**, 6743, adq9592 (2025), [arXiv:2406.13516].

[227] J. Bonn *et al.*, Nucl. Phys. B Proc. Suppl. **91**, 273 (2001).

[228] V. M. Lobashev *et al.*, Nucl. Phys. B Proc. Suppl. **91**, 280 (2001).

[229] A. Ashtari Esfahani *et al.* (Project 8), Phys. Rev. Lett. **131**, 10, 102502 (2023), [arXiv:2212.05048].

[230] A. De Rujula and M. Lusignoli, Phys. Lett. **118B**, 429 (1982).

[231] L. Gastaldo *et al.*, J. Low Temp. Phys. **176**, 5-6, 876 (2014), [arXiv:1309.5214].

[232] B. Alpert *et al.*, Eur. Phys. J. **C75**, 3, 112 (2015), [arXiv:1412.5060].

[233] R. E. Shrock, Phys. Lett. **96B**, 159 (1980).

[234] F. Vissani, Nucl. Phys. B Proc. Suppl. **100**, 273 (2001), [hep-ph/0012018].

[235] Y. Farzan, O. L. G. Peres and A. Yu. Smirnov, Nucl. Phys. **B612**, 59 (2001), [hep-ph/0105105].

[236] J. Schechter and J. W. F. Valle, Phys. Rev. D **25**, 2951 (1982).

[237] J. Engel and J. Menendez, Rept. Prog. Phys. **80**, 4, 046301 (2017), [arXiv:1610.06548].

[238] S. Abe *et al.* (KamLAND-Zen) (2024), [arXiv:2406.11438].

[239] M. Agostini *et al.* (GERDA), Phys. Rev. Lett. **125**, 25, 252502 (2020), [arXiv:2009.06079].

[240] I. J. Arnquist *et al.* (Majorana), Phys. Rev. Lett. **130**, 6, 062501 (2023), [arXiv:2207.07638].
[241] N. Abgrall *et al.* (LEGEND) (2021), [arXiv:2107.11462].
[242] W. H. Dai *et al.* (CDEX), Phys. Rev. D **106**, 3, 032012 (2022), [arXiv:2205.10718].
[243] V. Albanese *et al.* (SNO+), JINST **16**, 08, P08059 (2021), [arXiv:2104.11687].
[244] G. Anton *et al.* (EXO-200), Phys. Rev. Lett. **123**, 16, 161802 (2019), [arXiv:1906.02723].
[245] G. Adhikari *et al.* (nEXO), J. Phys. G **49**, 1, 015104 (2022), [arXiv:2106.16243].
[246] J. Renner *et al.* (NEXT), JINST **13**, 10, P10020 (2018), [arXiv:1808.01804].
[247] D. Q. Adams *et al.* (CUORE), Science **390**, 6777, 1029 (2025), [arXiv:2404.04453].
[248] O. Azzolini *et al.* (CUPID), Phys. Rev. Lett. **129**, 11, 111801 (2022), [arXiv:2206.05130].
[249] C. Augier *et al.* (CUPID), Eur. Phys. J. C **82**, 11, 1033 (2022), [arXiv:2202.08716].
[250] V. Alenkov *et al.* (AMoRE), Eur. Phys. J. **C79**, 9, 791 (2019), [arXiv:1903.09483].
[251] A. Agrawal *et al.* (AMoRE), Phys. Rev. Lett. **134**, 8, 082501 (2025), [arXiv:2407.05618].
[252] R. Arnold *et al.* (NEMO-3), Phys. Rev. **D92**, 7, 072011 (2015), [arXiv:1506.05825].